

Louisiana Tech University

Louisiana Tech Digital Commons

Doctoral Dissertations

Graduate School

Spring 5-25-2024

Phase Interface Dynamics and Heat Transfer Mechanisms in Evaporating Droplet and Pool Boiling Processes

Md Tanbin Hasan Mondal

Follow this and additional works at: <https://digitalcommons.latech.edu/dissertations>



Part of the [Nanoscience and Nanotechnology Commons](#)

**PHASE INTERFACE DYNAMICS AND HEAT TRANSFER
MECHANISMS IN EVAPORATING DROPLET AND POOL
BOILING PROCESSES**

by

Md Tanbin Hasan Mondal, B.S., M.S.

A Dissertation Presented in Partial Fulfillment
of the Requirements of the Degree
Doctor of Philosophy

COLLEGE OF ENGINEERING AND SCIENCE
LOUISIANA TECH UNIVERSITY

May 2024

LOUISIANA TECH UNIVERSITY

GRADUATE SCHOOL

March 12, 2024

Date of dissertation defense

We hereby recommend that the dissertation prepared by

Md Tanbin Hasan Mondal

entitled **Phase Interface Dynamics and Heat Transfer Mechanisms**

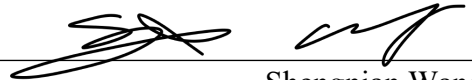
in Evaporating Droplet and Pool Boiling Processes

be accepted in partial fulfillment of the requirements for the degree of

Doctor of Philosophy in Engineering, Micro & Nanoscale Systems Conc.



Arden Moore
Supervisor of Dissertation Research



Shengnian Wang
Head of Engineering

Doctoral Committee Members:

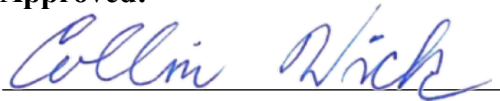
Leland Weiss

Shengnian Wang

Yun Chen

Shafiqur Rahman

Approved:



Collin Wick
Dean of Engineering & Science

Approved:



Ramu Ramachandran
Dean of the Graduate School

ABSTRACT

Despite the significant importance and widespread use of phase-change cooling techniques, there are still fundamental questions about the microscopic processes that govern the heat transfer mechanisms. In order to gain a better understanding of the underlying physics involved, it is essential to have information at the microscale regarding the surface temperature distribution with time as well as the location and speed of the moving contact line (MCL). A comprehensive understanding of heat transfer mechanisms and phase-interface behavior during phase-change cooling is crucial for improving heat transfer models, optimizing surface engineering, and maximizing overall effectiveness.

Firstly, this dissertation presents a capacitance-based microdevice capable of tracking a moving phase interface at the microscale for unconstrained liquid droplets. This microdevice is comprised of an array of planar interdigitated electrodes beneath a thin insulating polymer layer. During the experiments, monitoring changes in capacitance with time facilitated sensing the MCL location and speed as it passes over each capacitance sensor. This capacitive sensing scheme is noninvasive to the system under study, allowing its implementation into many types of existing hardware and devices and not requiring optical access to the phase change area of the device. Implementing multiple capacitance sensors in adjacent proximity for a semiconducting based demonstrated a few limitations, including coupling effects, but it did not prevent the effective detection of MCL. Utilizing a dielectric substrate demonstrated notable improvements, including but not limited to

increased capacitance signal outputs and reduced coupling effects for multiple sensors in adjacent proximity. Moreover, this sensing scheme demonstrated the efficient tracking of MCL during droplet evaporation across different surface temperatures, establishing its functionality at elevated temperatures and during phase-change heat transfer processes.

Next, multifunctional sensing in an evaporation phase change process is demonstrated by combining the capacitance-sensing microsensors with a series of resistance temperature detectors (RTDs) to form a multifaceted MEMS device. This composite MEMS device also includes a resistance heater, making it an independent experimental setup and ensuring its implementation in investigating phase-change cooling processes. The composite MEMS device has been utilized to measure the local heat transfer characteristics and MCL behavior simultaneously for the evaporation of individual sessile water droplets on the heated surface of the device. The microdevice's resistance- and capacitance-based operating principles mean that it can detect temperature changes and track MCL at the microscale in real time, even for applications with limited or no visibility, such as within thermal management hardware or processing equipment. Results of this study showed that the MCL passage precedes the change in local surface temperature, and the duration of the time difference between these events depends on the MCL's speed. In addition, the passage of the MCL accounts for more than 70% of the overall temperature change during the evaporation process.

This work also presents a series of studies in which this composite MEMS device was modified to investigate heat transfer mechanisms and simultaneous tracking of the MCL for subcooled impinging droplets across a range of surface temperatures at multiple impact velocities. Experimental results of this study showed that when a droplet impacts a

heated surface and evaporates, the process can be divided into two segments based on the effective heat transfer rate: an initial conduction-dominated segment followed by another segment dominated by surface evaporation. Results also showed that heat flux at the solid-liquid interface of an impinging droplet increases with the rise of either impact velocity or surface temperature. Additionally, this study demonstrated that convection within evaporating droplets contributes negligibly to overall heat transfer; instead, heat conduction into the droplet and surface evaporation dominates the process.

In the final study presented here, the composite MEMS device was further modified and implemented to measure surface temperature variation and track the movement of the MCL for isolated bubbling events during nucleate boiling of water. Experimental results showed that the rewetting process of the superheated sensing region acted as a fast-quenching event that caused a sharp and sudden temperature drop, and the duration of this event shortened with increasing surface temperature. The bubble nucleation followed the rewetting process and caused a gradual increase in surface temperature as the bubble started to grow with the advancing movement of the MCL. When the growing bubble diameter reached its maximum, the MCL began to recede, indicating the beginning of the rewetting process, which led to the next bubbling cycle.

Collectively, this work represents the first known examples of independent microscale sensing of MCL behavior and surface temperatures and does so for multiple instances of phase change processes. The data produced are analyzed and discussed within the content of fundamental heat transfer processes and prior works. Major findings are presented and guidance on next steps and future studies are provided.

APPROVAL FOR SCHOLARLY DISSEMINATION

The author grants to the Prescott Memorial Library of Louisiana Tech University the right to reproduce, by appropriate methods, upon request, any or all portions of this Dissertation. It is understood that “proper request” consists of the agreement, on the part of the requesting party, that said reproduction is for his personal use and that subsequent reproduction will not occur without written approval of the author of this Dissertation. Further, any portions of the Dissertation used in books, papers, and other works must be appropriately referenced to this Dissertation.

Finally, the author of this Dissertation reserves the right to publish freely, in the literature, at any time, any or all portions of this Dissertation.

Author _____

Date _____

DEDICATION

To my parents, Md Ashraful Islam Mondal and Mst. Sultana Naznin Ara Begum and my wife Rifat-E-Nur Hossain: My journey wouldn't have come this far without your sacrifices and unconditional love.

TABLE OF CONTENTS

ABSTRACT.....	iii
APPROVAL FOR SCHOLARLY DISSEMINATION	vi
DEDICATION	vii
LIST OF FIGURES	xi
LIST OF TABLES	xvii
ACKNOWLEDGMENTS	xviii
CHAPTER 1 INTRODUCTION	1
1.1 Background and Motivation	1
1.2 Dissertation Outline	5
CHAPTER 2 MICROSCALE TRACKING OF UNCONSTRAINED MOVING MULTIPHASE CONTACT LINES VIA A CAPACITANCE SENSOR ARRAY.....	8
2.1 Introduction and Motivation	8
2.2 Methodology	10
2.2.1 Microdevice Overview.....	10
2.2.2 Microfabrication Process	13
2.2.3 Experimental Setup.....	14
2.3 Results and Discussions.....	18
2.4 Summary of Findings.....	26
CHAPTER 3 SPEED AND LOCATION TRACKING OF MOVING MULTIPHASE INTERFACES VIA A CAPACITANCE MICROSENSOR ARRAY DURING DROPLET EVAPORATION	28
3.1 Introduction and Motivation	28

3.2	Methodology	31
3.2.1	Operating Principle	31
3.2.2	Microdevice Overview.....	32
3.2.3	Microfabrication Process	33
3.2.4	Signal Processing.....	34
3.2.5	Experimental Setup.....	35
3.3	Results and Discussion	38
3.4	Summary of Findings.....	48
CHAPTER 4 INDEPENDENT MICROSCALE SENSING OF PHASE INTERFACE AND SURFACE TEMPERATURE DURING DROPLET EVAPORATION.....		50
4.1	Introduction and Motivation	50
4.2	Methodology	58
4.2.1	Microdevice Overview.....	58
4.2.2	Microfabrication Process	61
4.2.3	Experimental Setup.....	62
4.2.4	Surface Temperature Calibration.....	64
4.2.5	Calibration of RTDs.....	66
4.2.6	Calculation of Temperature Difference Across Top Surface and RTDs Layer 67	
4.2.7	Measurement Uncertainty	68
4.3	Results and Discussion	69
4.4	Summary of Findings.....	92
CHAPTER 5 HEAT TRANSFER AND PHASE INTERFACE DYNAMICS DURING IMPACT AND EVAPORATION OF SUBCOOLED IMPINGING DROPLETS ON A HEATED SURFACE.....		94
5.1	Introduction and Motivation	94
5.2	Methodology	99

5.2.1	Microdevice Overview.....	101
5.2.2	Experimental Setup.....	103
5.3	Results and Discussion	105
5.3.1	Hydrodynamic Perspectives.....	105
5.3.2	Heat Transfer Perspectives	108
5.3.3	Interdependence of Phase Interface and Heat Transfer Dynamics	112
5.3.4	Energy Balance and Thermal Resistance.....	120
5.3.5	Contribution of Convection within Droplet.....	125
5.3.6	Calculation of the Dimensionless Parameters.....	127
5.3.7	Key Findings.....	128
5.4	Summary of Findings.....	131
CHAPTER 6 INVESTIGATION OF HEAT TRANSFER MECHANISMS AND THREE-PHASE CONTACT LINE BEHAVIOR OF NUCLEATED BUBBLES IN POOL BOILING WITH COMPOSITE MEMS DEVICE		134
6.1	Introduction and Motivation	134
6.2	Methodology	136
6.2.1	Microdevice Overview.....	136
6.2.2	Experimental Setup.....	139
6.3	Results and Discussion	141
6.4	Summary of Findings.....	147
CHAPTER 7 CONCLUSIONS AND FUTURE WORKS.....		148
7.1	Conclusions.....	148
7.2	Future Works	151
REFERENCES		154

LIST OF FIGURES

Figure 1-1: Heat flux vs. heat transfer coefficients for different cooling technologies (Reproduced with permission from [1]).	2
Figure 2-1: (a) Conceptual illustration of the capacitive sensing scheme (substrate not shown, not to scale) (b) Optical microscope image of the completed sensor array containing six capacitance sensors, with numbering going from bottom to top of the image (CS-1 to CS-6). (c) A detail of the sensing zone enclosed by the dashed box in (b) containing three IDE capacitance sensors.	13
Figure 2-2: (a) Schematic of the sensing circuit (b) Experimental set-up containing capacitance microdevice and chip carrier combo attached to a PGA socket on DSA (c) Conceptual schematic of the expanding and contracting droplet during the experiment.	16
Figure 2-3: Collaged images showing dosing (Images 1-4) and retraction (Images 5-8) of an unconstrained deionized water droplet during the testing of the sensors. The dashed rectangle in image 1 shows the capacitance sensor array (CS-1 through CS-6). .	17
Figure 2-4: Measured capacitance signal for advancing and receding water droplets with (a) sensor couple contains CS-1 and CS-3, (b) sensor couple consists of CS-1 and CS-2. (Due to a sampling frequency of 30 Hz, the discrete data points in the plots are closely spaced, appearing as continuous lines. For clarity of presentation, lines are used instead of discrete data points.).....	20
Figure 2-5: Measured capacitance signal for dosing and retraction of water droplets by using (a) three capacitance sensors CS-1, CS-3, and CS-6, (b) two capacitance sensors CS-3 and CS-6.	21
Figure 2-6: Measured capacitance signal for dosing and retraction of water droplets by using CS-1, CS-2, and CS-3 simultaneously.	22
Figure 2-7: (a) A diameter vs. step number plot acquired via DSA: change in diameter denoting dosing and retraction of water droplets during the experiment (b) Plot of contact angles with step number for water droplets on polyimide surface.	25
Figure 3-1: (a) A conceptual illustration of the capacitive sensing scheme (not to scale). (b) A laser-microscopic image of the microdevice showing resistance heater and capacitance micro-sensor array. (c) A detailed view of the sensing zone enclosed by the dashed box in (b) showing six capacitance sensors based on interdigitated	

electrodes. The resistance heater and interdigitated electrodes are on separate device layers and separated by a polymer thin film as described in the main text. 30

Figure 3-2: (a) Schematic of the experimental setup for tracking speed and location of MCL with a capacitance-based phase interface sensing microdevice, (b) Schematic of the supporting electric circuit used for each IDE electrode pair..... 35

Figure 3-3: Optical images of gradual dosing (Images 1-3) and retraction (Images 4-6) of a water droplet captured by the drop shape analyzer tool during initial aspiration experiments on substrate effects. The dashed box in Image 6 shows the location of the sensing zone of the microdevice comprising six capacitance micro-sensors CS-1 to CS-6 (numbered left to right). 37

Figure 3-4: Optical images of the evaporation process of a water droplet captured by drop shape analyzer equipment during the experiment. The dashed box in Image 1 shows the location of the sensing zone of the microdevice. 37

Figure 3-5: Measured normalized capacitance changes for advancing and receding deionized water droplets using the sensor pair CS-1 and CS-6 on a doped silicon substrate, where the dashed boxes denote the significant movements of MCL as shown in the optical images on top. 39

Figure 3-6: Normalized capacitance changes with time for advancing and receding deionized water droplets using capacitance micro-sensors CS-1, CS-3, and CS-6 with the microdevice based on a doped silicon substrate. 40

Figure 3-7: Normalized capacitance changes with time for advancing and receding deionized water droplets using capacitance micro-sensors CS-1, CS-3, and CS-6 with the microdevice based on a soda-lime glass substrate. 41

Figure 3-8: Normalized capacitance changes with time for advancing and receding deionized water droplets using three capacitance micro-sensors (CS-1, CS-2, and CS-3) in adjacent proximity with the microdevice based on a doped silicon substrate..... 42

Figure 3-9: Normalized capacitance changes with time for advancing and receding deionized water droplets using three capacitance micro-sensors (CS-1, CS-2, and CS-3) in adjacent proximity with the microdevice based on a soda-lime glass substrate. 43

Figure 3-10: Schematic of electric field lines distribution when a capacitance sensor is operating on its own (top) and when two IDE-based capacitance sensors are placed adjacent (bottom). 45

Figure 3-11: Normalized capacitance changes with time for droplet evaporation on a heated polyimide surface at 57.2 °C using all six capacitance micro-sensors (CS-1 to CS-6). The dashed box on the top right shows a close-up of the time lag among the sensors as the droplet evaporates away from the sensor region..... 46

Figure 3-12: Normalized capacitance changes with time for droplet evaporation on a heated polyimide surface at 70.7 °C using six capacitance micro-sensors (CS-1 to CS-6). The dashed box on the top right shows the time lag among the sensors as the droplet evaporates away from the sensor region.	47
Figure 3-13: Normalized capacitance changes with time for droplet evaporation on a heated polyimide surface at 85.5 °C using six capacitance micro-sensors (CS-1 to CS-6). The dashed box on the top right shows the time lag among the sensors as the droplet evaporates away from the sensor region.	48
Figure 4-1: Schematic of the contact line region of a hydrophilic evaporating droplet on a solid surface.	54
Figure 4-2: Laser microscope images of the micro-device. (a) A detail of the sensing zone containing six IDE capacitance micro-sensors, a series of four-probe type RTDs, and a resistance heater. (b) Thin-film resistance heater (serpentine feature) located beneath RTD and IDE layers. (c) A close-up of the sensing region showing detailed view of the IDEs and RTDs. (d) Schematic diagram of the cross-section of the micro-device. Conceptual image, not to scale.	59
Figure 4-3: Schematic of the experimental setup. Conceptual image, not to scale.	63
Figure 4-4: Representative optical image composite from the DSA for an evaporating droplet during an experiment. The dashed box at the top left of the collaged image highlights the sensing zone of the micro-device.	64
Figure 4-5: Measured surface temperatures at various power inputs during the calibration of the resistance heater.	65
Figure 4-6: Measured voltage outputs at various temperatures during the calibration of the RTD.	66
Figure 4-7: Change in resistance at various temperatures during the calibration of the RTD-12R.	67
Figure 4-8: Measured surface temperatures at various power inputs during the calibration of the resistance heater.	70
Figure 4-9: Evaporation process of a 6 μ L water droplet on a heated polyimide surface at 69.7 °C (a) absolute capacitance changes with time using six capacitance micro-sensors (CS-1 to CS-6), (b) temperature distribution with time employing twelve functioning RTDs.	73
Figure 4-10: Evaporation process of a 6 μ L water droplet on a heated polyimide surface at 61.0 °C (a) absolute capacitance changes with time using six capacitance micro-sensors (CS-1 to CS-6), (b) temperature distribution with time employing twelve functioning RTDs.	74

- Figure 4-11:** Evaporation process of a 6 μL water droplet on a heated polyimide surface at 53.0 $^{\circ}\text{C}$ (a) absolute capacitance changes with time using six capacitance micro-sensors (CS-1 to CS-6), (b) temperature distribution with time employing twelve functioning RTDs..... 75
- Figure 4-12:** Local temperature distribution and change in capacitance signal on the outset of droplet evaporating away from the heated polyimide surface at 69.7 $^{\circ}\text{C}$ 78
- Figure 4-13:** Local temperature distribution and change in capacitance signal on the outset of droplet evaporating away from the heated polyimide surface at 61.0 $^{\circ}\text{C}$ 80
- Figure 4-14:** Local temperature distribution and change in capacitance signal on the outset of droplet evaporating away from the heated polyimide surface at 53.0 $^{\circ}\text{C}$ 82
- Figure 4-15:** Normalized heat flux changes with time for an evaporating droplet on a heated polyimide surface at 69.7 $^{\circ}\text{C}$ 85
- Figure 4-16:** Normalized heat flux changes with time for an evaporating droplet on a heated polyimide surface at 61.0 $^{\circ}\text{C}$ 86
- Figure 4-17:** Normalized heat flux changes with time for an evaporating droplet on a heated polyimide surface at 53.0 $^{\circ}\text{C}$ 87
- Figure 4-18:** (a) Local temperature distribution, (b) distribution of lateral heat flux for a receding MCL at surface temperature of 69.7 $^{\circ}\text{C}$ 88
- Figure 4-19:** (a) Local temperature distribution, (b) distribution of lateral heat flux for a receding MCL at surface temperature of 61.0 $^{\circ}\text{C}$ 89
- Figure 5-1:** Optical images of the composite microdevice employed for investigating droplet impingement: (a) the microdevice attached to a ceramic chip carrier; (b) microscope image of the microdevice's sensing zone comprising RTDs, IDE-based capacitance microsensors, and a resistance heater; (c) a detailed view of the sensing zone, showcasing IDEs and RTDs..... 102
- Figure 5-2:** Time elapsed images of impacting droplets on a polyimide surface at four different impact velocities: (a) 0.58 m/s ($We = 11.2$), (b) 1.05 m/s ($We = 36.7$), (c) 1.22 m/s ($We = 49.2$), (d) 1.35 m/s ($We = 60.7$)..... 106
- Figure 5-3:** Evolution of droplet contact diameter with time at varying impact velocities (discrete points are connected through dashed lines to show the trend). 107
- Figure 5-4:** Evolution of diameter and contact angle over time of a 6.0 μL impacting water droplet on the polyimide surface at the surface temperature of 80.9 $^{\circ}\text{C}$ 108
- Figure 5-5:** Influence of varying impact velocities u during impingement of a 6.0 μL water droplet on the heated polyimide surface of the microdevice at 72.9 $^{\circ}\text{C}$, (a) change in temperature over time, (b) heat flux values over time for varying impact velocities,

(c) temperature change due to impingement vs. impact velocities, (d) heat flux due to impingement vs. impact velocities..... 110

Figure 5-6: Influence of varying surface temperatures during impingement of a 6.0 μL water droplet on the heated polyimide surface of the microdevice at $u = 1.05 \text{ m/s}$: (a) change in temperature over time, (b) heat flux values over time for varying surface temperatures, (c) temperature change due to impingement vs. surface temperatures, (d) heat flux due to impingement vs. surface temperatures..... 111

Figure 5-7: Droplet impact and subsequent evaporation of a 6.0 μL water droplet on a heated polyimide surface at 68.8°C (a) absolute capacitance change (%) with time depicting the passage of MCL, (b) temperature distribution with time (dashed box shows the temperature changes on a millisecond timescale directly preceding and following the moment of droplet impingement)..... 112

Figure 5-8: Droplet impact and subsequent evaporation of a 6.0 μL water droplet on a heated polyimide surface at 80.9°C (a) absolute capacitance change (%) with time depicting the passage of MCL, (b) temperature distribution with time..... 114

Figure 5-9: Droplet impact and subsequent evaporation of a 6.0 μL water droplet on a heated polyimide surface at 89.5°C (a) absolute capacitance change (%) with time depicting the passage of MCL, (b) temperature distribution with time..... 115

Figure 5-10: Heat flux distribution with time due to droplet impact and subsequent evaporation of a 6.0 μL water droplet on a heated polyimide surface at 68.8°C 117

Figure 5-11: Heat flux distribution with time due to droplet impact and subsequent evaporation of a 6.0 μL water droplet on a heated polyimide surface at 80.9°C 118

Figure 5-12: Heat flux distribution with time due to droplet impact and subsequent evaporation of a 6.0 μL water droplet on a heated polyimide surface at 89.5°C 118

Figure 5-13: Heat transfer rate distribution with time at the solid-liquid interface due to droplet impact and subsequent evaporation of a 6.0 μL water droplet on a heated polyimide surface at 80.9°C as measured by the microscale RTDs. 123

Figure 5-14: Change in volume and heat transfer rate at the liquid-vapor interface over time due to evaporation of a 6.0 μL water droplet on a heated polyimide surface at 80.9°C 124

Figure 6-1: Laser microscope images of the microdevice. (a) A detail of the sensing zone containing six IDE capacitance micro-sensors, a series of four-probe type RTDs, two hydrolysis trigger electrodes, and a resistance heater. (b) Thin-film resistance heater (serpentine feature) located beneath RTD and IDE layers. (c) A close-up of the sensing region showing detailed view of the IDEs and RTDs. (d) Schematic diagram of the cross-section of the microdevice. Conceptual image, not to scale. 137

- Figure 6-2:** Laser microscopic image of the nucleation cavity at the center of the device, fabricated by RIE etching of the polyimide layer. 138
- Figure 6-3:** (a) Pool boiling experimental setup consisting of 1: Borosilicate glass chamber, 2: Nichrome wire heater, 3: Thermocouple, 4: MEMS device, 5: Aluminum top plate, 6: Cylindrical enclosure machined out of MDS-filled cast nylon to hold the microdevice in inside the boiling test rig. (b) A nucleated bubble at the onset of departure from the center of the device. 140
- Figure 6-4:** A 3D model of the cylindrical enclosure machined out of MDS-filled cast nylon to hold the microdevice and connecting wires inside: (a) isometric view, (b) sectional view..... 140
- Figure 6-5:** Test results at a surface temperature of 111.5 °C show the MCL passage and surface temperature variation for a few bubbling events. 141
- Figure 6-6:** A detailed view of the MCL passage and surface temperature variation of two consecutive bubbling events for an experiment conducted at a surface temperature of 111.5 °C..... 143
- Figure 6-7:** A detailed view of the MCL passage and surface temperature variation of two consecutive bubbling events for an experiment conducted at a surface temperature of 115.4 °C..... 143
- Figure 6-8:** Vertical heat fluxes corresponding to the surface temperature variation of three consecutive bubbling events for an experiment conducted at a surface temperature of 113.2 °C..... 145
- Figure 6-9:** Vertical heat fluxes corresponding to the surface temperature variation of three consecutive bubbling events for an experiment conducted at a surface temperature of 113.2 °C..... 146

LIST OF TABLES

Table 2-1: DC sputtering parameters for deposition of platinum thin film for IDEs.	14
Table 2-2: RIE etching parameters for removal of polyimide on top of contact pads.....	14
Table 4-1: Summary of MCL passage, speed, and its effects on the thermal response for droplet evaporation.....	79
Table 4-2: Summary of heat flux values caused by advancing MCL, receding MCL, and liquid bulk.	86
Table 5-1: Table of nomenclature.....	95
Table 5-2: Summary of the heat flux values resulting from drop impingement and receding MCL due to evaporation.	120
Table 6-1: Summary of the effect of surface temperature on the bubbling event.	145

ACKNOWLEDGMENTS

First and foremost, I would like to express my gratitude to my advisor, Dr. Arden Moore, for his unwavering support and guidance throughout my Ph.D. journey. This achievement would not have been possible without his excellent mentorship, relentless support, and encouragement. Working under him and learning as I grow as a very young researcher has been my immense pleasure.

I would like to sincerely thank all my fellow research group members, including Shayan Davani, Amit Rai, Nishan Khatri, Tithi Desai, Rifat-E-Nur Hossain, John Barham, and Mahdi Roodbari, who helped me immensely with their guidance and support. I would also like to thank research assistants and collaborators from other research groups who immensely helped me with their suggestions and assistance, especially Md Shafayat Alam, Kiran Seetala, and Ronald Martin.

I greatly appreciate the guidance and help from my advisory committee members, Dr. Leland Weiss, Dr. Shengnian Wang, Dr. Shafiqur Rahman, and Dr. Yun Chen.

I want to thank Ms. Debbie Wood, Mr. Davis Bailey, Mr. Mark Lowe, and other IfM staff for providing training in various equipment and helping with various measurements and analyses during my research.

My journey wouldn't have come this far without the endless support and encouragement from my parents and wife; I am sincerely grateful for that.

CHAPTER 1

INTRODUCTION

1.1 Background and Motivation

As advanced and specialized technologies have developed over the last few decades and taken over most of present-day manufacturing and industrial sectors, a diverse range of thermal management methods have evolved to keep up. Phase-change cooling has been one of the most effective methods, with superior performance and outstanding capabilities of retaining uniform cooling temperature distribution throughout the heat flux surface [1]–[4]. More recently, with the increase in power density, microelectronic industries have been pushing traditional thermal management techniques such as air-cooled plates and pin-fin heat sinks to their maximum limit, where phase change cooling has emerged as an effective technique [2], [5]. Evaporative cooling and nucleate boiling have been considered effective means of phase change cooling capable of handling high heat fluxes due to the significant amount of thermal energy associated with the latent heat of vaporization of the fluid, which reduces the thermal resistance between the heat source and sink [1], [6]–[8]. A recent review [1] of thermal performance comparison of evaporative cooling and other technologies has demonstrated that evaporative heat transfer techniques (specifically micro and nanostructures-enhanced) outperform other methods reported in the current literature, as shown in Figure 1-1. Because of the broader applicability in diverse industrial sectors, including ultra-high heat flux microelectronics applications and providing superior

performance in electronic thermal management, researchers have extensively investigated phase-change cooling techniques such as droplet evaporation, droplet impingement on a heated surface, and nucleate boiling [1], [4], [9]–[11].

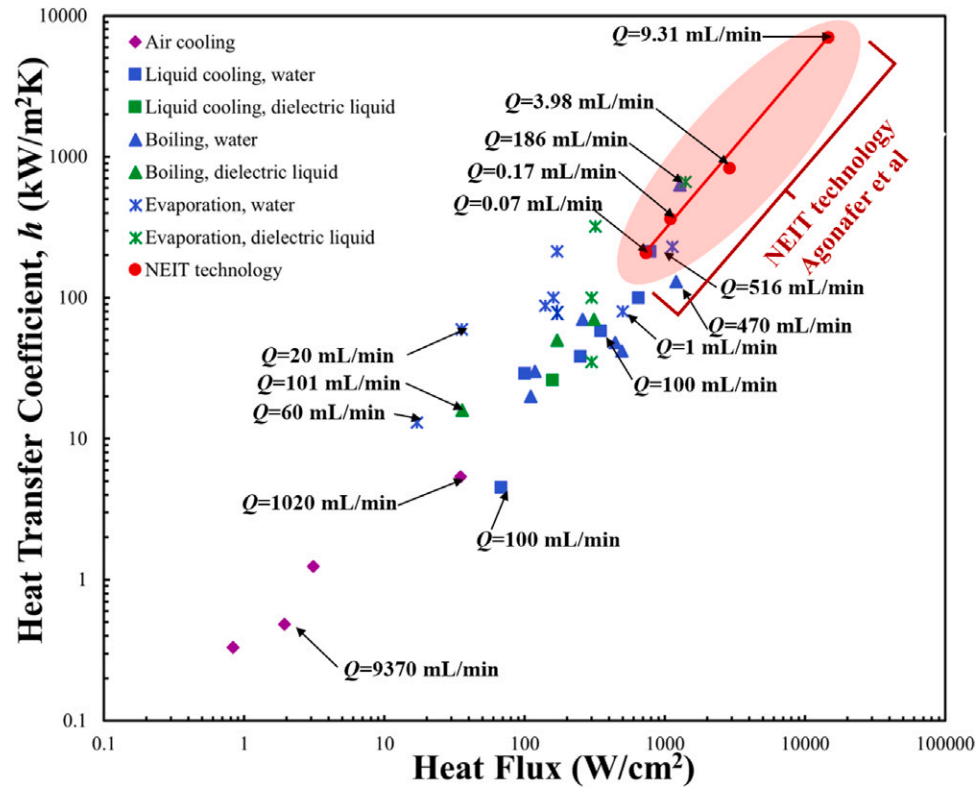


Figure 1-1: Heat flux vs. heat transfer coefficients for different cooling technologies (Reproduced with permission from [1]).

Despite its broad applicability and even ubiquity across natural events, investigating phase-change cooling techniques is not trivial as it is a complex phenomenon involving mass, momentum, and heat transfer interactions and usually comprised of various multifaceted processes, including but not limited to conjugate heat transfer at the moving contact line region, the motion of the moving contact line, micro-convection within the liquid, and surface evaporation [1], [4], [9]–[11]. A three-phase phenomenon where the liquid-vapor interfaces meet the solid heat flux surface is known as the moving contact line

(MCL) [12]. This moving interface plays an essential role in ensuring a thorough interpretation of the heat transfer mechanisms for phase-change cooling processes. Gaining a fundamental understanding of how heat transfer mechanisms and phase interface behavior influence or interact with each other during phase-change cooling processes is crucial for refining heat transfer models, optimizing surface engineering, and enhancing overall effectiveness. Correlating the interdependence of heat transfer mechanisms with dynamic phase interface behavior during these processes requires sophisticated and multifaceted sensing schemes to simultaneously measure temperature distribution and track MCL location and speed. While there have been numerous studies conducted in literature to explore heat transfer mechanisms during these processes, there is only a limited number of studies that focused on measuring the microscopic thermo-fluid phenomena near the MCL region, specifically correlating the heat transfer data to the phase interface behavior. Therefore, studying these processes from heat transfer and hydrodynamic perspectives and developing multifaceted sensing schemes to achieve this goal is a pressing need in this field of research.

Experimental approaches within the literature have mainly employed infrared thermography (IR) or macroscopic temperature sensing probes to measure the temperature distribution during investigating phase-change cooling processes [1], [13]. These temperature measurement techniques pose significant constraints, including low-temperature resolution, slower response time, and potential invasiveness to the process under study. IR, for instance, is only applicable in places where optical access to the surface is available. Additionally, the camera resolution and wavelength diffraction limit often limit IR thermography in detecting microscale temperature distribution at the thin-film

region [1], [14], [15]. Previous research has typically relied on external equipment, such as high-speed cameras and optical image processing, to track the MCL and investigate the interfacial behavior of the phase-change processes. However, these techniques usually have macroscopic spatial resolution and limited visibility, which often hamper precise detection of the location and temperature gradient in the MCL region because of the line of sight and viewing angle constraints [16]–[19].

This work addressed these research needs and demonstrated the development of an interdigitated electrode (IDE) based capacitance sensing microdevice capable of tracking MCL speed and location at room and elevated temperatures applicable for dynamic phase-change heat transfer processes. After successful performance testing of this capacitance sensing scheme, a MEMS device was developed, combining capacitance microsensors with microscale thermal sensors. This multifaceted composite MEMS device provided significant utility, especially in simultaneous tracking of MCL and measuring corresponding temperature changes in phase-change cooling processes. This work extensively describes how these sensing schemes were developed, tested, and employed to investigate real-life phase-change cooling processes such as droplet evaporation, droplet impingement on a heated surface, and nucleate boiling. Moreover, the experimental findings of this work, from investigating the fundamental heat transfer mechanisms and phase-interface behavior during phase-change cooling processes, can offer crucial insights

into underlying physics for enhancing heat transfer models, surface engineering, and overall effectiveness.

1.2 Dissertation Outline

Chapters 2 to 6 of this dissertation provide an extensive description of the research works that have developed multiple functional MEMS devices based on capacitance sensing alone and combined with microscale thermal sensors intended for investigating phase-change cooling processes to reveal the fundamental mechanisms associated with these processes.

Chapter 2 describes the design, fabrication, and testing of a capacitance-sensing microdevice based on IDEs where a semiconducting base was utilized as the starting substrate. This microdevice demonstrated good functionality in detecting the speed and location of MCL for both advancing and receding movement of unconstrained droplets at room temperature. However, employing multiple sensors in close proximity led to sensor coupling effects and signal inversion, which opened windows to improve the device design and overcome these limitations.

Chapter 3 provides a detailed description of a work based on the capacitance-sensing microdevice that adopts a dielectric base, which also extensively demonstrates the performance comparison of the same device on different substrate types. Adopting a dielectric base instead of the semiconductor has improved the overall performance of the capacitance-sensing microdevice by reducing the proximity effects and signal inversion. To make the device suitable for elevated temperature applications, a thin-film heater was incorporated, which made it applicable to investigate phase-interface behavior during dynamic phase-change processes such as droplet evaporation.

Chapter 4 describes the fabrication and testing of a custom-made composite MEMS device with a primary focus on the underlying physics revealed by investigating the evaporation of small-scale water droplets from its top polymer surface. After successfully validating the functionality of the capacitance sensing scheme described in the previous two chapters, a multifaceted MEMS device was developed by combining a series of microscale resistance temperature detectors (RTDs) with these capacitance microsensors. This composite microdevice also includes a thin-film resistance heater at the bottom, where a thin insulating polymer separates each two consecutive sensor layers. This microdevice adopted a soda lime glass as the starting substrate and facilitated an independent experimental setup for investigating phase-change cooling processes.

Chapter 5 describes the modifications made to the composite MEMS device and key findings from the heat transfer and hydrodynamic perspectives of droplet impingement heat transfer investigated by the modified device. After investigating droplet evaporation, this work aimed to investigate more transient heat transfer processes, such as droplet impingement heat transfer, which is the fundamental unit of spray cooling. To investigate such processes, a microdevice that could respond to rapid temperature changes was required. Therefore, a silicon substrate was adopted as the starting substrate, and a micro-membrane was fabricated underneath the sensing zone. These modifications made this device more versatile and enabled the study of heat transfer and phase interface dynamics during droplet impingement and subsequent evaporation from the heated surface of the microdevice.

Chapter 6 details the further modifications of this composite MEMS device, where an artificial nucleation cavity was fabricated in the middle of the sensing zone to make it

suitable for investigating nucleate boiling processes. An experimental setup was developed that allowed only the sensing zone of the MEMS device to get in contact with a pool of liquid while the connecting wires and other setup components were outside the pool. An external heater controlled by a temperature controller was utilized to reach the pool's temperature near the saturation point, and then heat was applied to the resistance heater of the device to nucleate bubbles. This MEMS device investigated each nucleated bubble's heat transfer mechanisms and phase interface behavior during the experiment.

Chapter 7 summarizes the main findings and impacts of the custom-made MEMS devices used to investigate phase-change cooling processes. The devices and experimental techniques utilized in these studies have the potential for future research opportunities, which are also described in this chapter.

CHAPTER 2

MICROSCALE TRACKING OF UNCONSTRAINED MOVING MULTIPHASE CONTACT LINES VIA A CAPACITANCE SENSOR ARRAY

2.1 Introduction and Motivation

The MCL plays a crucial role in various essential physical, chemical, biological, and thermal phenomena and has numerous applications in technological processes such as polymer processing, coating of solids by liquid films, wetting of powders, and production of photographic film [20], [21]. Tracking the speed and location of MCL in real time has been a matter of great emphasis in a broad range of disciplines, including heat transfer, microfluidics, materials science, bioengineering, and chemical engineering [21]. Optical and electrical sensing have been the two most commonly adopted means for tracking the MCL within the literature [16]. Despite being the most familiar technique for tracking MCL within the literature, optical sensing often relies on bulky equipment and fluorescent labeling, limiting its utility outside laboratory environments and its ability to integrate it into microdevices. [16], [19]. On the other hand, electrical sensing provides a scalable means of achieving real-time detection of the MCL; it is also advantageous because of its simplicity, cost-effectiveness, and applicability in microscale devices [16]. The two active trends in electrical-based MCL sensing are resistive and capacitive sensing approaches, which have been utilized extensively in this area of research [22]. There are significant differences between resistive and capacitive sensing. One of the major drawbacks of

resistive sensing is the requirement of a continuous conductive phase in the sensing region [16]. In addition, resistive sensors are not easily scalable as they often require intricate patterns to achieve the sensing scheme. In contrast, capacitive sensors only require a small gap between two coplanar electrodes as the primary sensing element, making them suitable to incorporate into microscale devices [23]. Capacitive sensing also offers a highly sensitive and minimally invasive scheme of tracking MCL suitable for electrically insulating and conductive liquids [17]. In capacitive sensing, the capacitance of the sensed region changes due to changes in dielectric constants as the liquids cover or pass over the sensing zone above the electrodes. This scheme enables contactless detection of MCL as the droplets under study do not come in physical contact with the electrodes [16], [19]. Adopting IDEs arrays increases the sensitivity of the capacitive sensing scheme, making the sensing scheme suitable for microscale droplets and less concentrated liquids [17]. Prior studies within the literature of MCL sensing via capacitance change have all demonstrated usage only for confined liquid droplets, or fluid flows in microchannels [16], [19], [24]. Therefore, there is a pressing need to investigate the use of capacitance-based MCL sensing for unconstrained droplet detection, such as occurs in condensation and evaporation-based heat transfer processes. This work aims to address this need by demonstrating a capacitance sensing approach capable of detecting the location and speed of a moving MCL for unconstrained liquid droplets with both advancing and receding movements.

This work presents a low-cost and scalable capacitance-based phase interface sensing approach, which can detect the speed and location of a moving phase interface at the microscale for unconstrained liquid droplets. The capacitance sensor reported in this work adopted an array of planar IDEs deposited on a thermally grown oxide layer atop a

silicon substrate. A thin layer of polymer acted as the topmost protective coating and prevented the liquid droplets from directly contacting the surface of the metallic IDEs. The capacitive sensing scheme is designed to facilitate highly sensitive, bulk fabrication compatible, and minimally invasive MCL sensing for various applications ranging from biomedical devices to heat exchangers. The proposed sensing method resembles the micro-scale electrical capacitance tomography of the area directly above the IDEs, which monitors the real-time change in capacitance at different positions. The performance of the sensing scheme has been verified by comparing the observations made with a commercial drop-shape analyzer tool, a widely accepted standard method. The results and discussion presented in this study include the device's MCL location and speed detection performance, as well as the spatial resolution limits and influence of coupling and parasitic capacitance on the IDE sensor array.

2.2 Methodology

2.2.1 Microdevice Overview

The basic operating principle of a capacitance-based phase interface sensor is that the capacitance of the region directly above the sensor changes due to differences in dielectric constant ϵ_r with the passage of the MCL [16], [19]. Figure 2-1(a) shows that, the electric field lines resulting from the applied sensing voltage on a pair of coplanar electrodes extend directly above the insulating layer to interact with the moving MCL region. Given the specific conditions of this study, the presence of water ($\epsilon_r = 80$ [19]) on the thin polyimide layer of sensing region ($\epsilon_r = 3.4$ [25]) causes a large change in the local dielectric constant compared to when air ($\epsilon_r = 1.0$ [26]) alone is present over the polyimide, which results in a significant change in effective dielectric constant of the region $\epsilon_{r,eff}$ in

the sensed region and the associated measured capacitance. In addition to $\epsilon_{r,eff}$, the capacitance C also depends on the width w and spacing $2a$ between the coplanar electrodes, which can be calculated by [17]

$$C = \frac{2\epsilon_{r,eff}\epsilon_0 l}{\pi} \ln \left[\left(1 + \frac{w}{a}\right) + \sqrt{\left(1 + \frac{w}{a}\right)^2 - 1} \right] \quad \text{Eq. 2-1}$$

where ϵ_0 is the vacuum permittivity and l is the interaction length of the electrode pair. This equation was derived under the assumptions of $w/a \gg 1$ and $l \gg w$, as stated in an analytical model for coplanar capacitive sensing by Chen et al. [17]. According to Eq. 2-1, the capacitance of the sensed region increases with increasing interaction length of the electrode pair. Adopting an electrode design with an array of planar IDEs and increasing the interaction length of the electrode pairs are effective ways to increase the capacitance of the sensed region and the measurement signal [17], [27]. The thickness of the polyimide thin film as the topmost coating also affects the effective relative permittivity $\epsilon_{r,eff}$ of the sensed region such that a thin insulation layer is preferred to maximize the sensitivity and signal strength of the capacitive sensor [16]. The penetration depth T of the sensing region refers to the vertical reach of the electric field lines from the topmost surface of the coplanar electrodes. Penetration depth varies with the width and spacing of the electrodes via the expression [17]

$$T = a \sinh \left[\cosh^{-1} \left(1 + \frac{w}{a}\right) \right] = a \sqrt{\left(1 + \frac{w}{a}\right)^2 - 1} \quad \text{Eq. 2-2}$$

Equations Eq. 2-1 and Eq. 2-2 were applied to achieve the best possible geometry of the sensing feature, which ensured that the capacitance signal had a higher strength while maintaining the penetration depth required for the experiment of interest and the desired

spatial resolution along the surface. The spatial resolution is also impacted by limitations associated with the intended microfabrication processes, which put lower bounds on the achievable electrode width and spacing. The geometry of the IDE influences both the magnitude of the capacitance of the sensed region and the magnitude of the changes in capacitance as the MCL passes over and $\epsilon_{r,eff}$ is altered. Although the increasing width of the electrode causes an increase in capacitance signal, it decreases with the growing spacing between electrodes. A higher number of electrode fingers and finger lengths increases the strength of the capacitance signals by facilitating more electric field lines within the sensed region. However, increased width, finger length, and the number of electrodes will restrain the applicability of the sensor in microscale devices by increasing the physical dimensions. Therefore, it is desirable to design the IDE to produce a measurable capacitance while keeping the overall IDE footprint small to ensure the best achievable spatial resolution. Specialized microfabrication techniques, such as electron beam lithography, offer excellent spatial resolution for creating compact IDEs with very small electrode widths and spacings, but their high cost and low throughput outweigh their utility [27]. In this work, the optimum geometry of the IDEs was chosen to facilitate measurable capacitance signal and minimum IDE footprint while still allowing for efficient batch microfabrication via conventional microfabrication techniques. Specifically, IDEs with electrode length $l = 250 \text{ } \mu\text{m}$, width $w = 6 \text{ } \mu\text{m}$, and electrode spacing $a = 3 \text{ } \mu\text{m}$, and electrode were utilized as shown in Figure 2-2 (b)-(c). The value of the penetration depth for this IDE design is $8.49 \text{ } \mu\text{m}$ as calculated using Eq. 2-2. Each test device consists of a series of six IDEs to explore the usage of multiple IDEs in close proximity on a common substrate, specifically for precise tracking of the speed and location of MCL.

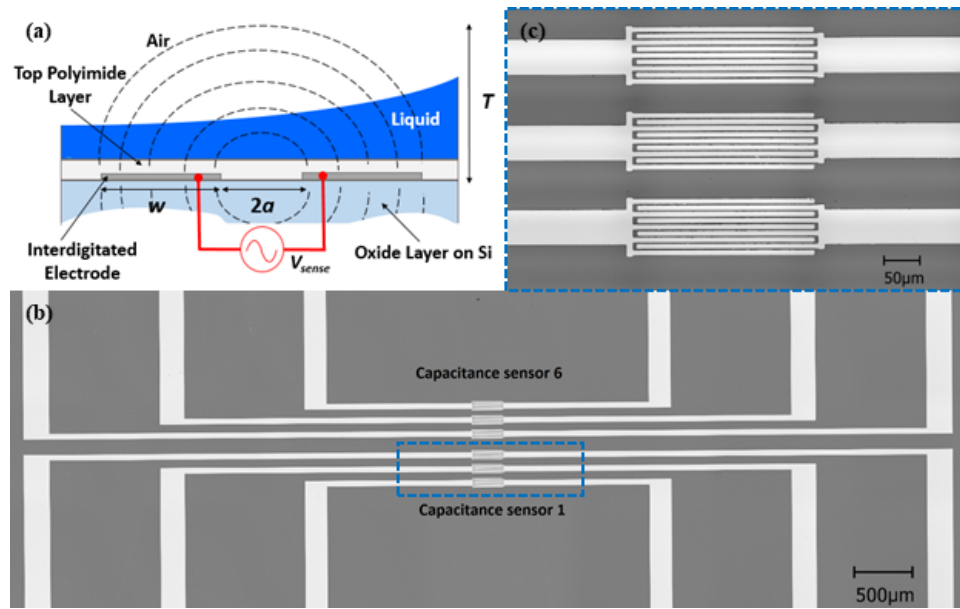


Figure 2-1: (a) Conceptual illustration of the capacitive sensing scheme (substrate not shown, not to scale) (b) Optical microscope image of the completed sensor array containing six capacitance sensors, with numbering going from bottom to top of the image (CS-1 to CS-6). (c) A detail of the sensing zone enclosed by the dashed box in (b) containing three IDE capacitance sensors.

2.2.2 Microfabrication Process

The capacitance sensor was microfabricated by depositing platinum (Pt) via a lift-off process followed by spin coating of a thin polyimide insulating layer. A commercially obtained 500 μm thick silicon wafer with a 500 nm thermally grown oxide layer was used as the starting substrate. After photoresist patterning of the IDE capacitance sensor array via standard UV photolithography, the deposition of a 100 nm thick layer of Pt as the IDEs was carried out in an AJA ATC sputtering system via DC sputtering process with a commercially available 3-inch sputtering target by applying the process parameters given in Table 2-1 below. A spin-on polyimide (PI-2611) was acquired from HD Microsystems for spin-coating of the thin insulating layer on top of the IDEs. The spin-coating of the PI-2611 was accomplished in a closed-bowl spin-coater to ensure a uniform deposition of a

400 nm thick insulating layer of polyimide. While a thin insulating layer is desirable for capacitance sensing purposes, it is equally important that the protective polyimide layer is thick enough to prevent the deposited IDEs underneath from protruding and affecting the surface wettability behavior. A thickness of 400 nm was determined to effectively balance these two requirements.

Table 2-1: DC sputtering parameters for deposition of platinum thin film for IDEs.

Baseline process parameters for DC sputtering deposition of platinum (Pt)				
Pressure	Power density	Argon (Ar) flow	RF Bias	Deposition rate
3 mTorr	225 W/cm ²	10 sccm	-	18.75 nm/min

Table 2-2: RIE etching parameters for removal of polyimide on top of contact pads.

Baseline process parameters for RIE of polyimide layer				
Pressure	Power	SF ₆ flow	O ₂ flow	Etch rate
180-190 mTorr	200 W	5 sccm	25 sccm	75-100 nm/min

As shown in Figure 2-1(b), the entire capacitive sensing device consists of an array of six capacitive sensors, which are individually connected to pairs of contact pads at the device periphery. To ensure proper wire bonding between the microdevice and the chip carrier, the polyimide layer from the contact pads was etched using a reactive ion etching (RIE) process in a Technics MICRO-RIE equipment using the process parameters given in in Table 2-2.

2.2.3 Experimental Setup

After microfabrication and dicing, individual capacitive devices were secured within the top cavity of the leaded chip carrier commercially obtained from Spectrum

Semiconductor Materials Inc. Each contact pad of the microdevice was wire-bonded individually with a contact pad of the chip carrier. Each of the contact pads of the chip carrier is attached independently to a pin at the bottom of the chip carrier, which in turn connects to a matching pin grid array (PGA) socket. The PGA socket allowed for easy switching of microdevices between experiments. Connecting electrical wires were hand-soldered to specific pins at the backside of the PGA socket to electrically connect the microdevice with the input terminals of the computer-controlled data acquisition setup.

Due to the small values of capacitance and capacitance change associated with this measurement, a supporting electrical circuit (Figure 2-2(a)) was implemented in order to create a usable signal that was compatible with the data acquisition hardware. The capacitance sensor (C_{sensor}) was connected in parallel to an RC oscillator circuit containing an operational amplifier, a resistor R_f , a capacitor C_f , and a reference capacitor C_{ref} . A function generator (DS 360) from Stanford Research Systems was used to provide a sinusoidal input signal with a frequency of 200 kHz and amplitude of 7.05 V_{rms} which was connected to the reference capacitor C_{ref} at the negative terminal and sensor capacitor C_{sensor} at the positive terminal. The output of the operational amplifier V_{out} , which is proportional to the capacitance value of C_{sensor} , was recorded by the computer-controlled data acquisition unit (DI-2108, DATAQ Instruments). This sensing scheme is a simplified version of those previously developed by Yazdi et al. [28] and Wei et al. [29] for use in miscellaneous microelectromechanical (MEMS) sensors requiring measurement of small capacitance values.

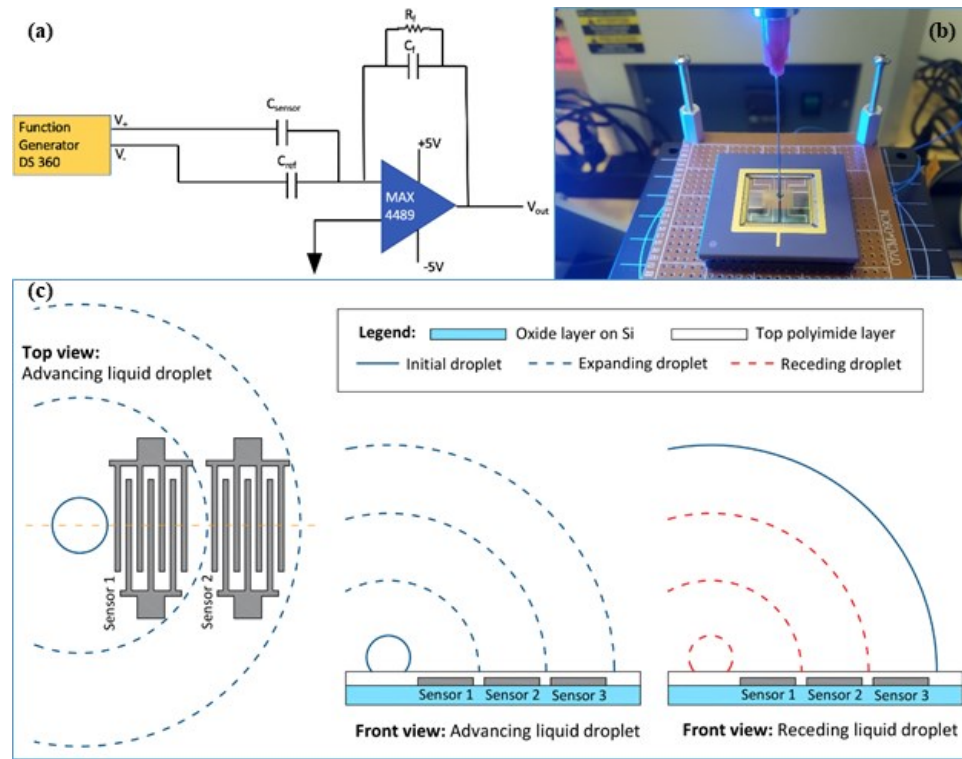


Figure 2-2: (a) Schematic of the sensing circuit (b) Experimental set-up containing capacitance microdevice and chip carrier combo attached to a PGA socket on DSA (c) Conceptual schematic of the expanding and contracting droplet during the experiment.

A drop shape analyzer (DSA 25E, KRÜSS Scientific) provided controlled and repeatable dosing and retraction of water droplets while testing the capacitance sensors. DSA, equipped with advanced analysis software, is a widely accepted method within the fluids community and can be utilized to evaluate the performance of the capacitance sensing scheme. Successive dosing and receding of a water droplet, as shown conceptually in Figure 2-2(c), facilitated a suitable experimental process to detect the location and speed of the MCL. The DSA controlled the advancing and receding movement of liquid droplets through its interactive programmable software, capable of dosing and retracting microscopic amounts of liquid at a rate as low as $0.05 \mu\text{L/s}$. Figure 2-2(b) shows an image of the microdevice and chip carrier assembly on the DSA stage during the testing of the

sensors, where a syringe of diameter 533 mm was attached to the DSA for dosing and retracing of the liquid droplets. For all experiments, the working fluid was deionized water at room temperature. As shown in Figure 2-3, the expanding and contracting of the droplets was accomplished in a precise manner via changes in the DSA's automated program such that it would induce a controlled and measurable time difference in when the MCL would pass over adjacent capacitance sensors. This allowed for assessing the accuracy of the capacitance sensor array in determining the MCL's speed and location, verified by an optical camera controlled by the DSA.

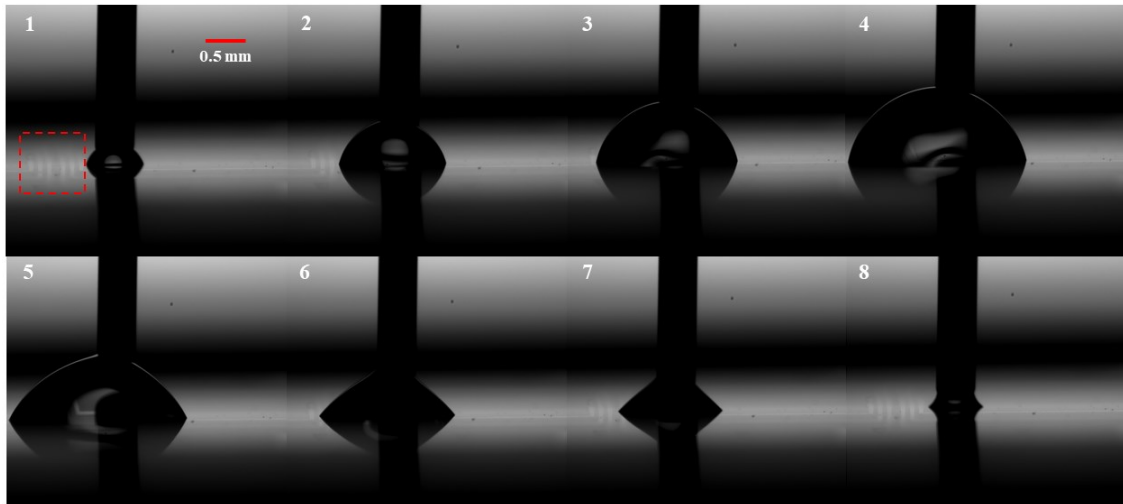


Figure 2-3: Collaged images showing dosing (Images 1-4) and retraction (Images 5-8) of an unconstrained deionized water droplet during the testing of the sensors. The dashed rectangle in image 1 shows the capacitance sensor array (CS-1 through CS-6).

In terms of measurement uncertainty, the voltage measurement resolution of DI-2008 data acquisition unit was $76.3 \mu\text{V}$ for the voltage measurement range of $\pm 2.5 \text{ V}$ utilized here. The lower limit of sampling interval was one millisecond for the DI-2008, although 50 milliseconds was used in this work as it was found to provide more than adequate MCL detection without creating unnecessarily large data files. As will be shown

in the following results, experiment noise led to a lower limit of capacitance change detection of 0.2 fF or roughly 0.01% of the measured capacitance signal in the dry state, while spatial resolution of the measurement was determined to be 40 μm . For all experimental investigations reported in this dissertation, each experiment was repeated at least three times to ensure reliability, and the data reported represents the best outcomes out of the three trials conducted.

2.3 Results and Discussions

Figures 2-4 to 2-6 demonstrate the relative capacitance change over time for MCL's advancing and receding movement for unconstrained deionized water droplets. Each experiment reported in these plots comprised multiple cycles of dosing and retraction of the droplet performed using the DSA equipment. Figure 2-4 (a) shows that the capacitance sensors (CS) CS-1 and CS-3 were individually able to track the location of the MCL as it passed over each sensor. The MCL speed can be determined by using the time lag between two sensors and their known spatial separation. The timing of these events also correspond to when the droplet edge was observed to pass over the sensor regions in the video taken from the DSA tool, thus serving to confirm functionality. For a single cycle of dosing, the water droplet first moves over CS-1 and causes an increase in capacitance signal, while the capacitance signal of CS-3 remains unaffected until the droplet passes over it. During the retraction, the water droplet first moves away from CS-3 and decreases its capacitance signal, while the capacitance signal of CS-1 remains unchanged until the droplet completely moves away. The experimental data presented in these plots were the relative change in capacitance, in which the change in capacitance for each sensor was normalized to its initial capacitance value in the dry state when no droplets were present in the sensing

region. While all six sensors are geometrically identical and have an average capacitance of 175 fF, there is some sensor-to-sensor variation (approximately ± 20 fF) in their initial capacitance values measured in the dry state due to small differences in parasitic capacitance present via on-chip traces, connectors, lead wires, etc. The influence of parasitic capacitances on the measurement of small capacitance signals is a common phenomena within the literature [29]. However, since this work only seeks to exploit an observed *change* in capacitance with MCL movement, the influence of these parasitic capacitances do not hinder the experiment so long as the capacitance *change* can still be measured by the associated circuit and data acquisition hardware. Hence, normalizing the data emphasizes these capacitance changes and is more relevant to the measurement's intended usage than plotting results as the absolute magnitude of capacitance.

When two adjacent sensors were employed to perform the same experiment, this resulted in an evident proximity effect in which the relative change in capacitance was reduced for one sensor and increased for another due to inter-sensor coupling. An example of this phenomena can be seen by comparing the data in Figure 2-4(a) in which CS-1 and CS-3 are utilized (158 μm separation distance) versus Figure 2-4(b) in which the same experiment was conducted but with CS-1 and CS-2 (38 μm separation distance). The sensor couple comprised of CS-1 and CS-3 detects the speed and location of the MCL more distinctively than sensor couple of CS-1 and CS-2 because of the greater distance between the sensors. However, the change in capacitance is still measurable even for the CS-1/CS-2 pair, which makes the approach of utilizing neighboring sensors to detect the location and speed of the MCL viable.

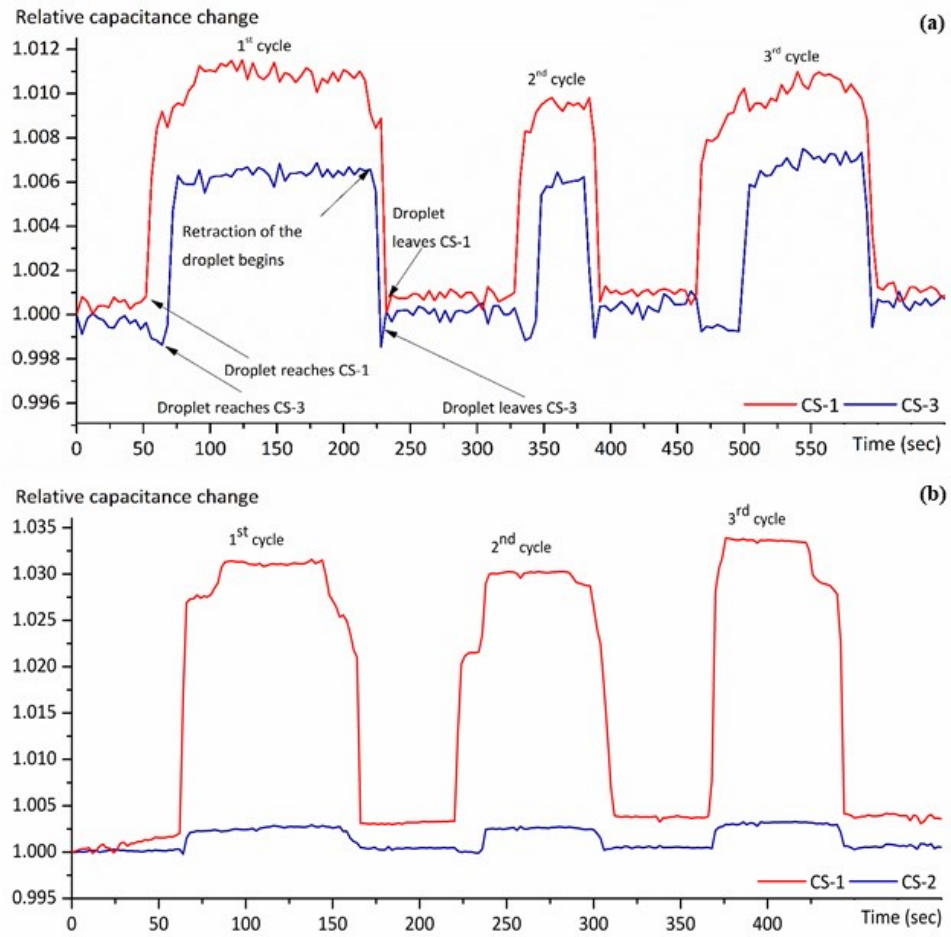


Figure 2-4: Measured capacitance signal for advancing and receding water droplets with (a) sensor couple contains CS-1 and CS-3, (b) sensor couple consists of CS-1 and CS-2. (Due to a sampling frequency of 30 Hz, the discrete data points in the plots are closely spaced, appearing as continuous lines. For clarity of presentation, lines are used instead of discrete data points.)

Based on the experimental data, the number of sensors being utilized significantly influenced the proximity effect but did not prevent effective tracking of MCL. Figure 2-5(a) shows an approach of utilizing three capacitance sensors (CS-1/CS-3/CS-6) simultaneously. Here, the middle sensor (CS-3) shows an inverted but still detectable signal. According to Figure 2-5(b), disconnecting CS-1 from the function generator led to adequate detection of the MCL for the same experiment with the sensor couple CS-3/CS-

6, where the distance between the two sensors is $336\text{ }\mu\text{m}$. In addition, the signal from CS-3 inverts to resemble that previously observed for the two-sensor experiments in Figure 2-4. Besides demonstrating the utility of using three sensors, the cumulative data shown in Figure 2-5 regarding the effect of disconnecting CS-1 is effective proof of sensor proximity coupling as a real but manageable phenomenon.

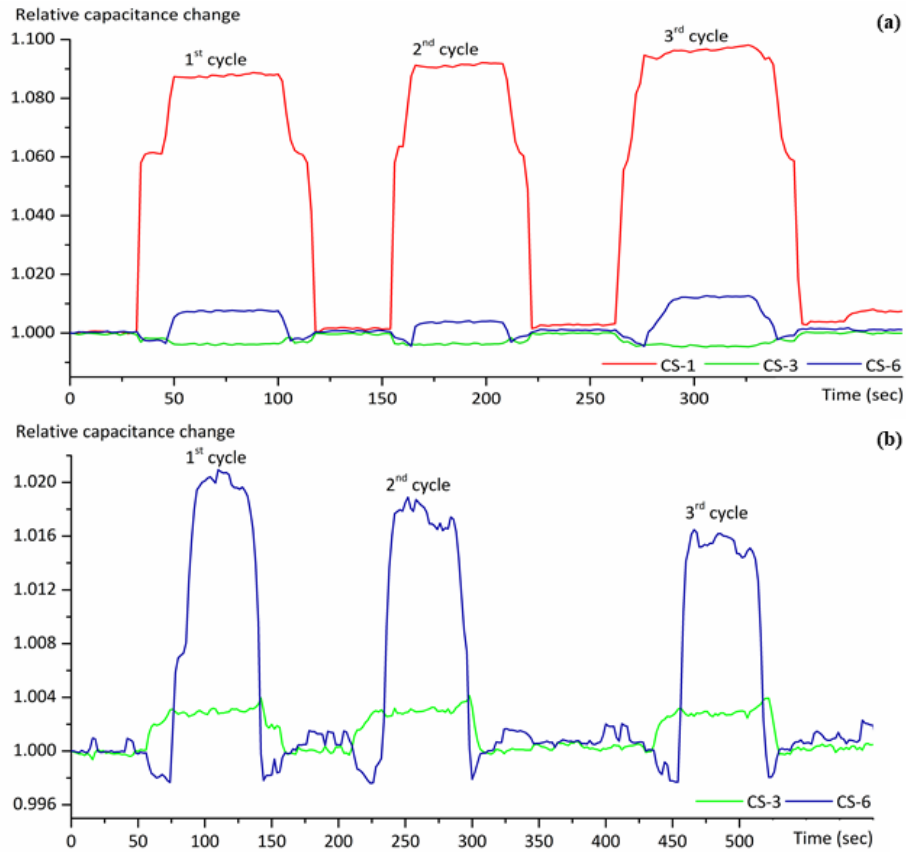


Figure 2-5: Measured capacitance signal for dosing and retraction of water droplets by using (a) three capacitance sensors CS-1, CS-3, and CS-6, (b) two capacitance sensors CS-3 and CS-6.

Utilizing three consecutive sensors (CS-1/CS-2/CS-3) where the sensors are only $38\text{ }\mu\text{m}$ apart, representing the maximum spatial resolution achievable with this array design, resulted in the most extreme case of sensor proximity. As Figure 2-6 shows, this approach causes the inversion of capacitance signal for CS-2 and CS-3 and a signal strength

that is small compared to the noise level. However, the change in capacitance and, hence, the passage of the MCL is still detectable. This experiment then represents the limit of spatial resolution achievable for the given array design and sensing circuit, which is approximately 40 μm . It also demonstrates, based on the observed noise level, the lower limit of capacitance change detection of 0.2 fF or roughly 0.01% of the measured capacitance signal in the dry state.

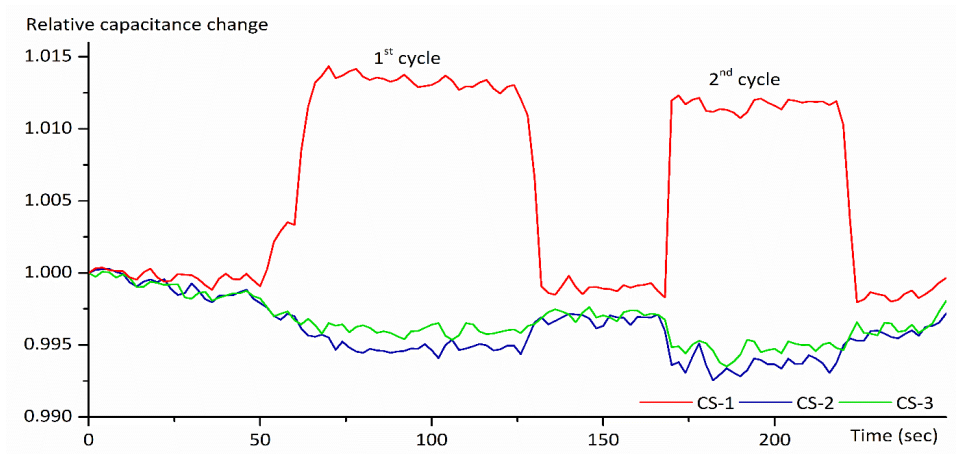


Figure 2-6: Measured capacitance signal for dosing and retraction of water droplets by using CS-1, CS-2, and CS-3 simultaneously.

The above results demonstrated that each capacitance sensor can efficiently track the MCL's location individually and in use with other sensors, whether the coupled sensors are adjacent or located farther away within the sensor array. MCL speed can be calculated by utilizing the known spatial separation between any two sensors and the time required for the MCL to travel that distance. For example, as shown in Figure 2-5(b) for the first cycle of dosing the water droplet reached the first capacitance sensor (CS-3) at $t_1 = 57.2$ s and was detected to reach CS-6 at $t_2 = 75.0$ s, which led to the calculation of speed of the multiphase contact line by using $v = \Delta x / \Delta t$, where Δx is the distance travelled by the

MCL and $\Delta t = t_2 - t_1$ is the time spent to travel the distance. This provides an MCL speed of 23.5 $\mu\text{m/s}$. This value is in good agreement with the MCL speed of 24.3 $\mu\text{m/s}$ estimated via video taken by the DSA. The good agreement between these numbers helps validate the IDE capacitor array as a viable means of MCL location detection and speed measurement, especially in applications where visibility for optical methods is not possible or for which measurements at multiple locations simultaneously is desirable.

Apart from providing controlled dosing and retraction of small-scale water droplets, another vital functionality of DSA was to measure the droplet diameter as well as the advancing and receding contact angle of the water droplets on the polyamide top layer. As shown in the representative data in Figure 2-7(a) taken from the single cycle of a given experiment, during the dosing of the water droplet via DSA the droplet diameter gradually increased, then decreased during retraction as expected.

The approach presented here has additional utility in its ability to estimate both the advancing and receding contact angle from the measured capacitance changes in time. Using the data in Figure 2-5(a) as an example, there is a measurable difference between the slopes of the advancing and receding capacitance change signals used in detecting the MCL. The relative capacitance change data of CS-1 demonstrates an average value of 0.133 s^{-1} for the slope of three dosing events, where the average value of the three retraction events is 0.071 s^{-1} . Thus, the slope of the dosing capacitance signals is 1.87 times higher than that of retracting signals. The contact angle ratio obtained from the DSA measurements in Figure 2-7(b) provides a value of 1.89, which comes from an average advancing angle of 73.88° and an average receding angle of 39.06° . The ratio of the slopes for advancing and receding capacitance signal (1.87) closely matches the ratio of the

advancing and receding contact angles observed via the DSA (1.89), which suggests that the rate of capacitance change scales with the contact angle. In principle, it is possible to use this measurement technique to get the actual value of advancing and receding contact angles from the slopes of the advancing receding capacitance change signals rather than just their ratio. This is important, as it is typically the contact angle values themselves rather than their ratio that is of greater importance within the field. The key to doing so would be to have sufficient existing data to confidently establish the quantitative relationship between capacitance signal slope and contact angle over the range of contact angles of interest. Here, this study is limited in this respect as it has only two data points for establishing this relationship: one for advancing and one for receding. If this experiment were to be repeated with water/surface relationships which gave additional contact angles, a reliable calibration curve for advancing and receding contact angles versus capacitance slope could be established with sufficient data points to elucidate the relationship. With this calibration available, the values of advancing and receding contact angle could be sensed with confidence without the need of optical verification. Thus, similar to the speed measurement, with additional calibration and improvements it may be possible to utilize IDE arrays such as those presented here as a means of determining the advancing and receding contact angles of droplets in applications where visibility for optical methods is not possible or for which measurements at multiple locations simultaneously is desirable. In its current implementation, this study estimates the overall relative uncertainty in contact angles that could be derived from the microsensor array to be approximately 19.9%, which was arrived at by combining the relative uncertainties in the DSA-measured contact angle and that of the capacitance change slope data. For the case of the most utilized contact

angle measurement span of 110° , this would equate to a contact angle measurement uncertainty of approximately 22° . However, the dominant component to the combined uncertainty lies with the noise in the microsensor array's support circuitry. With further improvements in the support circuitry, it is possible to get the overall relative uncertainty in contact angles derived from the microsensor array to be $\sim 10\%$. Taking this over the same 110° span as before would equate to a contact angle measurement uncertainty of approximately 11° .

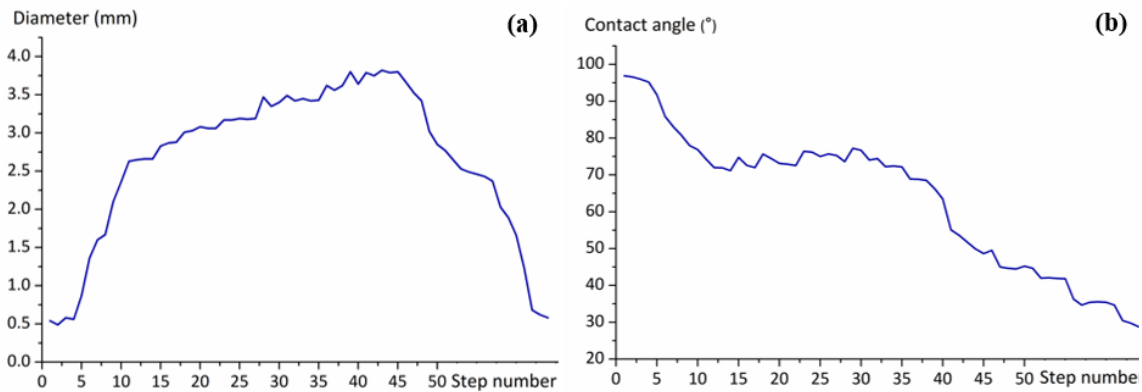


Figure 2-7: (a) A diameter vs. step number plot acquired via DSA: change in diameter denoting dosing and retraction of water droplets during the experiment (b) Plot of contact angles with step number for water droplets on polyimide surface.

It is worth mentioning that, in this study, the interaction among the water droplets and the topmost polyimide layer of the microdevice was hydrophilic such that the MCL was the first region of the droplet to reach the IDE sensor array during dosing and the last region of the droplet to leave the array during retraction. In contrast, for the case of a strongly hydrophobic droplet expanding over the sensor array there would be expected to be a time difference between when the foremost part of the advancing droplet passes over the array and when the MCL reaches the first IDE. A similar time difference but in reverse would occur during retraction. The magnitude of this time difference and the degree to

which this impacts the measurement would depend on how strongly hydrophobic the droplet/surface interaction is as well as how tall the penetration depth T is relative to the size of the droplet being measured.

2.4 Summary of Findings

This work presented a capacitance-sensing microdevice based on interdigitated electrodes for detecting the speed and location of moving contact lines for unconstrained water droplets. The functionality of the sensing scheme was validated against observations made via a commercial drop shape analyzer optical tool. Besides tracking bidirectional (advancing and receding) MCL movement, this sensor represents a minimally intrusive, low-cost, and scalable scheme of phase interface sensing. The approach of implementing multiple sensors within close proximity has provided efficient detection of MCL to within 40 μm spatial resolution. Employing more than two sensors for capacitance sensing without adequate spacing was observed to lead to sensor coupling effects that should be minimized but did not prevent effective MCL tracking. The capacitance sensor array exhibited the ability to accurately measure MCL speed via comparison against video taken during experiments. Further, it was shown that the rate of change of capacitance signals scale with the advancing and receding contact angles observed via optical measurements. Although future research is required to minimize parasitic capacitance and coupling effects, the results presented here demonstrate a novel new approach to MCL sensing, which can facilitate new discoveries in many application areas where optical methods are limited.

Future research on this capacitance sensing for unconstrained droplets should prioritize enhancing signal detection and spatial resolution. The main focus should be to

attain adequate capacitance signal strength from multiple sensors in adjacent proximity while reducing or eliminating the adverse effects of coupling and parasitic capacitance. In addition, facilitating the reliable detection of smaller capacitance changes would reduce the necessary size of a given IDE and improve spatial resolution. In terms of facilitating new science or applications, this sensor may be able to be effectively employed in heat transfer studies involving condensation or evaporation, where the IDE array would provide insights into MCL location, speed, and the contact angles with microscale resolution even in environments for which optical methods are not possible. In addition, facilitating the reliable detection of smaller capacitance changes would reduce the necessary size of a given IDE and improve spatial resolution. In terms of facilitating new science or applications, this sensor may be able to be effectively employed in heat transfer studies involving condensation or evaporation, where the IDE array would provide insights into MCL location, speed, and the contact angles with microscale resolution even in enclosed environments where optical methods have limited visibility.

CHAPTER 3

SPEED AND LOCATION TRACKING OF MOVING MULTIPHASE INTERFACES VIA A CAPACITANCE MICROSENSOR ARRAY DURING DROPLET EVAPORATION

3.1 Introduction and Motivation

In a three-phase system, like evaporating droplets on a heated surface or bubble nucleation in pool boiling environments, the MCL occurs at the interface of the solid wall, liquid, and gas phases. This three-phase contact line can move along the solid surface as the individual bubble nucleates and departs, and droplets evaporate away. MCL has been a subject of extensive experimental and analytical studies because of its ubiquity in interfacial science and many engineering fields, including but not limited to microfluidic devices, various coating and printing technologies, phase-change heat transfer systems, two-phase flows in porous media, and nucleate boiling [21], [30]–[33]. The strong temperature and density gradients in the vicinity of MCL and its mobile nature make it a significant factor in determining the overall heat transfer characteristics of the phase change process. As a result, the MCL behavior has also been widely investigated in recent years as it is the region that facilitates the highest heat transfer in evaporative or other phase-change heat transfer processes [1], [11], [34]–[36]. In terms of thermal management applications, the widespread utilization of multiphase cooling strategies to handle high heat flux densities means that insights gained into the behavior of the MCL, and its associated thermal impacts can lead to improved cooling devices, processes, and effectiveness via

informed surface engineering. In many phase-change heat transfer processes like nucleate boiling and droplet evaporation, studying MCL behavior has been essential, as temperature data alone does not provide a comprehensive understanding. Thus, it is crucial to correlate the heat transfer mechanisms with the MCL behavior to reveal the underlying physics behind these processes [3], [15], [36], [37].

Despite being the most commonly used technique within the literature, optical sensing has certain limitations, where electrical sensing has emerged as the preferred choice due to its higher precision, greater stability, and broader applicability at the microscale, especially in environments with limited visibility, such as within heat exchangers and vapor chambers [16], [19]. Optical techniques possess low sensitivity and throughput, often require bulky and complex setups, and are unsuitable for close-packed integration. On the other hand, electrical detection comprising resistive and capacitance sensing facilitate high sensitivity, scalability, transient response, low cost, and compatibility in compact integration [38]–[40]. Resistive and capacitive sensing have been most prominent in electrical techniques, with some important differentiators between the two types. Resistive sensing has some known limitations including requiring a continuous conductive phase in the sensing region and intricate patterns to achieve effective performance [19]. On the contrary, capacitance-based sensing only requires a spatial separation between two coplanar electrodes as the basic sensing element and can be easily scaled down to smaller feature sizes due to its less complicated geometry requirements [23].

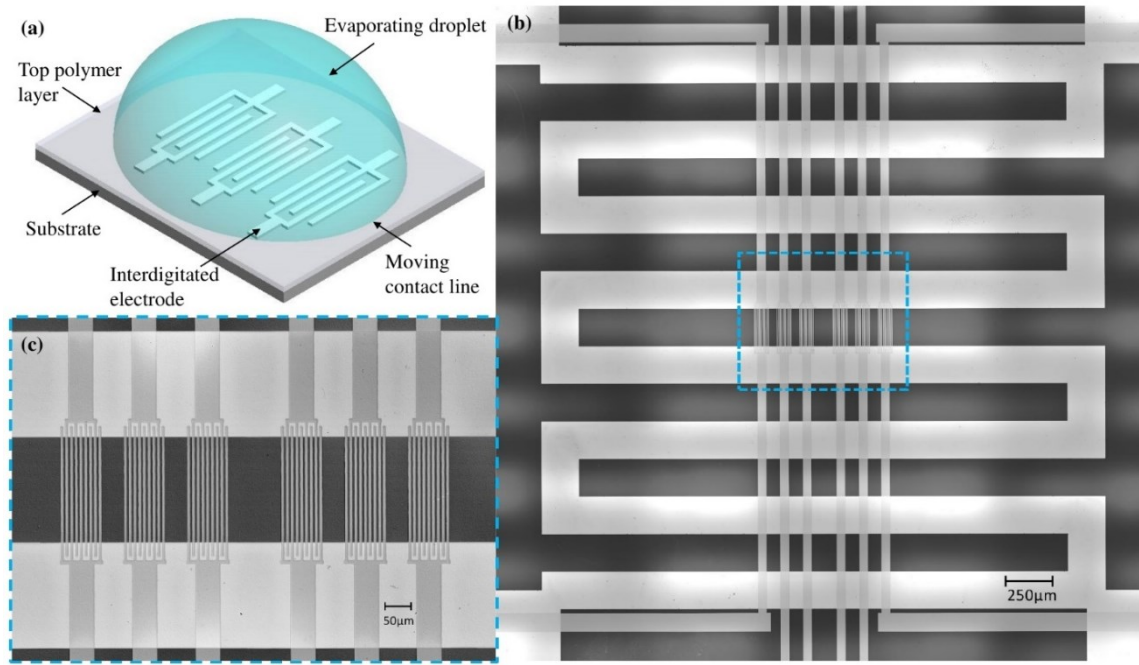


Figure 3-1: (a) A conceptual illustration of the capacitive sensing scheme (not to scale). (b) A laser-microscopic image of the microdevice showing resistance heater and capacitance micro-sensor array. (c) A detailed view of the sensing zone enclosed by the dashed box in (b) showing six capacitance sensors based on interdigitated electrodes. The resistance heater and interdigitated electrodes are on separate device layers and separated by a polymer thin film as described in the main text.

This work presents a capacitance-based microdevice that can precisely track MCL's location and speed at elevated temperatures for real-life applications such as droplet evaporation. The study also investigates how substrate material affects its performance. As shown in Figure 3-1, the microdevice is comprised of a total of six capacitance micro-sensors based on coplanar interdigitated electrodes (IDEs) with a thin insulating polymer layer on top. This approach also facilitates a bulk micro-fabrication compatible means of sensing phase interface such that many sensors can be created at one time. Unlike existing optical methods used previously in literature [11], [13], [41], this micro-sensor array approach does not require visual access to the surface under study such that MCL tracking can occur within opaque hardware or enclosures. Previous work on tracking MCL location

via this type of sensing scheme on a semiconducting substrate was shown to be effective for simple aspirated water droplets but also demonstrated certain nonidealities, particularly in terms of capacitive coupling effects between sensors in close proximity [18]. Here, this study reports on significant improvements by utilizing a dielectric substrate, including but not limited to obtaining a much stronger capacitance signal output from multiple sensors in adjacent proximity with reduced coupling effects. The motivations behind choosing soda-lime glass as the alternate substrate are its cost-effectiveness and broad applicability in microfluidic and other MEMS devices. Soda-lime glass substrates are also widely implemented as they provide advantages over other materials in terms of high electrical insulation, surface stability, high resistance to mechanical stress, and compatibility with a wide range of microfabrication techniques [42]–[44]. This study also reports data for the moving MCL of an evaporating water droplet for the first time to demonstrate this approach's functionality at elevated temperatures and during a dynamic heat transfer process.

3.2 Methodology

3.2.1 Operating Principle

The phase interface sensing microdevice works based on the operating principle that when droplets or MCL pass over the sensing region, they cause a change in the relative permittivity/dielectric constant of the area. The variation of relative permittivity/dielectric constant causes a detectable change in the measured capacitance signal in the sensor array [16], [18], [19]. Apart from the relative permittivity of the medium $\epsilon_{r,eff}$, the capacitance C of the sensor array depends on the width w and spacing $2a$ between two consecutive coplanar electrodes. Figure 3-1(a) demonstrates a schematic illustration of the capacitive

sensing scheme, where electric field lines between two planar electrodes extend above the thin insulating layer to interact with the motion of MCL as the liquid droplet passes over it. These electric field lines are caused by an applied sensing voltage to the electrode pair. The sensing range of the electrical field from the top surface of the IDEs (referred to as the penetration depth T) also varies with the width w and spacing $2a$ between two consecutive coplanar electrodes. For more details on how this device works, please refer to the “Microdevice Overview” section in Chapter 2.

3.2.2 Microdevice Overview

The capacitance sensor design presented in this study comprises six capacitance sensors, as shown in Figure 3-1, each comprising an IDE pair. The geometry of the IDEs, including the width, spacing, and interaction length, significantly influences the sensitivity or strength of the capacitance signal and penetration depth of the electric field lines. The measured capacitance and penetration depth increase with the increasing width of the electrodes. However, the capacitance decreases with increasing spacing between electrodes. The strength of the capacitive signal also increases with the number of electrodes and their interaction length [27]. Although increasing width, interaction length, and the number of electrodes would enhance the sensitivity of the sensing scheme, it would also reduce the spatial sensitivity of the microdevice because of its increasing physical dimensions. Narrower spatial separation between two consecutive electrodes will also lead more challenging microfabrication and a reduction in the number of defect-free devices. Hence, a balanced approach has been implemented during the device design to facilitate a workable compromise between magnitude of the capacitive signal, penetration depth, desired spatial resolution, and high yield microfabrication. The final IDE array design shown in Figure

3-1(b-c) has an electrode width of $w = 6 \mu\text{m}$, spacing between two consecutive electrodes $a = 3 \mu\text{m}$, and an interaction length of $l = 250 \mu\text{m}$.

3.2.3 Microfabrication Process

This work involved the fabrication of two identical capacitance-sensing microdevices on different substrate types in investigating the influences of substrate materials on the performance of the MCL tracking microdevices. Two different substrate materials were used: a) a semiconducting base- commercially available single-side polished $500 \mu\text{m}$ thick boron-doped ($1 \times 10^{16} \text{ cm}^{-3}$) silicon wafer, and b) a soda-lime glass wafer of similar thickness as the dielectric base. The microfabrication of the capacitive micro-sensor array consisted of photolithography, deposition of platinum (Pt), spin-coating of a thin insulating polyimide top layer, and selective etching/patterning of the deposited polymer layer by reactive-ion etching. To enable a heated surface during the droplet evaporation testing, a 100 nm thin film of Pt was deposited and patterned as a resistance heater directly on top of the starting substrate via photolithography and DC sputtering deposition. A $1.2 \mu\text{m}$ thin film of the polyimide was deposited between the resistance heater and the IDEs arrays via spin coating of the diluted polyimide (75% PI-2661 + 25% NMP) to provide an electrically insulating layer. Microdevices that were not intended for evaporation studies did not include these processing steps and instead began with the IDE microfabrication steps that follow. To create the IDE sensing array, a 70 nm thin film of Pt was deposited and patterned via DC sputtering in an AJA ATC sputtering system with a commercially available Pt target. A spin-on polymer of polyimide (PI-2611) was obtained from HD Microsystems which can be diluted with the addition of N-Methyl-2-Pyrrolidone (NMP) to achieve thinner layers. A 440 nm thin film of polyimide was deposited on top of

the deposited Pt layer via spin coating of the diluted polyimide (50% PI-2661 + 50% NMP) in a closed-bowl spin coater. The 440 nm thick polyimide layer was chosen to ensure a balanced approach of increasing the sensitivity of the microdevice and providing a thick enough protective coating atop the Pt layer to prevent it from creating surface protrusions. A reactive ion etching (RIE) process was used to selectively etch the polyimide layer to open the contact windows at the device periphery to ensure wire bonding between the diced microdevice and the commercially available chip carrier.

3.2.4 Signal Processing

After dicing, the microdevice was secured at the ceramic chip carrier's cavity, where the microdevice's contact pads were wire bonded with the corresponding contact pads of the carrier. The microdevice and chip carrier assembly interfaces with a computer-controlled data acquisition system through a pin grid array (PGA) socket. A supporting sensing circuit was employed to translate capacitance changes into voltage readings and to ensure a measurable change in signal magnitude, as the capacitance changes related to this sensing scheme can be relatively small. As shown in Figure 3-2(b), the supporting circuit contains an RC oscillator couple, an operational amplifier, and a reference capacitor connected in parallel with the sensing IDE capacitor. The planar interdigitated electrode arrays used for the six capacitance micro-sensor are identical in geometry and have an average capacitance of 175 fF before the experiments in the dry state with approximately 14% of sensor-to-sensor variation. Observation of the noise level indicates that the lower limit of detecting capacitance changes is 0.2 fF, which is approximately 0.11% of the average capacitance of the microsensors in the dry state. It is important to mention that an edge-triggered

digitization scheme or signal inverter would enhance the clarity of the measured signal if the only purpose were to detect the presence of droplets in the sensing region.

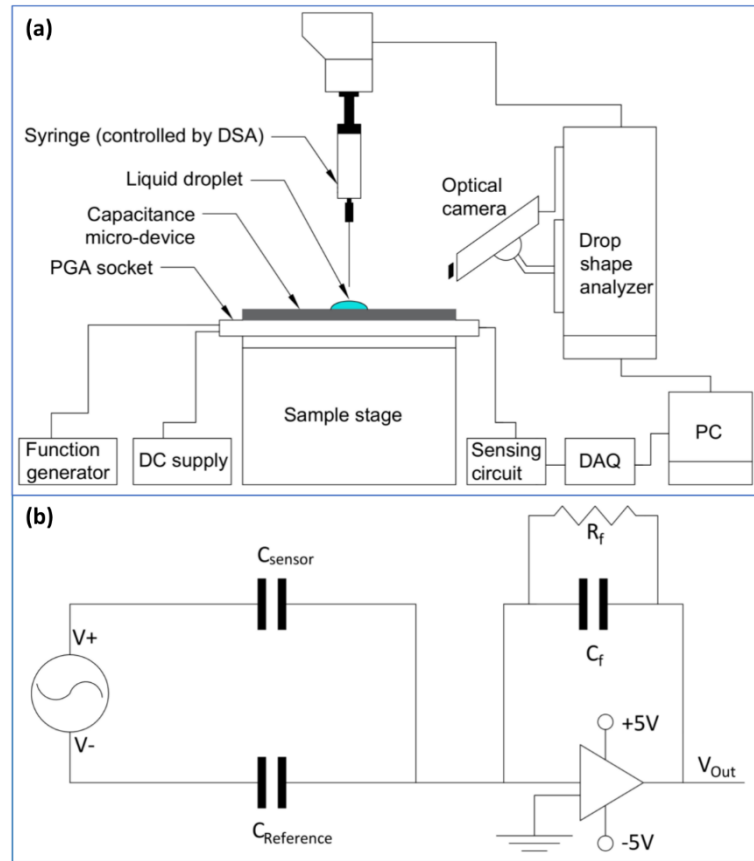


Figure 3-2: (a) Schematic of the experimental setup for tracking speed and location of MCL with a capacitance-based phase interface sensing microdevice, (b) Schematic of the supporting electric circuit used for each IDE electrode pair.

3.2.5 Experimental Setup

As shown in Figure 3-2(a), the experimental setup comprised the sample stage holding the microdevice below a syringe controlled by a drop shape analyzer (DSA 25E, KRÜSS Scientific). The DSA provided controlled dosing and retraction of deionized water droplets during initial aspiration experiments that did not involve a heated substrate for droplet evaporation, and controlled deployment of a known starting droplet size for the

evaporation studies that followed. An optical camera attached to the DSA also monitored the macroscopic behavior of the MCL, which served to validate that the microdevice array was functioning as intended. The captured images/videos via DSA shown in Figures 3-3 and 3-4 also facilitated a usable comparison of the MCL speed between the microdevice and the optical technique. Simple dosing and retraction without substrate heating (i.e. aspiration) was first utilized to study the impact of substrate material on sensing behavior. Once the dielectric substrate was found to be superior through these early studies, evaporating droplet testing at elevated device temperatures was performed. For ensuring elevated surface temperature during the droplet evaporation experiment, the thin film resistance heater of the microdevice was powered with known voltage and current from a DC power supply. Before dosing the water droplet, the resistance heater was powered by a set electric input power via the DC supply to attain the desired surface temperature of the microdevice. The DSA provided controlled dosing of the water droplet at various surface temperatures and recorded the entire evaporation process that followed. The calibration of surface temperature at various electric power inputs to the resistance heater was carried out by employing an IR camera (FLIR A300) and a commercially available thermocouple, with the latter being in good thermal contact with the center of the device. After conducting all relevant experiments, the surface temperature calibration was performed to avoid any undesirable damage to the sensing region of the microdevice.

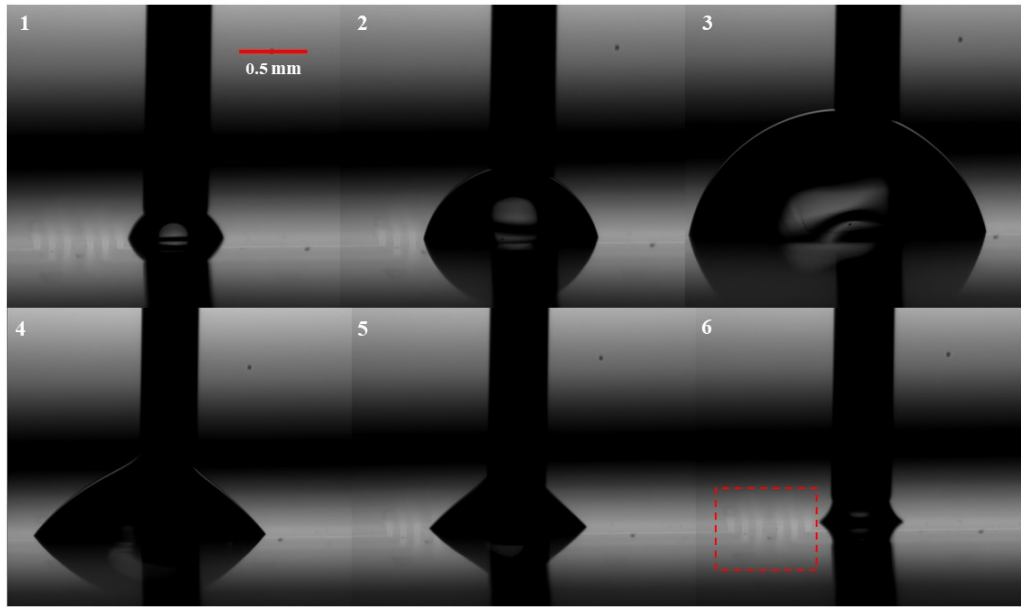


Figure 3-3: Optical images of gradual dosing (Images 1-3) and retraction (Images 4-6) of a water droplet captured by the drop shape analyzer tool during initial aspiration experiments on substrate effects. The dashed box in Image 6 shows the location of the sensing zone of the microdevice comprising six capacitance micro-sensors CS-1 to CS-6 (numbered left to right).

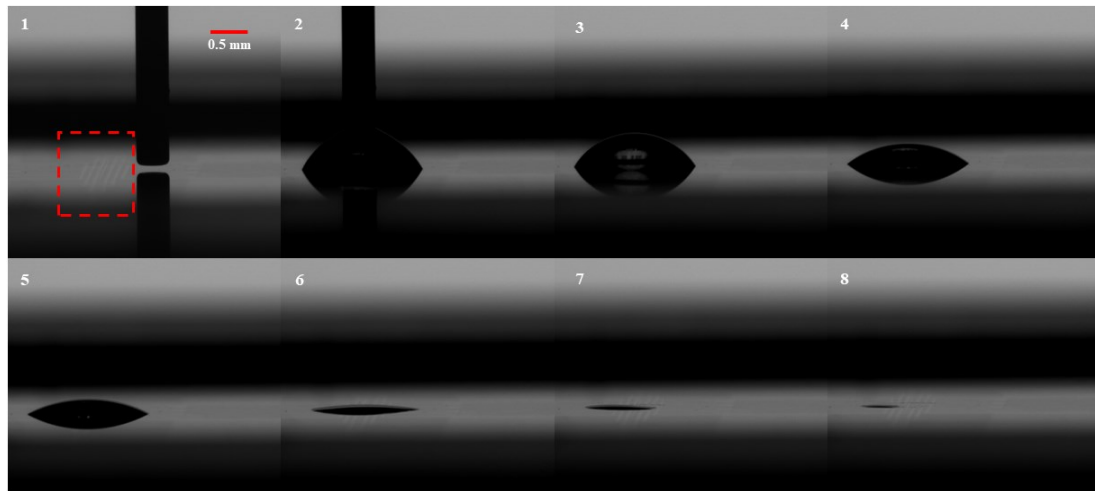


Figure 3-4: Optical images of the evaporation process of a water droplet captured by drop shape analyzer equipment during the experiment. The dashed box in Image 1 shows the location of the sensing zone of the microdevice.

3.3 Results and Discussion

The experimental results show the normalized capacitance change over time for dosing and retraction of deionized water droplets measured by identical microdevices based on a semiconducting (doped silicon) and a dielectric (soda-lime glass) substrate. Figure 3-5 demonstrates the changes in capacitance signals for the capacitance micro-sensor array deposited on a silicon substrate. As Figure 3-5 shows, during dosing of the water droplet, the MCL associated with the droplet's leading edge first moves over capacitance sensor CS-1 and causes an increase in signal. The MCL next reaches capacitance sensor CS-6, which also demonstrates a rise in capacitance signal with the passage of the MCL. These events are reversed when the water droplet leaves the sensing zone of the microdevice. This effectively demonstrates the basic measurement principle of measuring the capacitance changes with time as the MCL passes over the capacitance sensors. The four dashed boxes shown in Figure 3-5 demonstrate the MCL's significant advancing and receding movement toward and away from the sensors employed during the experiment. The optical images on top of Figure 3-5 represent MCL's corresponding fundamental movements, while the collaged images shown in Figure 3-3 exhibit the overall aspiration experiments comprising gradual dosing and retraction of water droplets. All capacitance change data presented in this work has been normalized relative to the initial capacitance signal before the experiment when only air alone was present over the sensing zone.

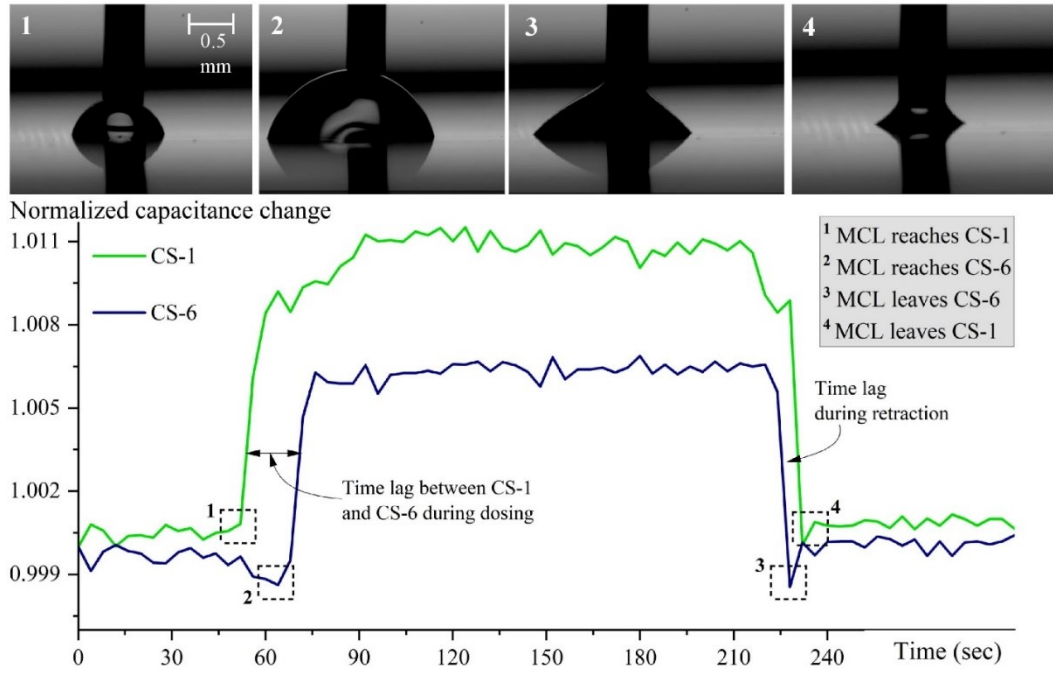


Figure 3-5: Measured normalized capacitance changes for advancing and receding deionized water droplets using the sensor pair CS-1 and CS-6 on a doped silicon substrate, where the dashed boxes denote the significant movements of MCL as shown in the optical images on top.

The timing of the observed capacitance changes is in good agreement with the gradual dosing and retraction of the water droplets shown in Figure 3-3, confirming the measured capacitance changes are because of the passage of the MCL of the dosed droplets. Besides indicating MCL location at a specific time, the measured capacitance changes also enable measurement of MCL speed by utilizing the time lag shown in the graphs and the known spatial separation between the capacitance sensors. For example, as shown in Figure 3-5, during dosing the water droplet first reached CS-1 at $t_1 = 52$ s and the change in capacitance signal for CS-6 was detected at $t_2 = 64$ s. Utilizing the known distance between CS-1 and CS-6 ($\Delta x = 658$ μm) and the time lag ($\Delta t = t_2 - t_1 = 12$ s) the speed of the MCL was calculated as 54.8 $\mu\text{m/s}$ by applying $v = \Delta x / \Delta t$.

Although capacitance sensing with the microdevice based on a doped silicon substrate demonstrated effective sensing, it exhibited undesirable sensor proximity effects, especially in the case of simultaneous implementation of three or more (out of six total) capacitance sensors. As an example, Figure 3-6 shows the normalized capacitance changes for capacitance sensors CS-1, CS-3, and CS-6 on a doped silicon substrate, where the capacitance signal from the middle sensor is inverted from the expected trends shown in Figure 3-5. This signal inversion did not cause any interruptions in the ability to track the MCL as the signal response is still present even with inverted trend, but still represents an undesirable effect on the signal.

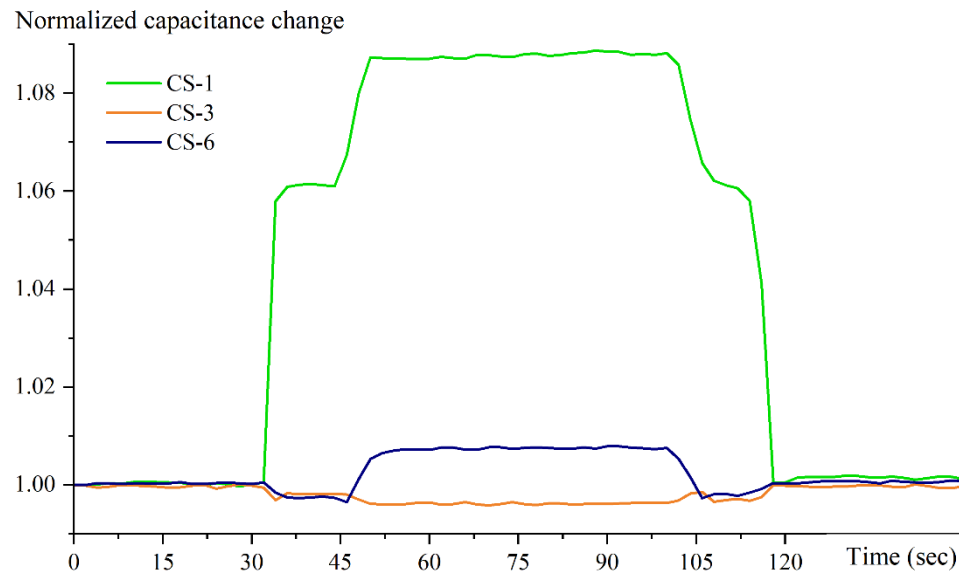


Figure 3-6: Normalized capacitance changes with time for advancing and receding deionized water droplets using capacitance micro-sensors CS-1, CS-3, and CS-6 with the microdevice based on a doped silicon substrate.

Implementing the identical sensing device based on a dielectric soda lime glass substrate demonstrated that the measured capacitance signal underwent less proximity effect that caused the inversion of the capacitance signal. The substitution of soda lime glass for

doped silicon facilitated well-ordered capacitance signals and enabled increased relative change in capacitance compared to its semiconducting counterpart as shown in Figure 3-7, where the same sensor combination from Figure 3-6 (doped silicon) was used for capacitive sensing.

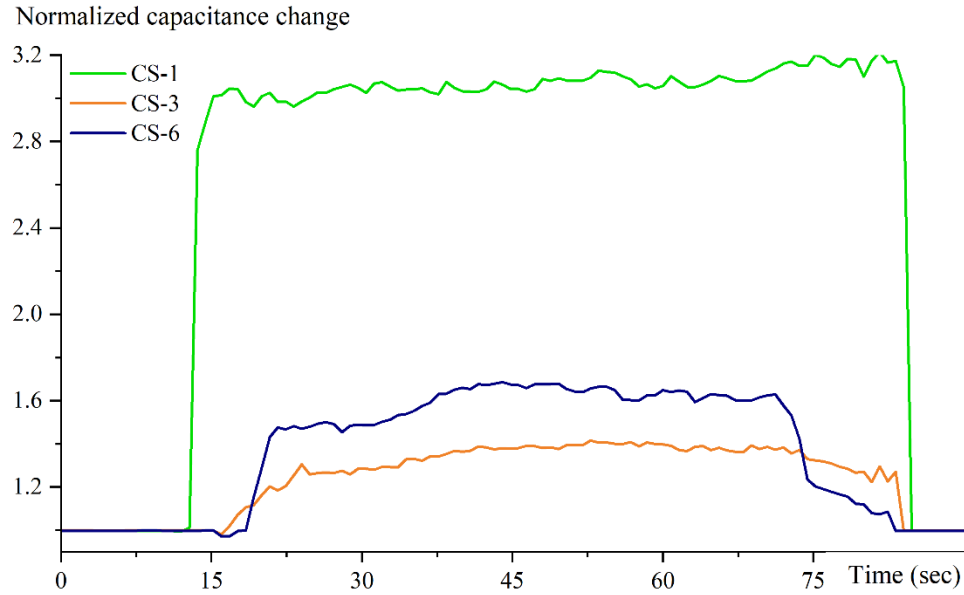


Figure 3-7: Normalized capacitance changes with time for advancing and receding deionized water droplets using capacitance micro-sensors CS-1, CS-3, and CS-6 with the microdevice based on a soda-lime glass substrate.

Based on results from the previous doped silicon substrate experiments [18], a sensor triplet comprising CS-1, CS-2, and CS-3 represents the most extreme scenario of sensor proximity effects where two out of three capacitance sensors exhibited inversion in their capacitance signals. Figure 3-8 illustrates the relative change in capacitance for this sensor combination for doped silicon, where CS-1 still shows an uninterrupted detection of the spatial location of the MCL. The semiconducting base of the microdevice and the small spatial separation ($\sim 40 \mu\text{m}$) among these immediately adjacent sensors are the major causes of this inversion, which constrained their simultaneous implementation in tracking MCL.

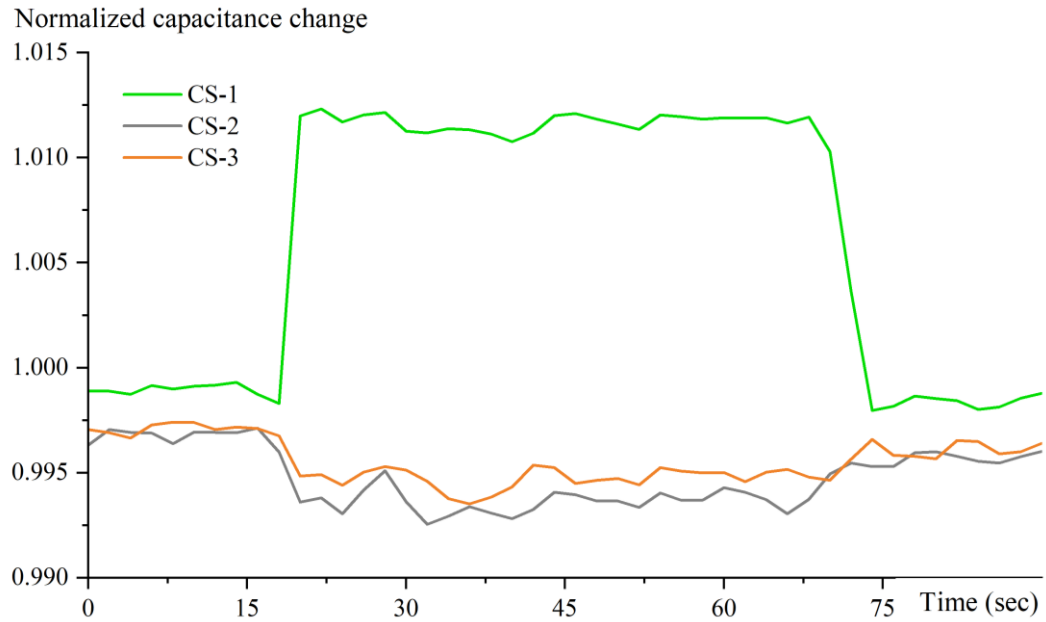


Figure 3-8: Normalized capacitance changes with time for advancing and receding deionized water droplets using three capacitance micro-sensors (CS-1, CS-2, and CS-3) in adjacent proximity with the microdevice based on a doped silicon substrate.

In comparison, implementing the identical sensing device based on a dielectric base instead of the semiconducting one improved measured signals and reduced coupling effects, with only one sensor providing inverted signals, as shown in Figure 3-9. As this data indicates, the experiment employed three sensors simultaneously in the highest sensor proximity configuration, where CS-3 contains inverted but still detectable MCL passage signal response. Taken together, these experiments indicate the achievable limit of spatial resolution ($\sim 40\ \mu\text{m}$) for this sensing scheme which essentially depends on the geometry and design of the sensor array regardless of the substrate material type.

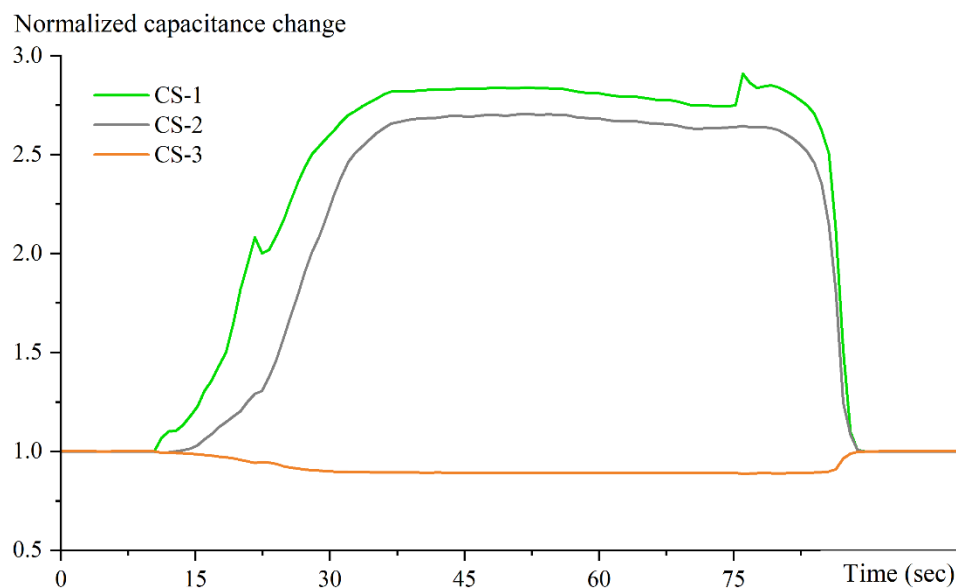


Figure 3-9: Normalized capacitance changes with time for advancing and receding deionized water droplets using three capacitance micro-sensors (CS-1, CS-2, and CS-3) in adjacent proximity with the microdevice based on a soda-lime glass substrate.

DSA provided controlled dosing of the water droplet throughout the experiments, where a short interval between successive dosing was maintained by pausing the droplet flow from the syringe to ensure a noticeable time lag among the sensors employed for tracking MCL. In contrast, during retraction, the suction of the water droplets through the syringe was uninterrupted and enabled a faster retracting motion of the MCL; consequently, retraction events happened faster than dosing events and thus demonstrated a smaller time lag. The experiments intended to allow a noticeable time lag among sensors to ensure individual functionality rather than an identical time lag for dosing and retraction. To have more insights into the reason behind signal inversion when neighboring sensors are used requires scrutinizing Figures 3-6 to 3-9 closely. Figure 3-6 shows that the capacitance sensing based on a doped silicon substrate exhibited signal inversion of at least one sensor when three or more (out of six total) capacitance sensors were employed to

track the MCL. According to the conceptual schematic of electrical field distribution shown in Figure 3-10, the electric field lines resulting from two adjacent IDE-based capacitance sensors interfere with each other. This interference or coupling effect among capacitance sensors placed adjacent to each other facilitates a variability in the electric field that drops the overall capacitance of the region. Therefore, electric field interference often led to signal inversion when neighboring sensors were used, especially for microdevices based on the doped silicon substrates. Later, an electrically insulating and lower dielectric constant substrate was adopted to overcome interference in capacitive signal outputs. Apart from lower dielectric constant, availability in conventional substrate form and cost-effectiveness made soda-lime glass an ideal candidate as the starting base of the microdevice. As shown in Figure 3-7, the implementation of the soda-lime glass substrate abated the signal inversion caused by proximity effects.

During the experiments, it was observed that the outermost sensors, CS-1 and CS-6, provided a signal with a higher amplitude. These external sensors, surrounded by another sensor on a single side, experienced less interference or coupling than the interior sensors. In contrast, the internal sensors, such as CS-3 (surrounded by other sensors on both sides), provided lower amplitudes due to interference from both sides.

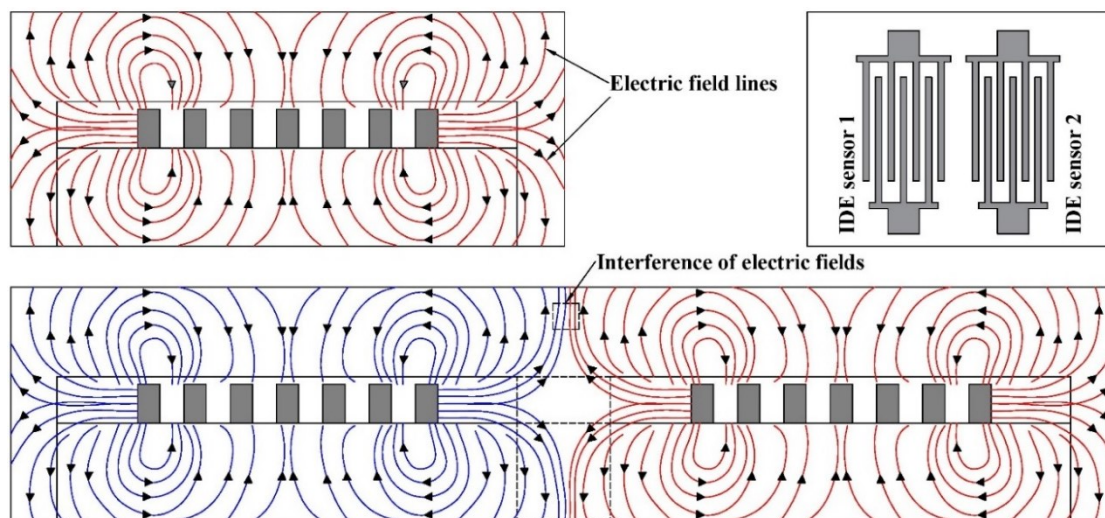


Figure 3-10: Schematic of electric field lines distribution when a capacitance sensor is operating on its own (top) and when two IDE-based capacitance sensors are placed adjacent (bottom).

The capacitance-sensing microdevice also enabled location and speed tracking of MCL at elevated temperatures and in a dynamic heat transfer process of droplets evaporating from a heated surface. As described above, a thin-film resistance heater was integrated with the microdevice, which facilitated heating of the topmost surface at various controllable temperatures for droplet evaporation investigation. Figures 3-11, 3-12, and 3-13 show the normalized change in the capacitance signal of six capacitance sensors during the evaporation cycle of a 1 μL water droplet at surface temperatures of 57.2 $^{\circ}\text{C}$, 70.7 $^{\circ}\text{C}$, and 85.5 $^{\circ}\text{C}$. These results indicate that, as expected, the duration of the evaporation event gets shorter as the surface temperature increases. According to the capacitance sensing perspective, the passage of the MCL due to the evaporation process occurred after 150 seconds at 57.2 $^{\circ}\text{C}$, 106 seconds at 70.7 $^{\circ}\text{C}$, and only 79 seconds when the surface temperature was at 85.5 $^{\circ}\text{C}$. The DSA provided controlled dosing of the water droplet during experiments and captured images of the entire evaporation process during

each of the experiments as shown in Figure 3-4. During droplet evaporation studies, MCL's speed associated with the dosing was much lower than the speed of MCL due to the evaporation at the near end of the experiment. Therefore, the MCL took a shorter time to move away from the sensor region, consequently demonstrating a shorter time lag during retraction.

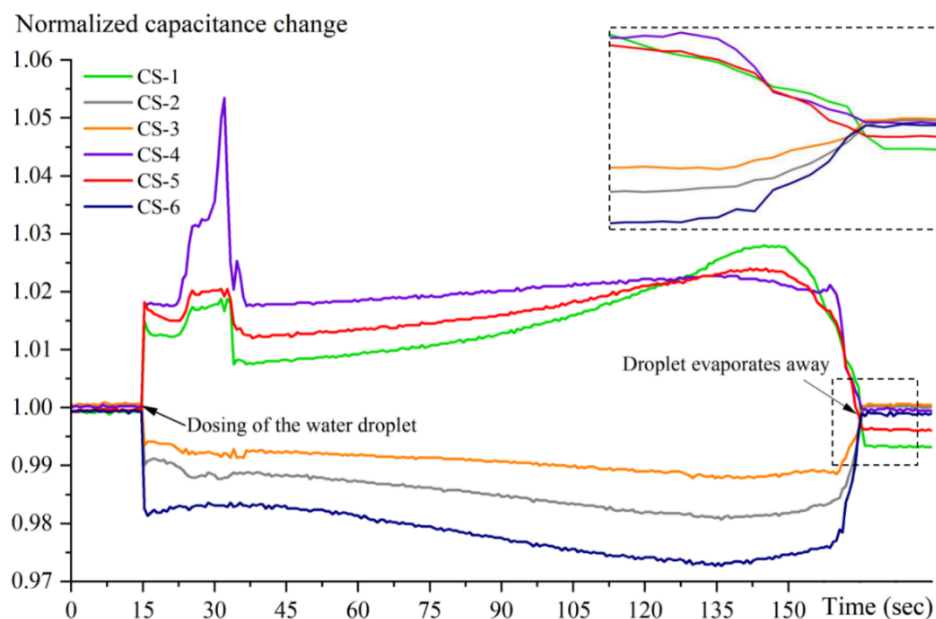


Figure 3-11: Normalized capacitance changes with time for droplet evaporation on a heated polyimide surface at 57.2 °C using all six capacitance micro-sensors (CS-1 to CS-6). The dashed box on the top right shows a close-up of the time lag among the sensors as the droplet evaporates away from the sensor region.

The observed capacitance changes in the sensor array are in good qualitative agreement with the captured images of droplet evaporation shown in Figure 3-4. As shown in Figure 3-4, during the evaporation at 57.2 °C and 85.5 °C, the MCL of the water droplet moved away from the rightmost capacitance sensor (CS-6) to the leftmost one (CS-1). The normalized changes in capacitance signal shown in Figures 3-11 and 3-13 exhibit the same sequence and time lag among each of the six sensors employed during the experiments.

These results indicate the efficient functionality of this micro-device at elevated temperatures and during dynamic heat transfer processes.

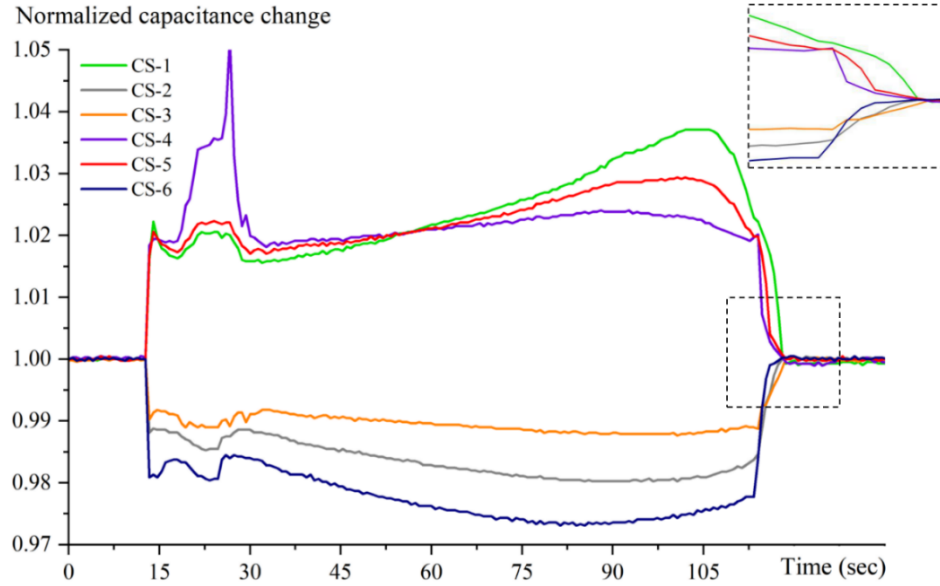


Figure 3-12: Normalized capacitance changes with time for droplet evaporation on a heated polyimide surface at 70.7 °C using six capacitance micro-sensors (CS-1 to CS-6). The dashed box on the top right shows the time lag among the sensors as the droplet evaporates away from the sensor region.

Previous studies have provided valuable insights regarding the experimental investigation of droplet evaporation under external electric fields [45]–[47]. These works adopted parallel plate/disc capacitors to apply an external electric field to the droplet under study. High voltage power converters were employed to generate the high voltage between the capacitor plates such that the applied electric fields were in kV/cm ranges. For noticing detectable changes in water droplet geometry such as contact angle, baseline, and surface area, the strength of the electric fields has to be quite strong, often in the several kV/cm range. In contrast, in this work each IDE-based capacitance sensor is connected to a function generator that provides a sinusoidal signal with a frequency of 200 kHz and

amplitude of 7.07 Vrms. Even considering the microscale dimensions of the microdevice, this study estimates a maximum possible field strength in the sensing region of less than 0.5 kV/cm, which is significantly smaller than field strength values in the literature [45]–[47]. Further, this study has not observed any effects or changes in the geometry of the dosed water droplets during the experiments with the IDEs powered vs. not powered. For these reasons, this study concludes that the applied voltage in this work was not strong enough to impose any impact on the droplet under study.

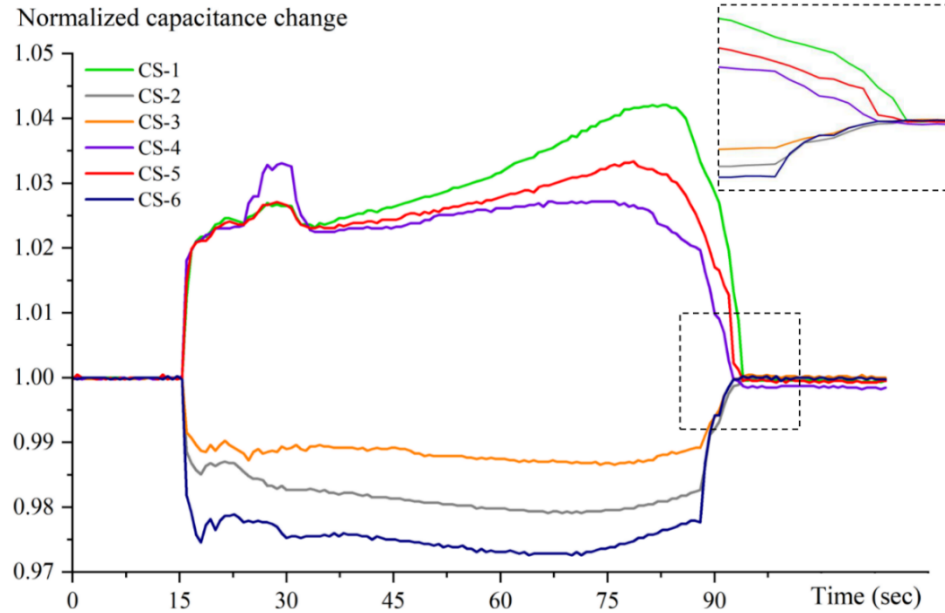


Figure 3-13: Normalized capacitance changes with time for droplet evaporation on a heated polyimide surface at 85.5 °C using six capacitance micro-sensors (CS-1 to CS-6). The dashed box on the top right shows the time lag among the sensors as the droplet evaporates away from the sensor region.

3.4 Summary of Findings

This study compared the performance of capacitive sensing microdevices and their dependence on substrate type. The sensing scheme utilized in this work has allowed for a

highly sensitive and bulk-fabrication-compatible means of MCL sensing, which enables precise tracking of moving phase interfaces for unconstrained liquid droplets with both advancing and receding movement. Although the previous approach of implementing multiple capacitive sensors in adjacent proximity for the semiconducting base has demonstrated a few limitations including coupling effects, it did not prevent the effective detection of MCL. Utilization of a dielectric substrate has demonstrated notable improvements, including but not limited to increased capacitance signal outputs and reduced coupling effects for multiple sensors in adjacent proximity. Moreover, this sensing scheme has demonstrated the efficient tracking of MCL during droplet evaporation at three different surface temperatures, which establishes its functionality at elevated temperatures and during a dynamic heat transfer process in the form of an evaporating water droplet.

In the future, the improvement of this capacitance sensing microdevice should primarily focus on further reducing the proximity effect by enhanced filtering and minimizing parasitic capacitance in leads, traces, interconnects, other system elements. Another emphasis in device improvement should be increasing the spatial resolution, via more compact geometry for the IDEs. This in turn, however, will require enhanced sensing of small capacitance changes and potentially more complicated micro/nanofabrication. For exploring new applications, this sensing scheme can be employed in complex phase-change heat transfer phenomena such as nucleate boiling processes and thin film evaporation. This sensing scheme may also have applications beyond thermal management, such as water harvesting, pollutant detection, or immiscible liquid/liquid interface studies.

CHAPTER 4

INDEPENDENT MICROSCALE SENSING OF PHASE INTERFACE AND SURFACE TEMPERATURE DURING DROPLET EVAPORATION

4.1 Introduction and Motivation

Evaporation is a common natural phenomenon that occurs in various aspects of our everyday lives and has significant scientific and engineering applications. The study of heat transfer mechanisms and MCL behavior involved in the evaporation of sessile droplets has been a matter of great interest in recent years due to its applicability in diverse fields, including medical diagnostics, inkjet printing, DNA mapping, and multiphase thermal management techniques. [1], [10], [11], [34], [48], [49]. In terms of phase change cooling, droplet evaporation facilitates high heat fluxes due to the significant amount of thermal energy associated with the latent heat of vaporization of the fluid which reduces the thermal resistance between the heat source and sink [1], [6].

Droplet evaporation involves complex thermo-fluid phenomena, including but not limited to conjugate heat transfer at the MCL region, the motion of the MCL, micro-convection within the sessile droplet, and surface evaporation [10], [11] [1]. Indeed, the MCL - a three-phase region where the liquid-vapor interface meets the solid surface - is an area of strong thermal and mass gradients that greatly influences the overall evaporation process. Different physical mechanisms govern the overall dynamics of the evaporation process depending on the experimental environment. When evaporation occurs in an open

environment, the diffusive transport of vapor into the atmosphere, the phase transition that occurs at the surface of the droplet, the heat transport within the droplet, and the conduction of heat from the surface to the droplet are among the significant influencing physical processes [50]. Despite being a topic of extensive research, the interdependence of MCL behavior and the associated conjugate heat transfer still needs to be comprehensively understood during droplet evaporation [11], [51].

The MCL of a droplet may look like a sharp interface at the macroscale, but at the microscale, it consists of a combination of a macro-region and a thin-film micro-region. As Figure 4-1 shows, the micro thin-film region comprises an adsorbed film and a transition film, where the adsorbed film results from the strong adhesion interactions between the droplet and the substrate. While the suppression of evaporation in the adsorbed film region is well-established for a liquid droplet in contact with pure vapor, the behavior of the adsorbed film region becomes more complicated in the diffusion-limited evaporation regime such as when the environment is not pure vapor. In this regime, the evaporation rate is limited by the rate at which the vapor molecules can diffuse away from the surface of the liquid into the atmosphere. The disjoining pressure, resulting from the change in relative vapor pressure in the atmosphere, determines the thickness of the adsorbed film region [50], [52]–[55]. The neighboring region of the adsorbed film where the thickness increases is known as the transition film region. This region is home to intense evaporation and very high heat flux values as the liquid-solid adhesion forces are weaker compared to the thin-film region. The transition film thickness varies from 1 to 3 μm [56], much thicker than the adsorbed film but still thin enough to offer only a negligible resistance to heat transfer. The thermal resistance increases with the film thickness in the macro-region

consisting of the intrinsic meniscus and micro-convection region. As the increasing film thickness offers growing resistance to the overall heat transfer, both these regions experience lower heat flux values compared to the transition film region. The macro-region holds the droplet's bulk portion and acts as the resource that supplies fluid toward the strongly evaporating micro thin-film regions. The liquid-vapor interface generated from the beginning of the intrinsic meniscus region is what is generally known as the droplet's macroscopic contact angle relative to the substrate's solid surface [3], [11], [57]. From heat transfer perspectives, researchers have emphasized the importance of the MCL in general and the micro-region that contains the transition thin film, as this region possesses the most significant heat transfer characteristics [14], [15].

Despite this established viewpoint, unlocking the physical interdependence of the MCL region and local temperature distribution remains a critical need in order to validate models, enable *a priori* surface design, and optimize evaporative cooling processes [15], [36]. Numerous approaches in the literature have adopted analytical models that conclude that the transition film between the intrinsic meniscus and non-evaporating adsorbed film regions facilitates the highest evaporative heat fluxes [1], [10], [11], [34]–[36], [58]–[60]. A few experimentally validated numerical studies on evaporating films from micro-grooves have demonstrated that up to 80% of the total dissipated heat during droplet evaporation occurs at the transition thin-film region [14], [60].

The behavior of the MCL is the primary factor that influences the evaporation process of a sessile droplet, and various research works have investigated the substrate's surface properties that significantly affect the MCL behavior and wettability. As an example, in one such work, Sobac and Brutin [61] studied the spontaneous natural

evaporation of sessile droplets under atmospheric conditions from nanocoated surfaces of varying wettability with different working fluids. The investigation revealed that the dynamics of the evaporative rate are proportional to the dynamics of the wetting radius, and the greater the contact angle and the more pinned the contact line the shorter the duration of the evaporation process [61]. The heat transfer characteristics at the MCL regions have also been experimentally investigated, although the number of works is relatively limited [14], [15], [36] [35], [37], [58], [62]. According to one empirical investigation with hydrofluoroether engineered fluid (HFE), the local heat fluxes at the contact line region could be 5.4-6.5 times greater than the average heat flux at other regions of the evaporating droplet [36]. Experiments with other nonaqueous liquids such as heptane have demonstrated that a 50 μm sub-region between the intrinsic meniscus and adsorbed film region facilitates 45-70% of the total heat transfer throughout the evaporation process [14], [15]. Additional experimental investigations with HFE for bidirectional movements of its MCL observed higher heat fluxes at the three-phase contact line region for advancing movement compared to the receding motion of the moving interface [36], [37]. The advancing MCL causes a significant increase in the temperature change rate per unit length by deforming the thermal boundary layer between the fluid and heated wall, which in turn enables a high heat transfer rate [62]. These experimental approaches have also demonstrated that during the advancing movement of MCL, the evaporative heat fluxes near the moving three-phase interface increase with the increasing speed of the MCL. Interestingly, in contrast the highest heat fluxes near this region during receding movement are independent of the speed of the MCL [36], [37]. Clearly, the MCL speed and direction are important factors in controlling the rate of heat transfer in this critical region.

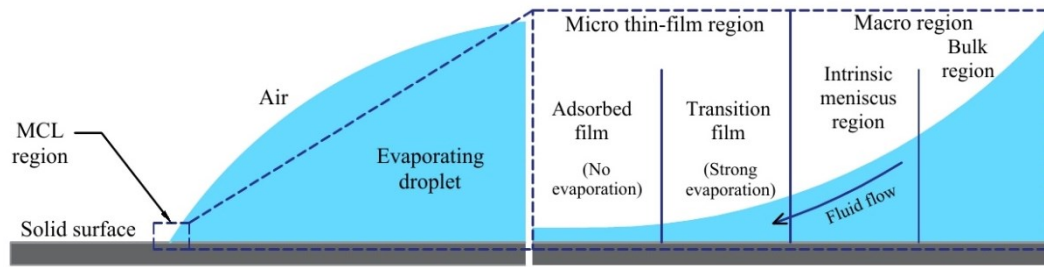


Figure 4-1: Schematic of the contact line region of a hydrophilic evaporating droplet on a solid surface.

Due to the involvement of complex heat transfer and phase interface dynamics during droplet evaporation, it is challenging to measure the local temperature distribution and correlate it with the MCL behavior. This often requires composite sensing schemes that combine non-intrusive microscale and transient measurement techniques [14]. Experimental approaches within the literature like those cited above have adopted macroscopic thermocouple probes, which present significant constraints in terms of temperature resolution, response time, and potential invasiveness to the droplet under study [1][13]. To overcome low spatial resolution with macroscopic sensing techniques, some researchers have utilized thermochromic liquid crystals (TCLs), organic compounds with an optically active twisted molecular structure that changes color with temperature change within a specific range. Researchers studied the evaporation of volatile liquid droplets deposited on a heated substrate in a pure saturated vapor environment via TCLs, where the TCLs reflected a distinct color depending on the temperature, and a charge-coupled device (CCD) camera captured the color information for image processing to convert it into temperature readings [63]. Despite being advantageous over macroscopic probe techniques, measurement uncertainty and low shelf-life of the crystals limit TCLs' broader applicability [1][14], [15].

Higher spatial resolution than thermocouples, good temperature sensitivity, and non-contact nature have made infrared (IR) thermography one of the most widely used techniques for measuring local temperature distribution. Although IR thermography is a well-established technique, it can only be employed to measure temperature distribution if optical access to the surface is available in the wavelengths of interest [64]. Moreover, the limitation on the camera resolution and wavelength diffraction limit often restrains IR thermography from precise quantitative detection of the temperature distribution at the thin-film region [1], [14], [15]. Microfabricated temperature sensors are attractive for microscale temperature sensing of evaporating droplets because of their high temporal and spatial resolution [65] so long as they are implemented in a non-intrusive manner to the droplet under study. A few fundamental works exploring local processes in pool boiling have developed specialized micro-thermocouples as these are smaller and faster, whereas the macroscopic temperature probes lack sufficient accuracy regarding spatial and temporal dimensions. Measurements of local heat transfer mechanisms in dynamic heat transfer processes require thermal sensors with sufficient fast response; these microfabricated thermocouples facilitated the effective investigation of local temperature fluctuations and spatial wetting dynamics for phase change heat transfer processes [7], [66], [67]. Similarly, several significant experimental investigations of heat transfer distributions at the interface between a solid substrate and fluid have employed microscale resistance heater arrays on a quartz substrate. These approaches incorporated infrared cameras with high-speed CCD imaging and revealed the significance of specific heat transfer mechanisms in addition to microlayer evaporation for boiling processes [8], [68]–[70]. An experimental investigation measuring interfacial temperature distribution during

droplet evaporation of ethanol on a copper substrate also coupled infrared thermography with a CCD camera [71]. Another experimental approach with a novel technique of measuring heat transfer parameters utilized infrared thermometry to investigate wall temperature and heat flux distribution during droplet evaporation of PF-5060. According to this work, as the droplet diameter decreased due to evaporation the highest heat flux values occurred at the receding moving contact line of the droplet [64]. Other fundamental works on the experimental investigation of phase change heat transfer have developed and implemented novel test rigs for inspecting boiling heat transfer from a hot plate to planar and impinging jets. These works employed a micro-optical technique with a probe diameter of approximately $1.5\text{ }\mu\text{m}$ for efficient tracking of droplet diameter or dry spot size of microscale droplets or bubbles [72], [73]. Researchers have investigated several nucleate boiling experiments under steady-state and transient conditions for different wetting fluids such as FC-72, isopropanol, and water employing these micro-optical probes [74].

However, measuring surface temperature distribution employing all these methods alone does not necessarily provide the strong, direct experimental link to microscale MCL dynamics needed to advance the field and overcome its commonly invoked assumptions regarding interdependence. Besides temperature, a comprehensive understanding of the physical mechanisms involved in droplet evaporation requires correlation of MCL location and speed with the local temperature distribution. Several seminal works within the literature emphasized photographic inspections of droplet structures during the evaporation process and implemented very complex techniques due to continuous capturing schemes still underdoing development during that period. The implementation of the flash photographic method provided significant insights for various phase change heat transfer

processes, including but not limited to Leidenfrost evaporation, collision dynamics of a liquid droplet on a hot surface, and nucleate boiling [75]–[77]. Photographic inspection also played a decisive role in the fundamental work on the investigation of contact angle temperature dependence of water droplets as the contact angle measurements were obtained from the captured photographs of the droplets [78]. High-speed photographic techniques and heat transfer measurements played equally significant roles in another pivotal work investigating the effects of surface roughness on water droplet evaporation [79]. Recent experimental approaches within the literature have employed high-speed cameras and optical image processing techniques to document MCL movement during evaporation of small-scale droplets but are limited due to their macroscopic spatial resolution and visibility, i.e. line of sight and viewing angle [16]–[19]. As an alternative, electrical sensing approaches facilitate several advantages over optical sensing, including real-time tracking of MCL location at the microscale without requiring line-of-sight visibility or set viewing angles [16], [18],[41].

This work adopted a novel combined microscale sensing approach to experimentally reveal the physical interdependence of MCL motion and local temperature distribution underneath an evaporating droplet. The experiments reported in this work utilized a custom-designed micro-electromechanical (MEMS) device comprised of spatially distributed thin-film resistance temperature detectors (RTDs) and an array of interdigitated electrode (IDE) capacitance-based phase interface sensors for investigating the heat transfer phenomena and MCL motion for evaporating droplets on the microscale. This novel approach of combining a capacitance-based phase interface sensing scheme with temperature-sensing microfabricated RTDs allows for simultaneous and independent

sensing of both critical aspects with high spatial and temporal resolution. Results of this work show that the passage of the MCL precedes the actual change in local surface temperature and the duration of time lag between these two events depends on the speed of the MCL. In addition, it is shown that the MCL speed depends on the surface temperature. Specifically, higher surface temperature facilitates higher MCL speed, which in turn causes greater differences in wall temperature underneath the liquid bulk and dry region, consequently enabling higher heat flux values. Further, most of the temperature change during the evaporation process occurs in the three-phase contact line region, accounting for more than 70% of the overall temperature change.

4.2 Methodology

4.2.1 Microdevice Overview

This work has adopted a custom-made composite MEMS device comprised of a thin-film resistance heater, a series of RTDs, and an array of IDE capacitance microsensors to investigate the droplet evaporation process. Figure 4-2(a)-(c) show laser microscope images of the micro-device used for studying droplet evaporation. Figure 4-2(d) shows a diagram of the cross-sectional view of the micro-device, where the resistance heater resides directly on top of the starting soda-lime substrate. The first of the three polyimide polymer layers resides between the resistance heater and the RTDs to provide electrical insulation. A series of 28 platinum thin-film RTDs are spatially oriented from the center of the device atop the first polymer layer to measure the local temperature distribution beneath the evaporating droplets at various locations. For both the RTDs and IDEs, this study follows a numbering scheme where 1 corresponds to a sensor closest to the center and numbering increases with radial distance towards the periphery of the sensing zone.

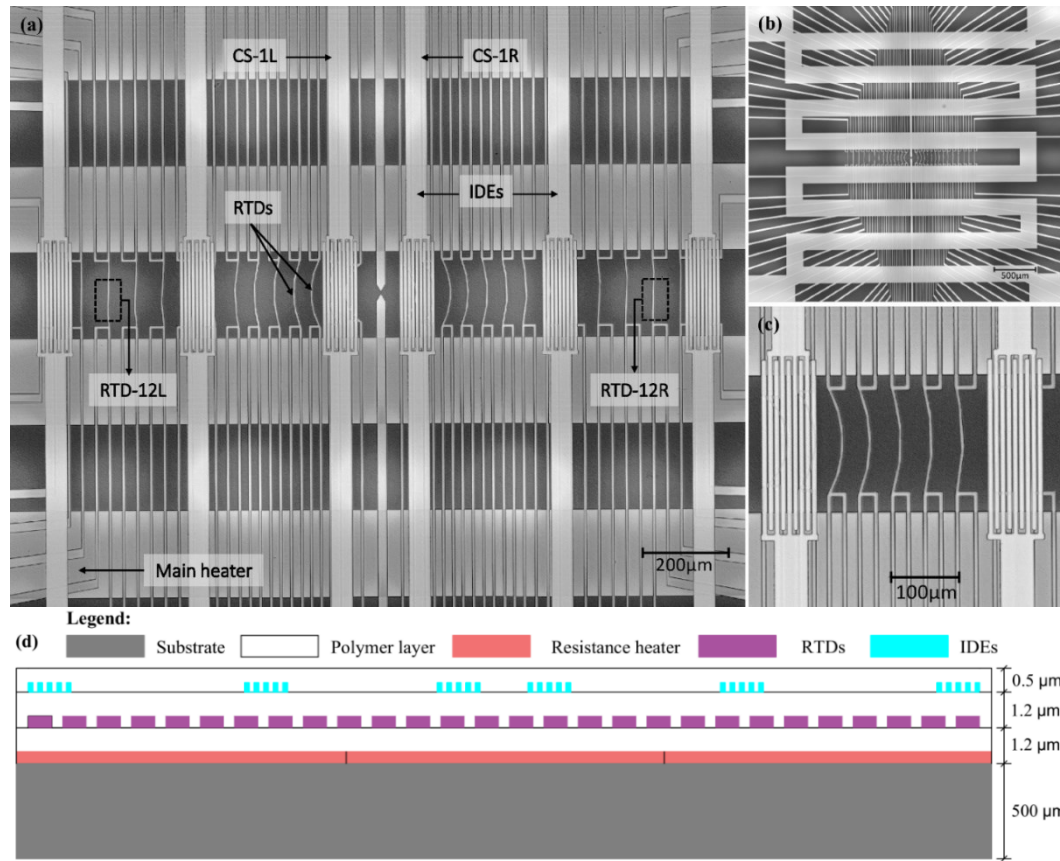


Figure 4-2: Laser microscope images of the micro-device. (a) A detail of the sensing zone containing six IDE capacitance micro-sensors, a series of four-probe type RTDs, and a resistance heater. (b) Thin-film resistance heater (serpentine feature) located beneath RTD and IDE layers. (c) A close-up of the sensing region showing detailed view of the IDEs and RTDs. (d) Schematic diagram of the cross-section of the micro-device. Conceptual image, not to scale.

Naming is further accomplished with an L for a sensor to the left of the device center and R for a sensor to the right. Hence, RTD-1R is the RTD closest to the device center on the right while RTD-14L would be the farthest RTD to the left of the device center. A similar scheme is used for the capacitance sensors, i.e., CS-1R, CS-3L, etc. It is important to note that despite centering the droplet on the device at the start of an experiment, evaporation does not necessarily occur symmetrically or end exactly at the device center.

An RTD works based on the operating principle that the electrical resistance of metals having a positive temperature coefficient of electrical resistance changes linearly with temperature. Since the temperature sensing depends on the element resistance, any added resistance from the lead wires, contacts, or connectors will result in measurement error for an RTD [80], [81]. As shown in Figure 4-2(c), a four-probe style of RTD was utilized in this project that eliminates the influence of contact and lead resistances and allows the resistance of the actual temperature-sensing central four-probe region of each RTD to be accurately known. The spatial resolution of the temperature sensing scheme employed in this work is 40 μm as dictated by the spatial separation between each consecutive RTDs.

The IDEs of the capacitance microsensor were deposited atop the second polymer layer to track the speed and location of MCL of the evaporating droplets. In prior works, the IDE-based sensing scheme demonstrated effectiveness for microscale tracking of the MCL for advancing and receding aspirated water droplets as well as during droplet evaporation processes [18], [82]. The capacitance micro-sensor works based on the operating principle that the relative permittivity of the region above the interdigitated electrodes changes with the passage of the MCL of the droplet, which in turn causes a detectable change in capacitance in the sensor array [16], [18], [19], [82]. This device employed a thin (500 nm) insulating layer of polyimide directly atop the microfabricated IDEs, which possesses relative permittivity ϵ_r of 3.4 [83]. With the dosing of the water ($\epsilon_r = 80$) [19] droplet, the capacitance micro-sensors experience a significant change in relative permittivity in the sensed region compared to when mostly air ($\epsilon_r = 1$) [18] occupies the area directly on top of the IDEs. The IDE array represents this change in

relative permittivity by exhibiting a change in capacitance signal output, which denotes the location and passage of the MCL during the experiment. Please refer to the previous works [18], [82] for further details on this sensing scheme, including its implementation and validation.

4.2.2 Microfabrication Process

A soda-lime glass wafer with a thickness of 500 μm was selected as the starting substrate due to its cost-effectiveness, microfabrication compatibility, and ability to enhance the strength of the capacitance signals while minimizing coupling effects for multiple capacitance sensors in adjacent proximity. The microfabrication of the MEMS device consists of the deposition of platinum (Pt) as the resistance heater, RTDs, and capacitance micro-sensor array by standard photolithography and lift-off techniques. The microfabrication process also includes the spin coating of the thin insulating polyimide polymer layers to provide electrical insulation between metal layers and to enable a thin topmost protective coating. To begin, a 100 nm thin film of Pt was patterned as the serpentine resistance heater directly on top of the starting substrate (Figure 4-2(b)), where a 15 nm thin film of titanium (Ti) acted as the adhesive layer. The deposition of the Pt layer was carried out in an AJA ATC sputtering system with a commercially available 3-inch sputtering target, which provided a deposition rate of 75-100 nm/min at 200 W. The same sputtering deposition process was implemented to deposit all three metal layers (resistance heater, RTDs, and IDEs) of the microdevice.

A commercially obtained spin-on polyimide (PI-2611, HD Microsystems) was utilized to deposit the thin insulating layers. The stock PI-2611 polymer provided a comparatively thick layer of 2.8 μm at a spin speed of 5000 RPM. Adding N-Methyl-2-

Pyrrolidone (NMP) with PI-2611 provides thinner layers at the same spin speed. A diluted PI-2611 (75% PI-266 + 25% NMP) provided a thin film of 1.2 μm atop the resistance heater, which acted as the electrically insulating layer between the resistance heater and the RTDs. Next, the array of 28 RTDs was patterned on top of the initial polyimide insulation layer. A second 1.2 μm polyimide film was then deposited via spin coating to serve as the electrical insulation between RTDs and the capacitance-sensing IDE micro-sensors to follow. The IDEs utilize a 70 nm thin layer of Pt deposited on top of the second insulation layer of polyimide and are shown in Figure 4-2(a). Finally, a thin layer (~ 500 nm) of polyimide was deposited on top of the IDEs to create a topmost protective coating of the micro-device and prevent shorting when a water droplet is present. Bond pads for every sensor on each deposited metal layer were located at the chip periphery on the starting substrate for convenient and reliable wire bonding. The three polyimide layers were patterned via reactive ion etching with a mixture of 5 sccm CF_4 and 20 sccm of O_2 to remove unwanted polymer from the device periphery before depositing the bond pads onto the exposed soda-lime surface.

4.2.3 Experimental Setup

Figure 4-3 demonstrates the experimental setup for studying the droplet evaporation process and the micro-device to be tested. The bond pads of the microfabricated test device were individually wire-bonded with bond pads of a commercially obtained leaded ceramic chip carrier (Spectrum Semiconductor Materials Inc.). The test device and ceramic chip carrier assembly was connected with a pin grid array (PGA) zero insertion force socket, which was in turn embedded onto a custom sample stage. This assembly was aligned underneath the syringe of a computer-controlled drop

shape analyzer (DSA 25E, KRÜSS Scientific) for the evaporating droplet studies as illustrated in Figure 4-3. During experiments, the dosed volume of the water droplets was 6.0 μL with a dosing rate of 1.0 $\mu\text{L/s}$. The initial temperature of the droplet was 24.0 $^{\circ}\text{C}$.

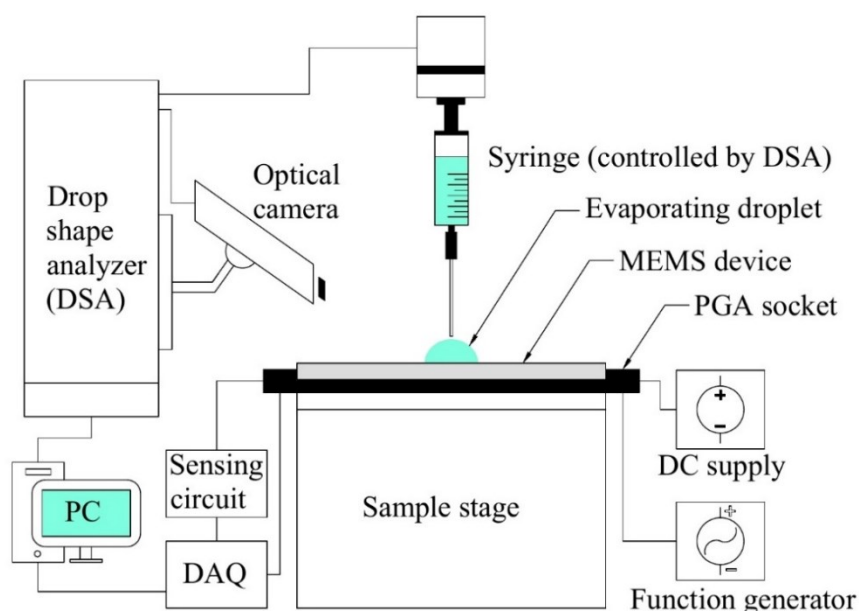


Figure 4-3: Schematic of the experimental setup. Conceptual image, not to scale.

The DSA dosed the consistent volume of droplets during each experiment, and an optical camera attached to the DSA recorded the evaporation process. The images and videos captured by the DSA during the evaporation process like those shown in Figure 4-4 enabled the validation of the intended functionality of the micro-device. A DC power supply provided the necessary power to the resistance heater to control the droplet's evaporation by facilitating elevated surface temperatures during the experiment. As Figure 4-4 depicts, the DSA facilitated precise dosing of a water droplet through a needle with a diameter of 0.50 mm in the approximate center of the microdevice. The droplet entirely covered the sensing zone of the microdevice, which allowed for simultaneous measurement of temperature distribution and the tracking of the MCL's speed and location. The collage

images presented in Figure 4-4 illustrate the changes in volume and contact angle of the droplet due to evaporation from the heated polyimide surface of the microdevice. The DSA recorded the changes in volume, diameter, and contact angle as the evaporation progressed for all the experiments conducted in this study. Further details regarding DSA-tracked contact angle and droplet volume data can be found in the Results and Discussion section. To prevent self-heating of the RTDs, a small current of 0.2 mA was supplied from a separate DC supply to the power leads of each RTD employed during the experiment. The voltage leads of each RTD, and capacitance micro-sensor were connected to a computer-controlled multichannel data acquisition (DAQ) system (NI 6255, NI).

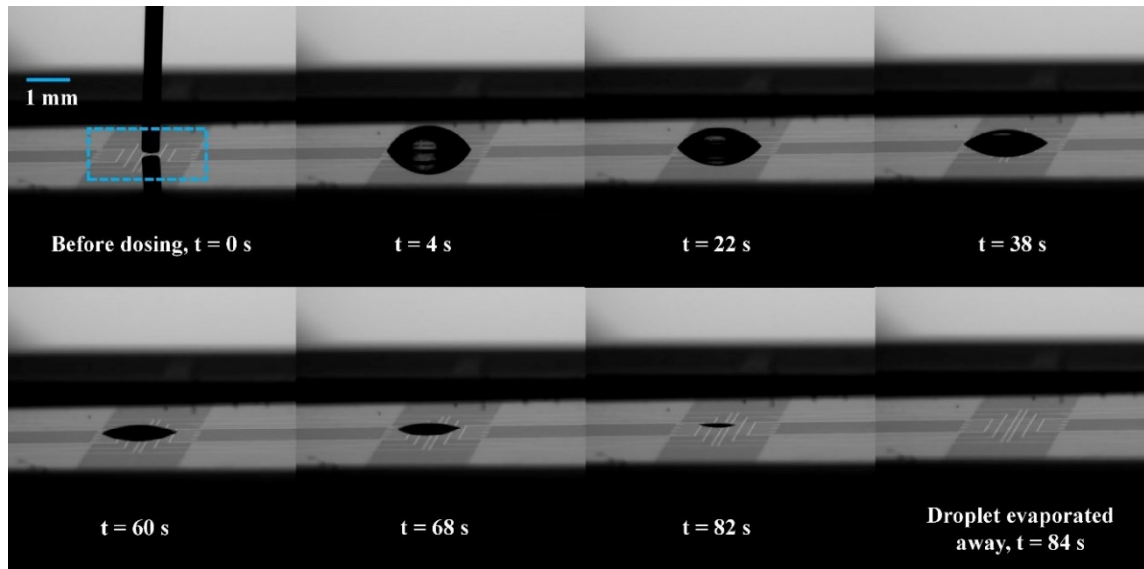


Figure 4-4: Representative optical image composite from the DSA for an evaporating droplet during an experiment. The dashed box at the top left of the collaged image highlights the sensing zone of the micro-device.

4.2.4 Surface Temperature Calibration

An IR camera (FLIR A300) and a commercially available macroscopic thermocouple were employed to calibrate the surface temperature at various power inputs from the DC supply. During the calibration, the macroscopic thermocouple was carefully

placed on the microdevice's sensing zone, and good thermal contact was ensured between the polyimide coating of the device and the thermocouple's sensing tip. The microdevice was kept in good focus from the IR camera to monitor the temperature change of the polyimide surface simultaneously with the thermocouple and the IR camera. Before the calibration, a standard temperature humidity meter (Fluke 971) was utilized to adjust the IR camera's emissivity parameters and the thermocouple's temperature reading. The calibration of the surface temperature was carried out in the temperature range from 35 °C to 80 °C. To determine the current input to the resistance heater, a known DC voltage was supplied through a commercial resistor with minimal resistance (10 Ω), and the corresponding voltage drop was measured.

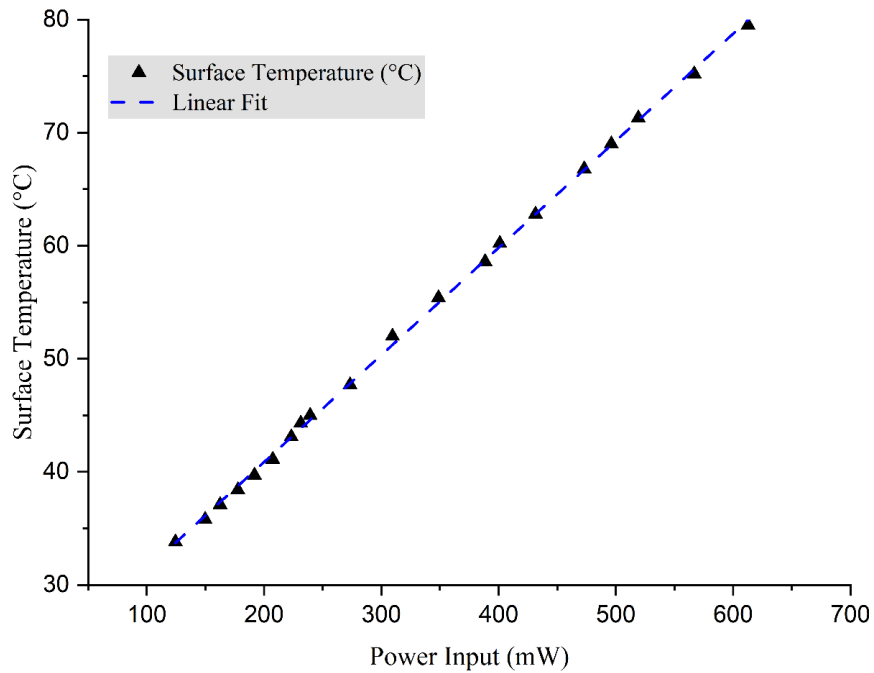


Figure 4-5: Measured surface temperatures at various power inputs during the calibration of the resistance heater.

The power inputs were calculated from the supplied DC voltage and the current input employed to the resistance heater. Both the thermocouple and IR camera provided

surface temperature readings of the polyimide top-layer of the microdevice for various power inputs ranging from 124.5 mW to 612.7 mW throughout the calibration. Figure 4-5 shows a linear increase in surface temperature as the power input increases.

4.2.5 Calibration of RTDs

Each of the twelve RTDs employed for the experiments exhibited a change in voltage outputs with the surface temperature change. Converting the recorded output voltages (Figure 4-6) into temperature readings for each RTD involved a few steps. Firstly, the output voltages of each RTD were converted into resistance values by employing the known current input of 0.2 mA.

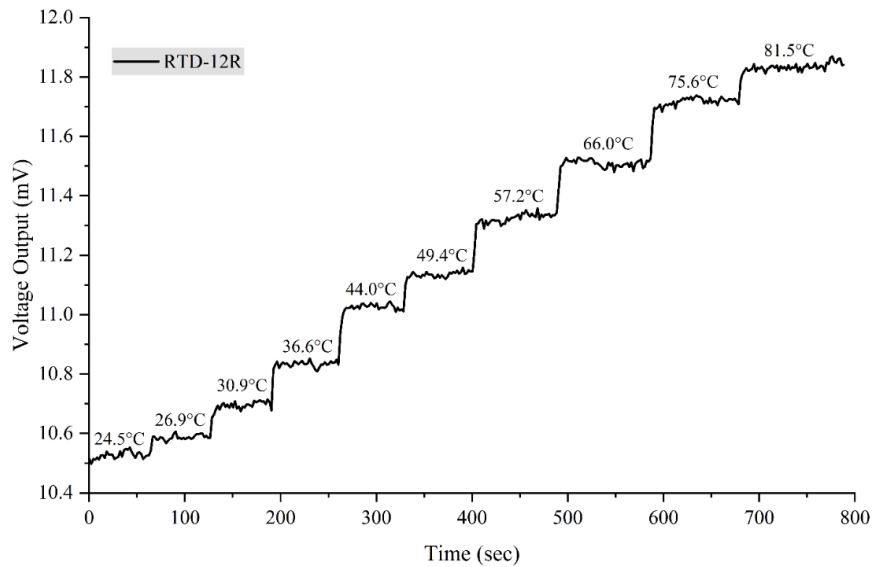


Figure 4-6: Measured voltage outputs at various temperatures during the calibration of the RTD.

Each temperature step from the resistance heater calibration and actual experiments provided an average resistance value for the RTDs, which yielded a linear regression relationship between temperature and resistance, as shown in Figure 4-7. This linear

regression relation provided temperature outputs corresponding to the resistance changes in the RTD arrays throughout the evaporation process.

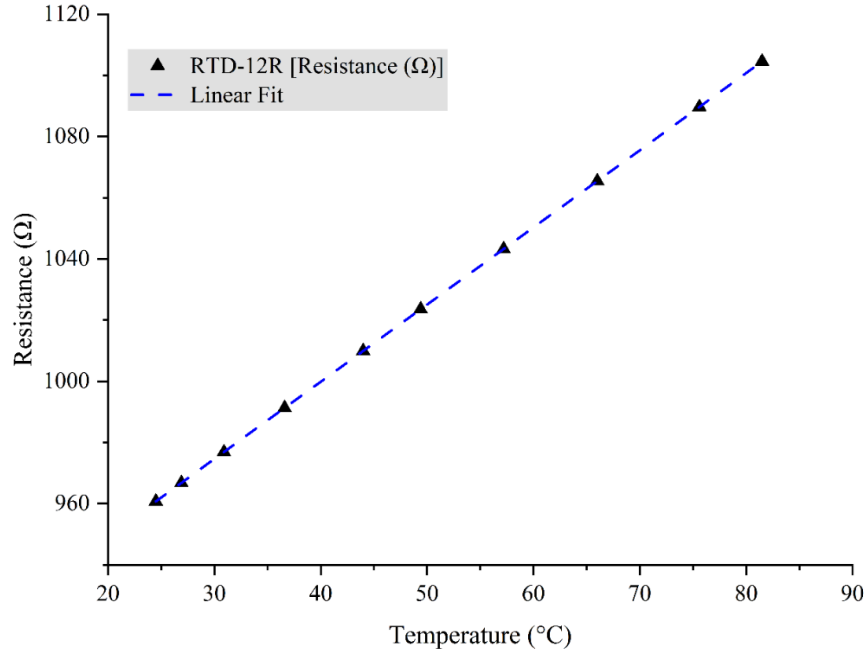


Figure 4-7: Change in resistance at various temperatures during the calibration of the RTD-12R.

4.2.6 Calculation of Temperature Difference Across Top Surface and RTDs Layer

Referring to the cross-section of the microdevice shown in Figure 4-2, the top surface of the microdevice and the RTDs are separated by a $1.7 \mu\text{m}$ of spin-on polyimide polymer. According to Fourier's law, the following expression yields the conductive heat transfer if T_S and T_R denote the surface temperature and temperature of the RTD sensor at its respective layer.

$$Q = kA \frac{dT}{dx} = kA \frac{(T_R - T_S)}{dx} \quad \text{Eq. 4-1}$$

$$dT = (T_R - T_S) = \frac{Qdx}{kA} \quad \text{Eq. 4-2}$$

where Q is the amount of power input to the resistance heater, A is the area perpendicular to the conduction, k is the thermal conductivity of polyimide, dx is the thickness of the polyimide, and dT/dx is the temperature gradient. According to the equation above, for various power inputs from 124.5 mW to 612.7 mW (shown in Figure 4-5), the temperature difference across the top surface and the RTDs' layer varies from 0.007 °C to 0.04 °C, which is much smaller than either the experimental uncertainty of the RTDs or the magnitude of the temperature changes being detected in these experiments. As such, this study presents the RTD-reported temperatures as being representative of the surface temperature within experimental uncertainty.

4.2.7 Measurement Uncertainty

The measurement uncertainty analysis of the temperature sensing was carried out by analyzing the standard deviation of the initially recorded temperature readings of each RTD when there was no heating, or no water droplet present in the sensor region of the microdevice. The uncertainty analysis of the three experiments performed at 53.0 °C, 61.0 °C, and 69.7 °C showed that the local temperature could be recorded with a precision of ± 0.2 °C. An absolute accuracy of ± 1.2 °C was determined by combining this random noise uncertainty with calibration against thermocouples or IR cameras which have their own limits of accuracy. It is important to note that most of this absolute uncertainty is expected to be bias error rather than random error such that measurements of temperature differences can still have smaller uncertainty estimated at ± 0.5 °C via standard error propagation methods. A sampling frequency of 30 Hz provided adequate datasets to precisely measure the dispersion of the recorded temperature readings and repeating each experiment three

times on each surface temperature enabled accurate estimation of the precision value stated above. A propagated error calculation from the lateral heat flux data presented in Figures 4-18(b) and 4-19(b) showed an error of 11%, resulting from the temperature difference measurement uncertainty of ± 0.5 °C. For propagated error calculations, the Kline-McClintock relation was utilized, which employs sensitivity indices and uncertainties in the measured variables to estimate resultant uncertainty.

4.3 Results and Discussion

This study utilized a drop shape analyzer (DSA) equipment to facilitate the dosing of a consistent volume of water droplets for each experiment reported in this work. Additionally, the DSA recorded the entire evaporation process. The DSA is state-of-the-art equipment capable of simultaneously measuring a droplet's change in volume and contact angle via its image analysis software. This measurement is possible when the droplet is in the good focus of the optical camera attached to the DSA and a measurement scale is set. As shown in Figure 4-4, the droplet remained in good focus throughout the evaporation process, and the DSA continuously recorded the changes in volume and contact angle. While Figure 4-4 shows imaging at a small angle ($<10^\circ$ from the horizontal) to enable viewing over the edge of the chip carrier, we have found no evidence that this small angle viewing impacts the software-measured values. Figure 4-8 depicts representative data on the variations in both volume and contact angle of a 6 μL water droplet on the polyimide surface.

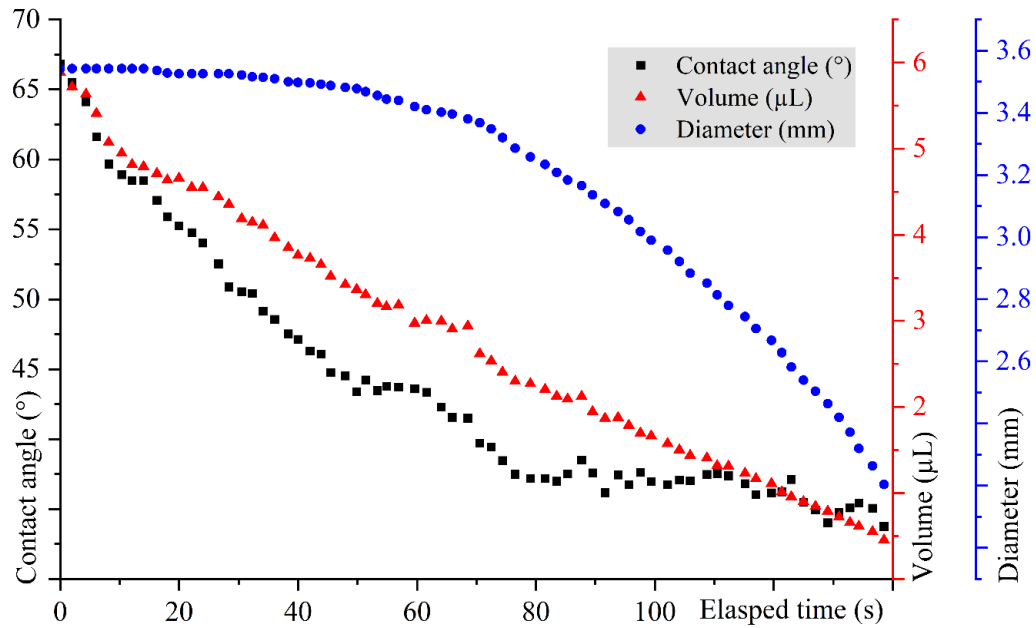


Figure 4-8: Measured surface temperatures at various power inputs during the calibration of the resistance heater.

Figure 4-9 demonstrates representative results of absolute capacitance change (%) resulting from the passage of the MCL and surface temperature response for the evaporation process of a 6 μL water droplet at a surface temperature of 69.7 $^{\circ}\text{C}$ from the initial dry state and through the subsequent droplet dosing and evaporation. As Figure 4-4 shows, the dosing of the water droplet on the heated polyimide surface of the microdevice was carried out via a needle attached to the syringe controlled by the DSA. Before dosing, the syringe's needle with a diameter of 0.50 mm was manually placed above the center of the microdevice. Water droplets of 6 μL in volume sufficiently covered the sensing zone of the microdevice, which was 1.5 mm in length from the leftmost to the rightmost RTD/IDE, and DSA provided controlled dosing of the same volume of water droplets for all experiments at varying surface temperatures. Since the dosing of water droplets did not facilitate precise alignment of the droplet's center with the microdevice's center or

corrections after dosing, the droplets in this experiment evaporated in an asymmetric manner with respect to the exact center of the microdevice, with the MCL crossing the sensing region from right to left with respect to Figure 4-2. It was observed that the droplets evaporated symmetrically with respect to their own center, however.

As Figure 4-9(a) shows, the six capacitance micro-sensors exhibited a simultaneous rise in capacitance signal with the dosing of the water droplet and retained it until the MCL passed through the sensor region near the end of the evaporation process. The capacitance-based micro-sensors also demonstrated sequential time lag between one another, which facilitated a precise tracking of the speed and location of MCL as the droplet evaporated. This is difficult to discern from the full time-scale data in Figure 4-9(a) but will be apparent in subsequent figures that focus on time windows specific to the MCL passage. Figure 4-9(b) shows the temperature values detected by the twelve functioning RTDs on the micro-device. At the beginning of the experiment, the RTD signals report room temperature until the DC supply powered the resistance heater of the micro-device to reach the desired surface temperature. With the dosing of the water droplet, the RTDs detected a sudden decrease in surface temperature and an eventual return to previous temperature readings as the droplet evaporated. The change in surface temperature throughout the evaporation process detected by the RTDs correlates in time to the changes in capacitance signals referring to the MCL passage, which validates the dual functionality of this micro-device. Additional figures (Figures 4-10 and 4-11) similarly portray the capacitance change and temperature with time over the entire experiment for an evaporating droplet of the same volume (6 μL) at surface temperatures of 61.0 $^{\circ}\text{C}$ and 53.0 $^{\circ}\text{C}$, respectively, where the overall evaporation process was completed over longer time periods compared to the

experiment conducted at the surface temperature of 69.7 °C. It is important to note that both the RTDs and IDEs were labeled according to a specific naming convention in the experiments reported on this work. This convention assigns a value of 1 to the sensor closest to the center, with subsequent sensors numbered in increasing order as their radial distance moves toward the periphery of the sensing zone. Additionally, this study utilized an "L" designation for sensors located to the left of the device center and an "R" designation for sensors situated to the right. As the annotated examples in Figure 4-2 depict, CS-1L represents the IDE nearest to the device center on the left side, while CS-3L indicates the IDE located furthest to the left from the device center. A similar naming scheme was employed for the RTDs, such as RTD-1R, RTD-13R, RTD-2L, RTD-14L, etc.

This study investigated the effect of large-scale convective flow or air currents on the RTDs or IDEs employed to measure the temperature distribution and track the MCL, as the experiments reported in this study took place in an open environment. As shown in Figure 4-9, the IDE signals did not depict any noticeable fluctuations above signal noise levels before the droplet dosing or after the evaporation cycle when the sensing region is bare to the open environment. Similarly, the measured temperature readings via the RTDs during these time periods also did not exhibit any fluctuations above signal noise levels that abrupt air currents would be expected to cause. For both sensor types, signal changes caused by the evaporation process were significantly larger than noise levels prior to and after droplet presence, indicating that the effect of air currents or large-scale convective flow were negligible in comparison. Additionally, attempts to measure air current movement near the experimental setup with an anemometer produced no readings, as any movement was below the instrument's lower threshold.

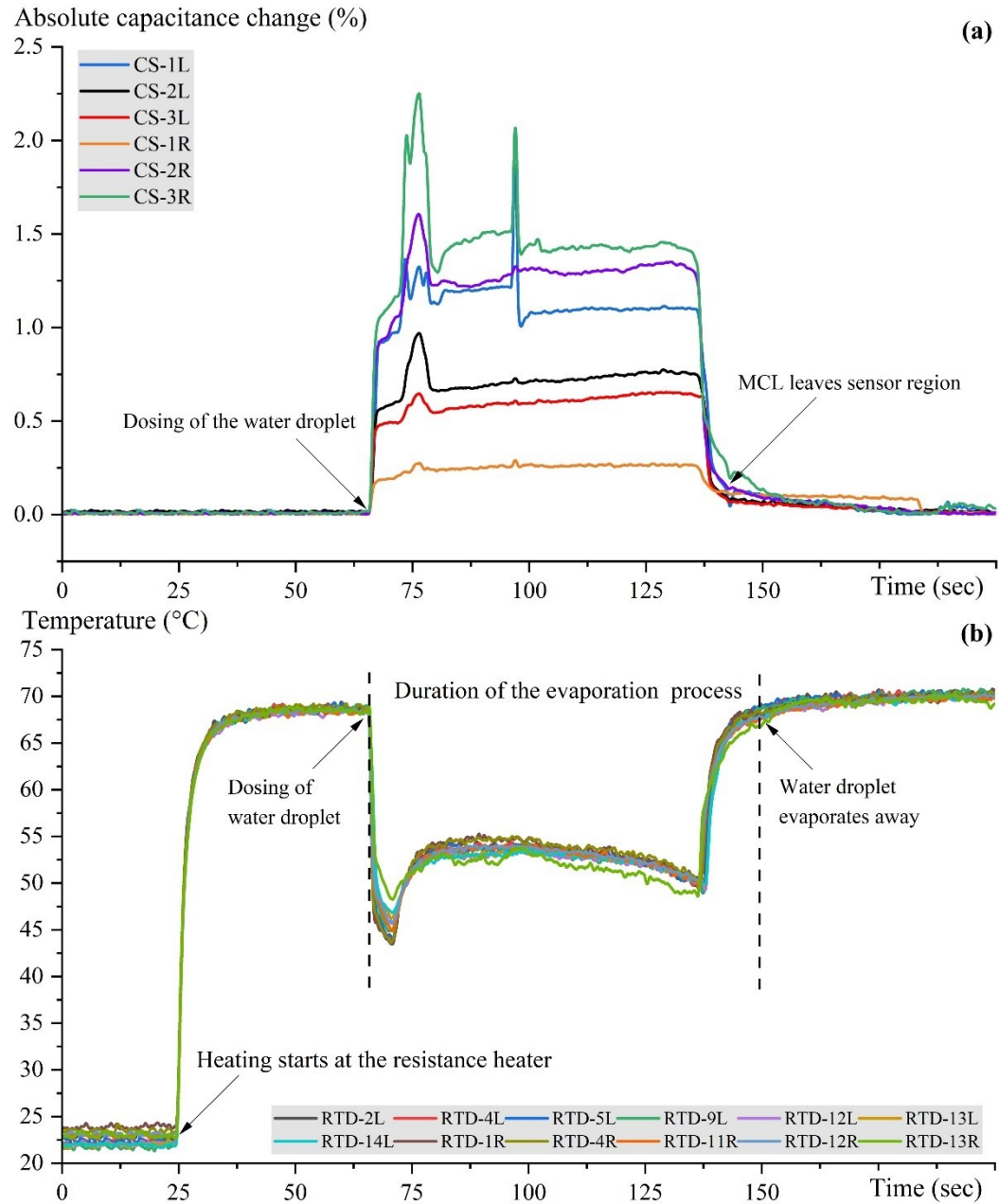


Figure 4-9: Evaporation process of a 6 μL water droplet on a heated polyimide surface at 69.7 $^{\circ}\text{C}$ (a) absolute capacitance changes with time using six capacitance micro-sensors (CS-1 to CS-6), (b) temperature distribution with time employing twelve functioning RTDs.

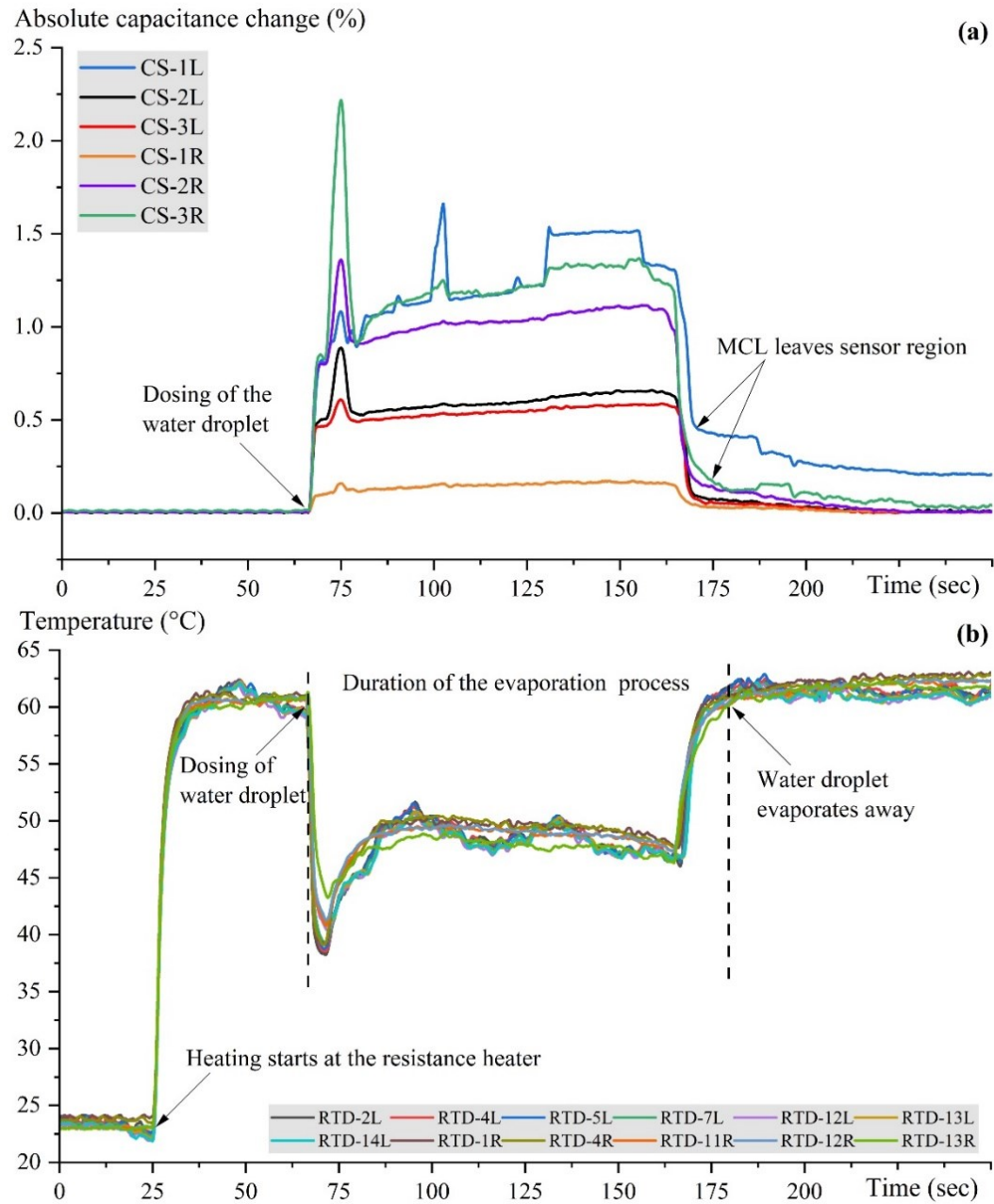


Figure 4-10: Evaporation process of a 6 μL water droplet on a heated polyimide surface at 61.0 $^{\circ}\text{C}$ (a) absolute capacitance changes with time using six capacitance micro-sensors (CS-1 to CS-6), (b) temperature distribution with time employing twelve functioning RTDs.

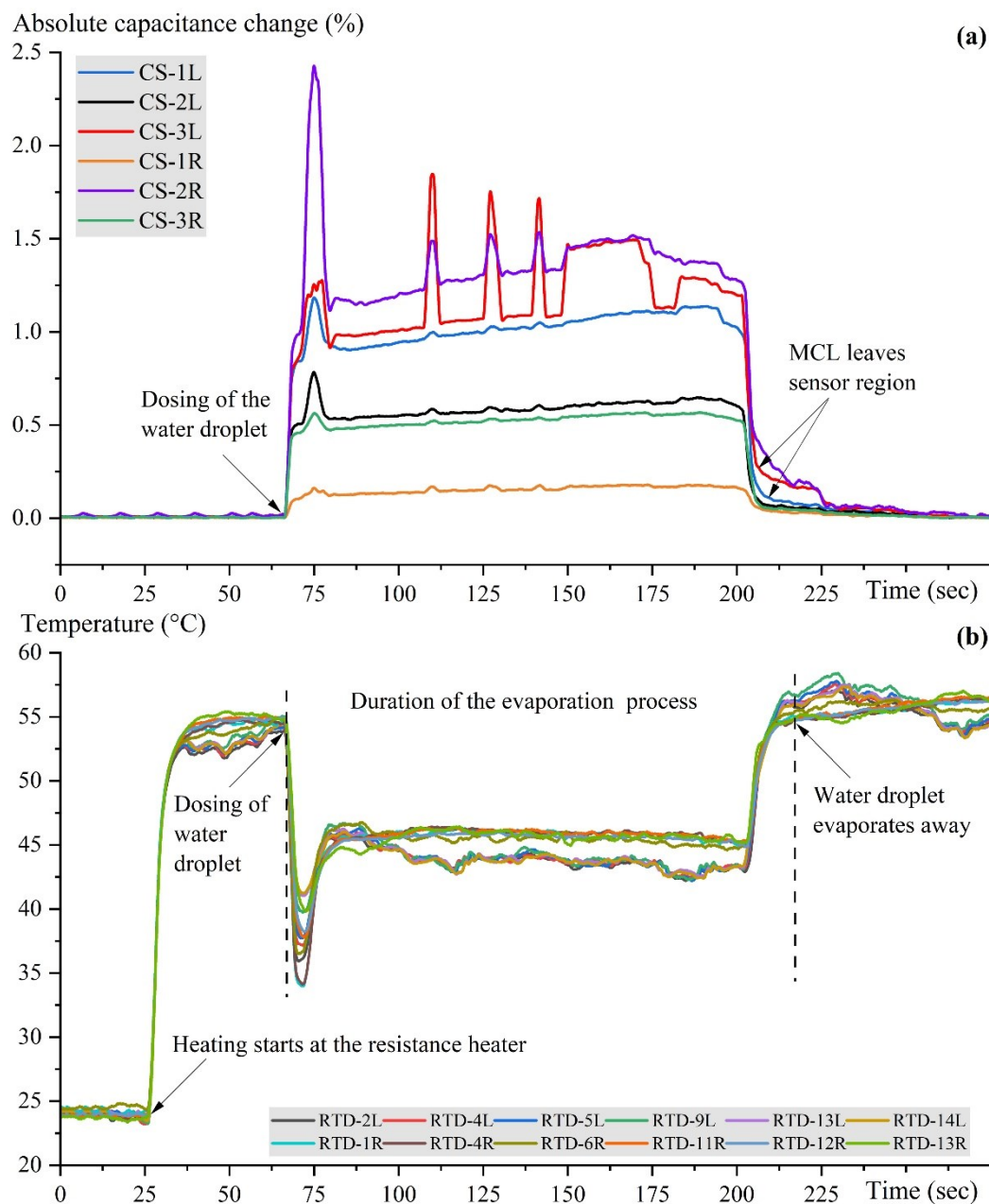


Figure 4-11: Evaporation process of a 6 μL water droplet on a heated polyimide surface at 53.0 $^{\circ}\text{C}$ (a) absolute capacitance changes with time using six capacitance micro-sensors (CS-1 to CS-6), (b) temperature distribution with time employing twelve functioning RTDs.

Figure 4-9 demonstrates that RTDs measured a greater temperature change during dosing of the water droplet where the MCL advanced over the sensing region compared to

the temperature change caused by the receding MCL at the end of the evaporation process. For example, during the experiment performed at a surface temperature of 69.7 °C, the advancing MCL caused an average temperature drop of 22.5 °C whereas the receding MCL near the end of the evaporation process produced a temperature rise of 19 °C. Similarly, the average temperature change caused by the advancing movement of MCL was, on average, 5.6 °C and 6.1 °C higher compared to the temperature changes caused by receding MCL near the end of the evaporation process for experiments performed at surface temperatures of 61.0 °C and 53.0 °C, respectively. As summarized in Table 4-1, these results show a non-negligible difference in temperature change caused by advancing and receding movement of MCL, and the magnitude of temperature difference depends on the surface temperature-dictated MCL speed. Further, the greater temperature change for an advancing MCL with comparable speed to a receding MCL is found to be greater, which is in agreement with existing studies [36], [37] and is attributable to deformation of the thermal boundary layer between the fluid and heated surface [62].

The temperature and MCL tracking data can be utilized to measure the timing and sequence of MCL passage, its associated thermal response, and the interdependence between these events, specifically focusing on shorter time windows. The local temperature distributions for experiments conducted at surface temperatures of 69.7 °C and 61.0 °C shown in Figures 4-12 and Figure 4-13 (left axes) demonstrate that when the water droplet evaporated away and the MCL was receding, the RTD on the right was first to detect the temperature changes associated with the passage of the MCL. These figures also exhibit sequential time lag among the RTDs, where the leftmost RTD was last to detect the temperature changes. The capacitance-based micro-sensors portrayed similar sequential

capacitance changes referring to the passage of the MCL. As also shown in Figures 4-12 and Figure 4-13 (right axes), the rightmost capacitance sensor CS-3R first detected the course of the MCL, whereas the capacitance-sensor CS-3L spatially located at the leftmost side was the last to report a change in capacitance signal. The collaged images captured via the DSA (Figure 4-4) demonstrated that the droplet's volume gradually reduced from the right to the left side of the device (relative to the center) due to the evaporation process, which provides a practical agreement with the data obtained from the micro-device. However, due to the unconstrained nature of the evaporation process, the passage of the MCL did not always follow this behavior for each experiment. The temperature distribution and capacitance change plots in Figure 4-14 depict a separate experiment where the water droplet first evaporated away from RTD-14L and RTD-6R was the last sensor to detect the temperature change, i.e., the movement of the MCL was in the opposite direction relative to the naming convention. The tracked passage of the MCL by the capacitance sensor array was identical to the response sequence reported by the RTDs, which validated the versatile functionality of this micro-device regardless of the direction of motion of the MCL of the evaporating droplets.

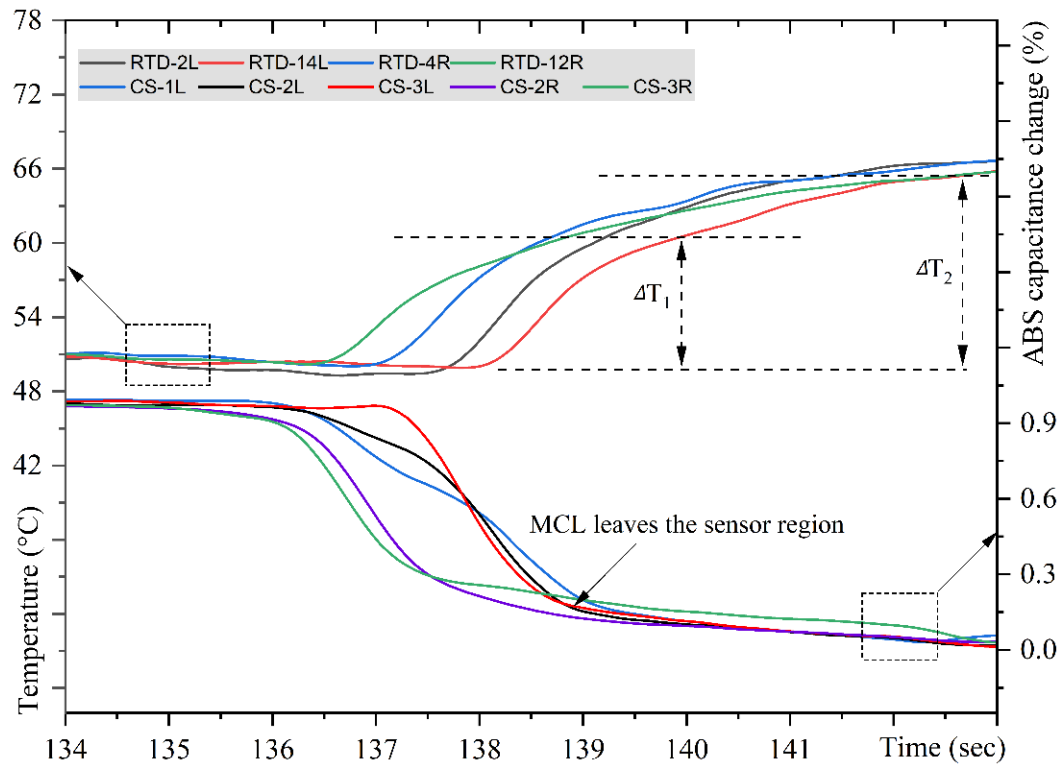


Figure 4-12: Local temperature distribution and change in capacitance signal on the outset of droplet evaporating away from the heated polyimide surface at 69.7 °C.

According to the experimental results in Figures 4-12 to 4-14, the capacitance sensor array reported the MCL passage *before* temperature changes, irrespective of the surface temperature during the experiments. The droplet evaporation study at 69.7 °C shows that capacitance-sensor CS-3L detected the transition of the MCL at 137.13 s, whereas the spatially equivalent temperature sensor RTD-14L detected the temperature change associated with this transition 0.81 s later. Similarly, experimental results at 61.0 °C show that capacitance-sensor CS-3L indicated a sudden fall in capacitance signal at 166.48 s, while it took 1.27 s longer for the corresponding RTD to demonstrate a change in temperature. While it has been previously known that the MCL serves as a region for significant heat transfer, these results show that the MCL passage precedes the actual

change in local surface temperature and that the duration of time between these events depends on the speed of the MCL as summarized in Table 4-1. For example, the speed of the receding MCL near the end of the evaporation process for the experiment performed at 69.7 °C was 0.95 mm/s, which facilitated a shorter time lag between MCL passage and associated thermal response. Conversely, the investigations conducted at 61.0 °C and 53.0 °C with slower speeds of receding MCL gave longer time lags between these two events. Table 4-1 reported only the time lags for the receding MCL movement associated with uninterrupted evaporation; in contrast, the advancing MCL associated with droplet dosing is considered a more artificial event required to begin the experiment under controlled and repeatable conditions.

Table 4-1: Summary of MCL passage, speed, and its effects on the thermal response for droplet evaporation.

Surface temperature	Advancing MCL speed**	Temperature change by advancing MCL	Receding MCL speed**	Temperature change by receding MCL	Time lag between MCL passage and thermal response
69.7 °C	1.31 mm/s	22.5 °C	0.95 mm/s	19.0 °C	0.81 s
61.0 °C	1.28 mm/s	19.8 °C	0.51 mm/s	14.2 °C	1.27 s
53.0 °C	1.29 mm/s	15.6 °C	0.47 mm/s	9.5 °C	1.43 s

** The propagated total uncertainty for MCL speed values is +/- 0.12 mm/s

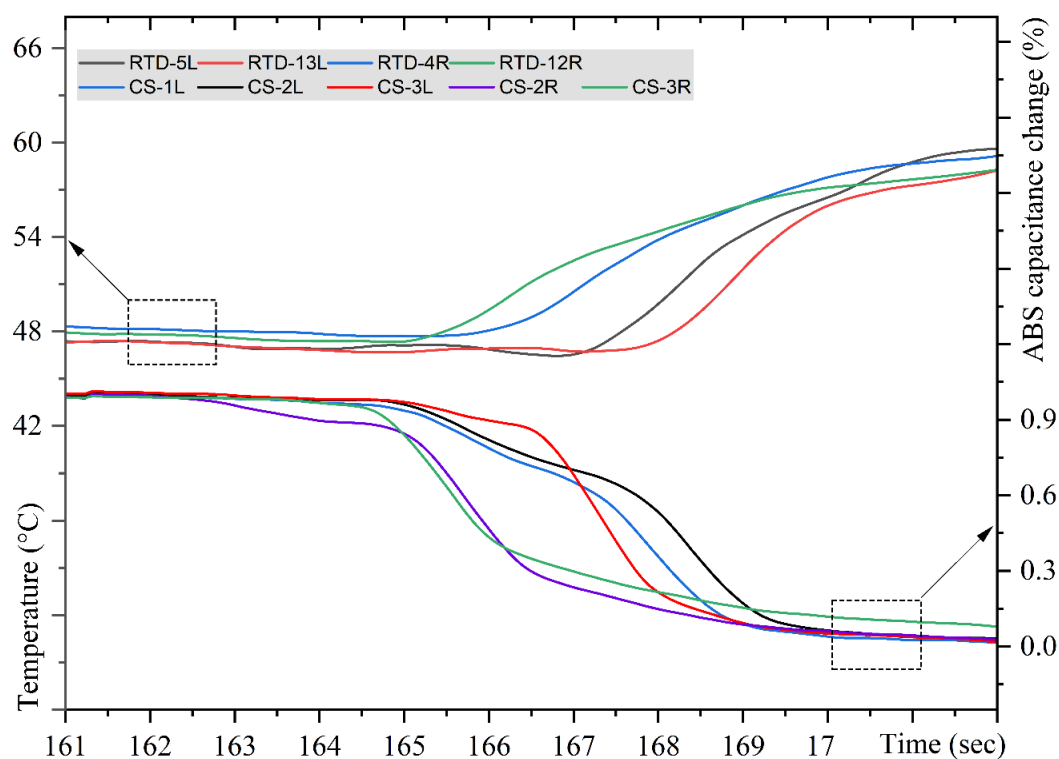


Figure 4-13: Local temperature distribution and change in capacitance signal on the outset of droplet evaporating away from the heated polyimide surface at 61.0 °C.

An in-depth analysis was conducted to determine the thermal time constant of an individual RTD. This was done to ensure that the observed time delay between the passage of MCL and the thermal response was not influenced by response lag in the RTDs. This analysis considered the dimensions of the RTDs, the lower bound heat transfer coefficient for an evaporating sessile droplet, and the thermophysical properties of platinum. This study also took into account the contribution of the four lead wires of the RTDs. The results of the conducted analysis showed that the thermal time constant of the RTDs was in the range of 0.5-1 ms, which is to be expected given the microscope size of the individual RTDs. Microfabricated temperature sensors have a rapid thermal response, which is one of their key advantages over macroscopic ones. This study has compared the results with the

observed time lag values presented in Table 4-1, which are on the order of 1-2 s, this study concludes that the speed of MCL propagation predominantly determines the time delay observed in the thermal response. The effect of response lag caused by resistance in the RTDs is negligible. It is important to note that the presence of surface contaminants can potentially affect the MCL's propagation speed on the microdevice's top polyimide surface. The sensing zone of the microdevice was gently cleaned after each experiment using cleanroom swabs soaked in acetone, isopropanol, and deionized water to prevent interference from surface contaminants.

According to the capacitance sensor data from CS-3L reported in Figure 4-12, the MCL of the evaporating droplet moved away from the sensor region at 138.96 s. Since the passage of the MCL preceded the actual change in local surface temperature and the time lag between these two events was 0.81 s; therefore 139.77 s revealed the exact temperature change associated with the MCL passage. In this evaporation process, the change in temperature due to MCL passage, denoted by ΔT_1 , was 9.7 °C, and the overall temperature change (ΔT_2) due to evaporation was 13.6 °C. The following equation yields the percentage temperature change due to MCL passage ($\Delta T_{MCL}(\%)$) relative to the overall temperature change. The calculated percentage change in temperature due to MCL passage was $71.3 \pm 3.7\%$ for the experiment conducted at the surface temperature of 69.7 °C.

$$\Delta T_{MCL(\%)} = \left(100 \times \frac{\Delta T_1}{\Delta T_2}\right) \quad \text{Eq. 4-3}$$

Results from the experiment performed at 61.0 °C showed that the temperature change due to the passage of MCL was 8.9 °C, which constituted $71.2 \pm 4.0\%$ of the total temperature change in the sensing zone. Experimental investigation at 53.0 °C also demonstrated a similar result, where the temperature rise associated with the transition of

MCL provided $71.0 \pm 5.4\%$ of the total temperature rise of $9.3\text{ }^{\circ}\text{C}$ due to the droplet's evaporation. Combinedly, these results show that the passage of the three-phase contact region of an evaporating droplet contributes more than 70% of the overall temperature change during the evaporation process. These results obtained are in excellent agreement with a recent study by Wang et al. Their work used a frequency domain thermo-reflectance method to measure the temperature profile underneath a static evaporating meniscus. They found a normalized cumulative heat transfer of 71% occurred within 1 mm of the meniscus edge [84].

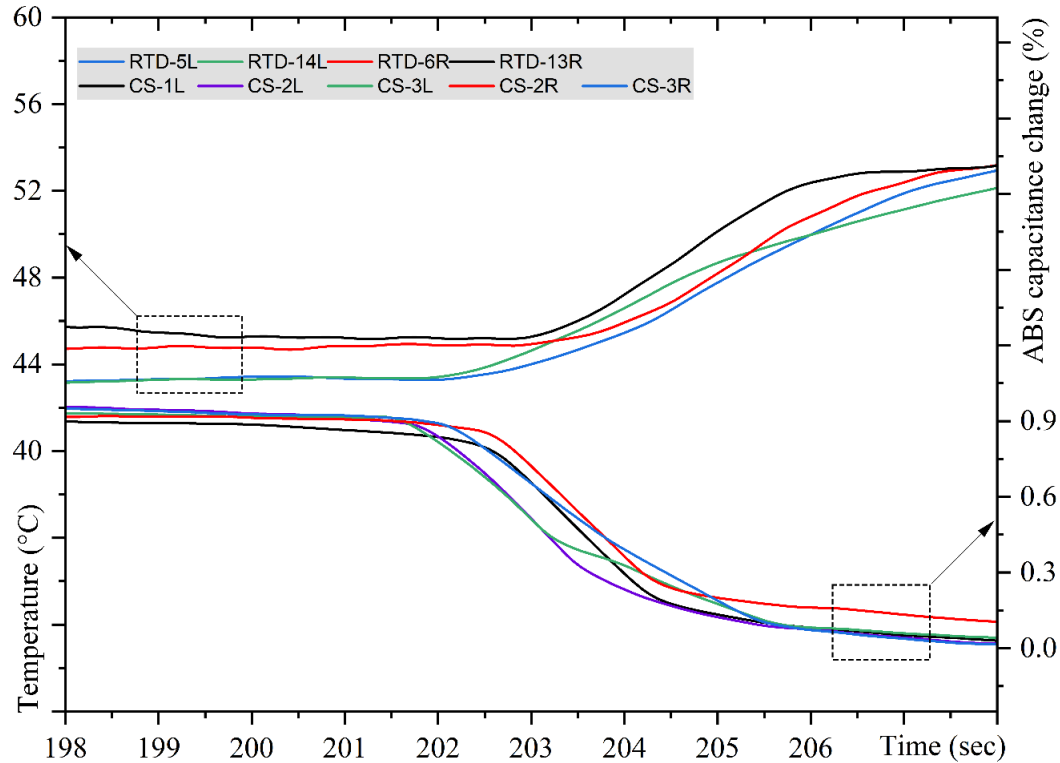


Figure 4-14: Local temperature distribution and change in capacitance signal on the outset of droplet evaporating away from the heated polyimide surface at $53.0\text{ }^{\circ}\text{C}$.

The data from the experiments can be further used to quantify the relationship between MCL passage and local vertical heat flux at the surface due to the evaporation

process. According to the schematic diagram of the cross-section of the microdevice shown in Figure 4-2(d), a 2.9 μm thin insulating layer of polyimide separates the resistance heater and top surface of the microdevice. If, at any instance, the top surface of the microdevice facilitates a temperature reading T_S , then according to one-dimensional heat conduction, the following equation yields the temperature of the resistance heater T_H .

$$Q = kA \frac{dT}{dx} = kA \frac{(T_H - T_S)}{dx} \quad \text{Eq. 4-4}$$

$$T_H = T_S + \frac{Qdx}{kA} \quad \text{Eq. 4-5}$$

where Q is the amount of heat transfer, A is the surface area, k is the thermal conductivity of polyimide, dx is the thickness of the polyimide, and dT/dx is the temperature gradient. Once the resistance heater's temperature is calculated, the following equation provides vertical heat flux values for each functioning RTD for experiments performed at three different surface temperatures.

$$q'' = k \frac{dT}{dx} = k \frac{(T_H - T_R)}{dx} \quad \text{Eq. 4-6}$$

where dx is the thickness of the polyimide layer that separates the resistance heater and the RTDs, and T_R denotes the temperature reading of the employed RTD. Finally, as shown in Figures 4-15 to 4-17, the calculated vertical heat flux values are normalized to the initial dry state to investigate the effect of liquid bulk and advancing-receding movement of MCL. The calculation of vertical heat flux is accomplished in two steps. Eq. 4-6 describes the calculation of the vertical heat flux based on two temperatures, T_H and T_R . T_H represents the heater temperature, which we first determined using the measurement of the device's surface temperature, T_S , and the heat produced by the heater, denoted as " Q " via Eq. 4-5, when no droplet was present. A simple 1D thermal resistance model shows that under these

experimental conditions, the thermal resistance vertically from the heater through the very thin polyimide layers is $\sim 30\times$ smaller than the thermal resistance of the much thicker soda lime substrate and more than $\sim 100\times$ small than lateral conduction thermal resistances such that practically all heat leaves via the top surface. Hence, we can utilize this model safely to determine T_H via measurements of T_S at known heater power values of Q . Second, when the evaporating droplet experiment is underway, we are measuring the local value of T_S via each RTD. This now becomes the value of T_S in the equation, and we solve for the local Q occurring in the vicinity of that RTD. Hence, we utilize the same 1D heat transfer model/equation for both parts, but in the first we know Q and T_S to determine T_H , and in the second we know T_H and T_S to determine the local Q .

Figures 4-15 to 4-17 show the normalized change in local vertical heat fluxes from resistance heater to evaporating droplet for the experiments performed at 69.7 °C, 61.0 °C, and 53.0 °C, where these vertical heat fluxes were calculated from the temperature gradients between resistance heater and RTDs having a vertical separation of 1.2 μm . In these experiments, the local heat flux has a maximum value immediately after dosing, as this is the region where the MCL of the droplet acts as an advancing interface and causes a more significant temperature change due to the deformation of the thermal boundary layer between the dosed water droplet and heated polyimide surface. As shown in Figure 4-15, the calculated heat flux for advancing MCL is, on average, 1.21 times the heat flux of receding movement of MCL near the end of the evaporation process.

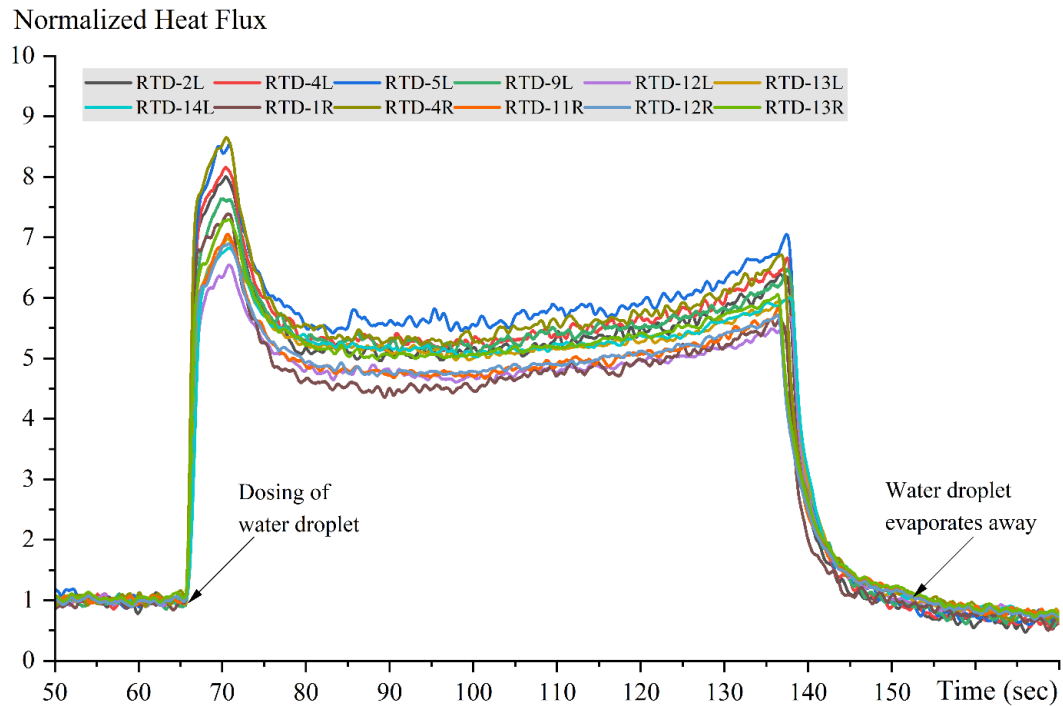


Figure 4-15: Normalized heat flux changes with time for an evaporating droplet on a heated polyimide surface at 69.7 °C.

From Figure 4-16, the average heat flux value for advancing MCL is 1.40 times the receding MCL. These results also indicate that the heat flux of the receding MCL due to evaporation depends on the MCL's speed as expected. To illustrate, the experiment performed at 69.7 °C enabled, on average, 6.15 times higher heat flux than the initial dry state with an MCL speed of 0.95 mm/s. In contrast, the experiment performed at a lower surface temperature of 61.0 °C facilitated a lower MCL speed of 0.51 mm/s for receding movement, which enabled 5.13 times higher heat flux than the initial dry state.

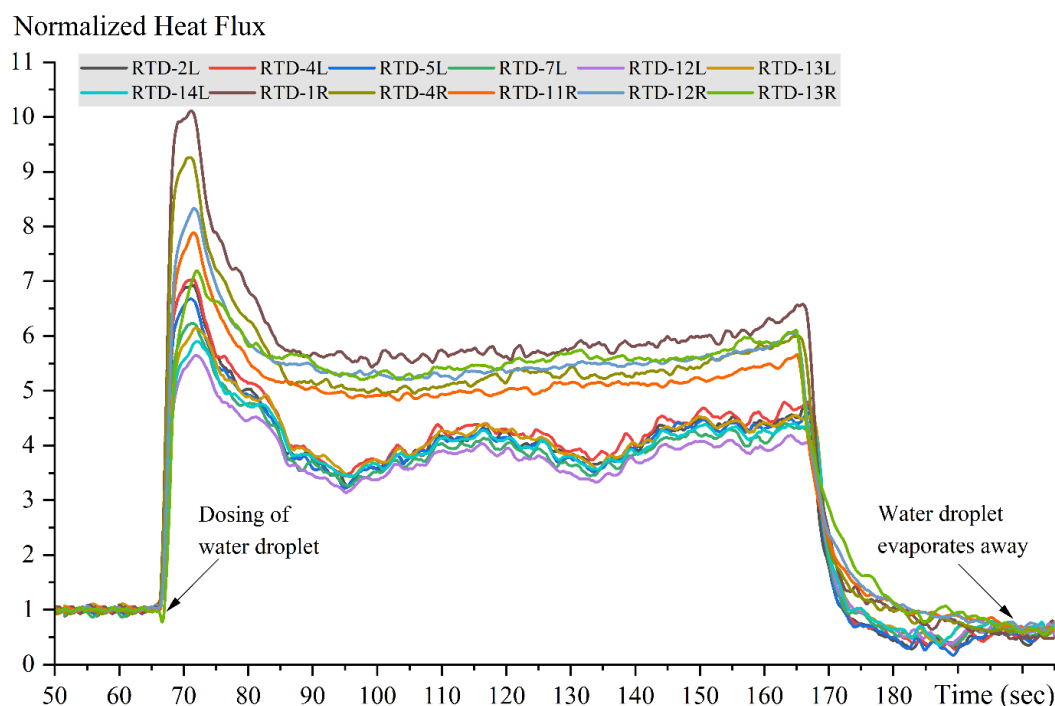


Figure 4-16: Normalized heat flux changes with time for an evaporating droplet on a heated polyimide surface at 61.0 °C.

Table 4-2: Summary of heat flux values caused by advancing MCL, receding MCL, and liquid bulk.

Surface temperature	Avg. heat flux caused by advancing MCL (x initial dry state)	Avg. heat flux caused by receding MCL (x initial dry state)	Avg. heat flux caused by liquid bulk (x initial dry state)
69.7 °C	7.45	6.15	5.22
61.0 °C	7.17	5.13	4.59
53.0 °C	5.50	3.59	3.42

The heat flux distribution shown in Figure 4-15 also indicates that as the MCL advances and recedes, it produces 1.43- and 1.18-times higher heat fluxes, respectively, compared to the heat fluxes produced by the liquid bulk region of the droplet. As summarized in Table 4-2, the evaporation studies at 61.0 °C and 53.0 °C shown in Figures 4-16 to 4-17 also exhibit a similar finding, where advancing and receding MCL generated

higher heat fluxes than the average heat flux caused by the liquid bulk. These results combinedly support the ideas that the MCL region facilitates the most significant heat transfer for droplet evaporation, the MCL passage produces the maximum local heat fluxes, and that local heat transfer at the MCL is greater for faster-moving MCLs.

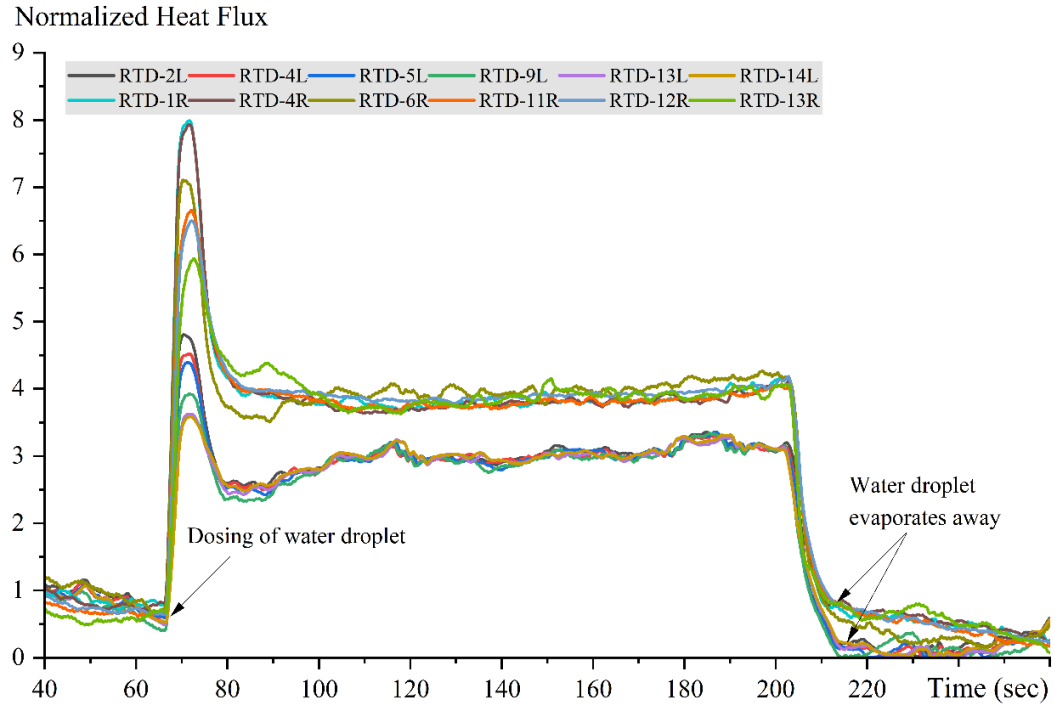


Figure 4-17: Normalized heat flux changes with time for an evaporating droplet on a heated polyimide surface at 53.0 °C.

As this microdevice measured surface temperature distribution with microscale precision, it is also possible to extract the lateral heat flux values at different times during the passage of the MCL. Since every functioning RTD represents a specific axial coordinate on the sensor region and the lateral temperature distribution plots (Figures 4-18 to 4-19) portray the temperature of these coordinates; therefore, the following equation yields the lateral heat flux.

$$q'' = k \frac{dT}{dx} \quad \text{Eq. 4-7}$$

Where k is the thermal conductivity of polyimide, dT is the temperature change, and dx is the spatial separation.

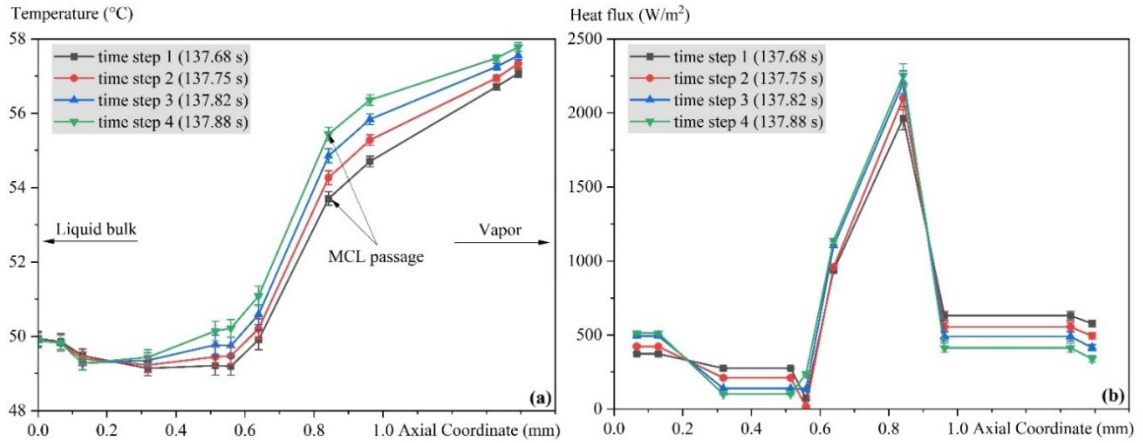


Figure 4-18: (a) Local temperature distribution, (b) distribution of lateral heat flux for a receding MCL at surface temperature of 69.7 °C.

Figures 4-18(a) and 4-19(a) represent the local temperature distribution underneath the evaporating meniscus at various spatial coordinates for experiments performed at 69.7 °C and 61.0 °C. Each of the twelve functioning RTDs employed for these experiments denotes a specific spatial coordinate in the sensing zone of the microdevice. RTD-14L at the leftmost of the sensed region is assigned a relative coordinate of 0 mm, and the remaining RTDs up to RTD-12R correspond to the other positive relative coordinates shown in Figures 4-18 and 4-19. These figures then give the temperature distribution underneath the evaporating droplet at four different times near the end of the evaporation process when the MCL is receding, where coordinates up to 0.64 mm correspond to the wall temperatures underneath the liquid bulk. The axial coordinate 0.84 mm indicates a

steep rise in wall temperature caused by the passage of the MCL, which is manifested as an increase in temperature with time.

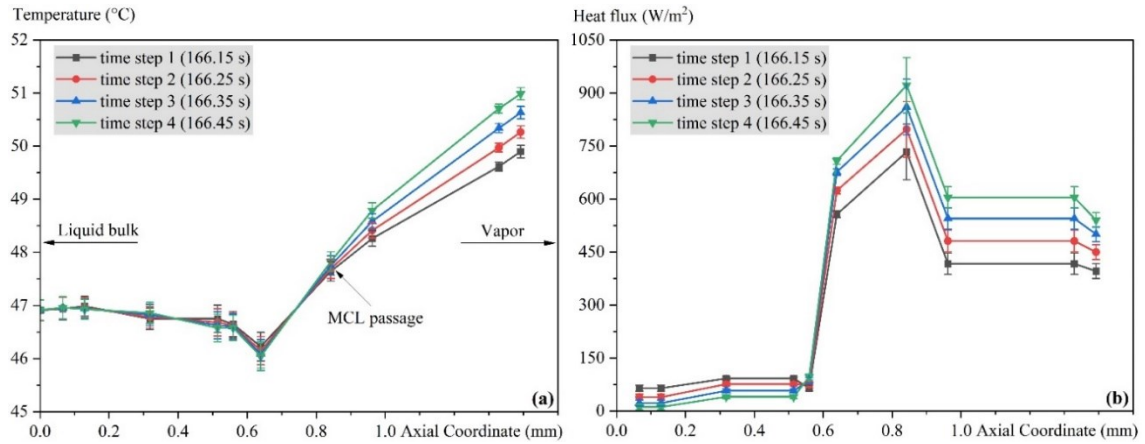


Figure 4-19: (a) Local temperature distribution, (b) distribution of lateral heat flux for a receding MCL at surface temperature of 61.0 °C.

Figures 4-18(b) and 4-19(b) show the lateral heat flux distributions calculated from the measured temperatures at different coordinates presented in Figures 4-18(a) and 4-19(a). According to the absolute capacitance change data shown in Figures 4-12 and 4-13, 136.29 s and 165.07 s denote the passage of the MCL from RTD-1R, which has a spatial coordinate of 0.84 mm. Since the MCL passage precedes the actual change in local surface temperature, the times shown in Figures 4-18 and 4-19 are chosen to portray the associated thermal response. The coordinate 0.84 mm demonstrates both experiments' maximum heat flux values, indicating the MCL passage from the sensor region. These results indicate that the lateral heat flux also depends on the MCL's speed. The average heat flux associated with the MCL's passage is 2132 W/m² for the experiment conducted at a surface temperature of 69.7 °C, which facilitates a receding MCL speed of 0.95 mm/s. According to the results shown in Figure 4-19(b) from the experiment conducted at the

surface temperature of 61.0 °C, the MCL speed of 0.51 mm/s provided a much lower average heat flux of 828 W/m², corresponding to the passage of the slower MCL.

In terms of macroscopic temperature response over the course of the experiment, the results of this study are qualitatively comparable to those of Chen et al. [85] and David et al. [86] despite differences in working fluid, interfacing surface, and experimental approach. They likewise reported a sharp decrease upon droplet deposition, followed by a gradual increase in temperature and another sharp change in temperature near the end of the evaporation process. Microscopically, the closest work to this may be the IR-based investigations of Ibrahim et al. [36] which utilized HFE7100 as the working fluid. While operating on microscopic RTDs rather than IR imaging analysis, this microdevice likewise allows to know the lateral temperature distribution across the contact line with microscopic resolution. Results in Figures 4-18(a) and 4-19(a) for lateral temperature distribution at two different surface temperatures depict a decrease in temperature occurring due to evaporation at the three-phase line before a notable increase in temperature as one moves from inside the liquid region to the vapor region without. Also, an increase in surface temperature/heat flux results in a deeper temperature dip. Similar observations were reported in Ibrahim et al. [36]. However, in that work the position of the contact line was defined as coinciding with the location of the local temperature minimum. This work does not rely on such a definition and instead has independent tracking the location of the contact line via the IDE sensors. This is an important distinction and a major part of the novelty and utility of this work. As shown in Figures 4-18(a) and 4-19(a), it is evident that the minimum temperature occurs just *inside* the contact line on the liquid side but still within 200-300 μm of the contact line location as measured by the IDEs. For comparison, the

lateral tracking resolution of this study for the contact line is estimated to be ~ 100 μm , and the entire region of the contact line's influence on temperature is approximately 600 μm .

A comparable discussion can be held regarding heat flux, which in this case is determined via the RTD-measured temperature distributions and also benefits from independent contact line sensing via the IDEs in a similar manner to above. Raj et al. [35] conducted numerical modeling to study the heat flux associated with the movement of the contact line of an evaporating droplet. They found that the heat flux initially increased to a maximum value at the moving contact line region and subsequently decreased due to the growing thickness of the liquid film in the bulk region. Ibrahim et al. [36] demonstrated that the defined contact line region exhibited the highest heat flux, attributed to its high evaporation rate. Here again, the current study aligns well with these previous works as depicted in Figures 4-18(b) and 4-19(b), which gives confidence as to its results. Similar to the temperature distribution discussion, however, the direct contact line tracking shows that the highest heat flux does indeed coincide with the MCL's passage for both surface temperatures without the need to infer such a conclusion. This supports existing theoretical and numerical studies that predict such phenomenon due to the strong gradients in the region. Quantitatively, Ibrahim et al. [36] found that the local heat fluxes near the contact line were 5.4-6.5 times higher than the mean heat flux. This work puts this ratio at about 5.50-7.45 for the faster-moving advancing MCL and 3.59-6.15 for the slower receding MCL cases, respectively. Additionally, Wang et al. [84] employed a frequency domain thermo-reflectance method to measure the temperature profile beneath an evaporating meniscus. They found that approximately 71% of the normalized cumulative heat transfer occurred within 1 μm of the meniscus edge. This finding is in excellent agreement with

this study, as Figures 4-12 to 4-14 demonstrate that the passage of the three-phase contact region of an evaporating droplet contributes to over 70% of the overall temperature change during the evaporation process.

4.4 Summary of Findings

This work investigated droplet evaporation on a heated polyimide surface at various temperatures, revealing the underlying physics behind the phase-change heat transfer and interdependence between the MCL and temperature distribution underneath an evaporating droplet. A microfabricated composite device comprising phase-interface sensing capacitance sensors and temperature sensing RTDs was employed to keep track of the MCL and measure temperature distribution underneath the evaporating meniscus. Experimental investigations were performed to determine the impact of MCL's speed and direction of motion on the overall evaporative heat transfer, where the results showed that the MCL precedes the actual change in local surface temperature and the timing differences between these events depends on the speed of the MCL. The following conclusions can also be drawn from the experimental investigations:

- The passage of the three-phase contact region of an evaporating droplet contributes more than 70% of the overall temperature change during the evaporation process.
- The time lag between MCL passage and associated thermal response depends on the speed of MCL. The evaporation study at 69.7 °C showed a time lag of 0.81 s with an MCL speed of 0.95 mm/s, while the experiment at 61.0 °C and 53.0 °C enabled extended time lag of 1.27 s and 1.43 s with slower MCL speed of 0.51 mm/s and 0.47 mm/s, respectively.

- Advancing MCL of an evaporating droplet due to dosing exhibited a more significant temperature change than the temperature change associated with a receding MCL due to evaporation. The magnitude of temperature difference caused by advancing and receding movement depends on the speed of the MCL; the higher the MCL's speed, the greater the temperature difference.
- The average heat flux value for advancing MCL was 5.50-7.45 times the initial dry state and 1.21-1.53 times higher than the receding MCL.
- The MCL region facilitated the most significant heat transfer for droplet evaporation. The advancing and receding MCL passage enabled 1.43-1.61 times and 1.05-1.18 times higher heat fluxes, respectively, compared to the heat fluxes produced by the liquid bulk region of the droplet.
- Due to the significant differences in wall temperature underneath the liquid bulk and MCL regions, the maximum local heat flux values occurred at the three-phase contact line.
- The lateral heat flux also depends on the MCL's speed and surface temperature. The MCL's speed of 0.95 mm/s provided 2.57 times higher heat flux in the MCL region compared to the experiment that facilitated an MCL's speed of 0.51 mm/s.

In the future, this custom-made composite micro-device is envisioned to study the evaporating meniscus of nonaqueous liquids, different liquid-surface interactions with varying wettability, and the dynamics of heat transfer and phase-interface behavior involved in droplet impingement and nucleate boiling processes.

CHAPTER 5

HEAT TRANSFER AND PHASE INTERFACE DYNAMICS DURING IMPACT AND EVAPORATION OF SUBCOOLED IMPINGING DROPLETS ON A HEATED SURFACE

5.1 Introduction and Motivation

Droplet impingement has ubiquity across natural events and has gained significant importance because of its broader applicability in various industrial and technological applications, including but not limited to spray cooling, fire suppression systems containing sprinklers, cooling of turbine blades, fuel-air interaction in internal combustion engines, and cooling towers [4], [5], [9], [87]–[92]. Due to the rise in power density, microelectronic industries have recently required cooling technologies with high heat removal capacity, where spray cooling has emerged as an effective technique with its outstanding capability of retaining uniform cooling temperature distribution throughout the heat flux surface [2], [5]. Studying hydrodynamics and local heat transfer for a single droplet impingement on a heated solid wall is essential to enhance a deeper understanding of the spray cooling technique and maximize overall effectiveness [4], [89], [92], [93]. Despite its ubiquity across natural and man-made events as outlined above, studying droplet impingement on a heated wall is not trivial as it is a complex phenomenon involving mass, momentum, and heat transfer interactions [4], [9]. The characteristics of the droplet and heated surface interactions mainly depend on the physical properties of liquid,

substrate properties, impact velocity, impact diameter, and surface temperature [4], [88], [89].

Table 5-1: Table of nomenclature.

u	Impact velocity (m/s)	$Ma = \frac{d\sigma}{dT} \frac{\Delta T L}{\mu a}$	Marangoni number
D	Impact diameter (m)	$Gr = \frac{g \beta \Delta T L^3}{\nu^2}$	Grahshoff number
ρ_w	Liquid density (kg/m ³)	$Bo = \frac{g \beta \rho L^2}{\frac{d\sigma}{dT}}$	Bond number
h_{fg}	Latent heat of water (kJ/kg)	Q_s	Heat transfer rate at the solid-liquid interface (W)
σ	Surface tension (N/m)	h_s	Heat transfer coefficient at solid-liquid interface [W/(m ² °C)]
V	Volume of the droplet (m ³)	$h_{liq/vap}$	Heat transfer coefficient at liquid-vapor interface [W/(m ² °C)]
r_d	Wetting radius (m)	Q_{sen}	Sensible heat transfer rate within droplet (W)
$L = \frac{V}{\pi R^2}$	Characteristic length (m)	$Q_{conv/ext}$	Convective (external) heat transfer rate (W)
μ	Dynamic viscosity (Ns/m ²)	Q_{rad}	Radiative heat transfer rate (W)
a	Thermal diffusivity (m ² /s)	$Q_{liq/vap}$	Heat transfer rate at the liquid-vapor interface (W)
g	Acceleration due to gravity (m/s ²)	C_w	Specific heat capacity of water [J/(kg°°C)]
β	Coefficient of thermal expansion (°C ⁻¹)	k_w	Thermal conductivity of water [W/(m°°C)]
ν	Kinematic viscosity (m ² /s)	R_{tot}	Total thermal resistance (°°C/W)
A_c	Droplet contact area (m ²)	$R_{drop,cond}$	Thermal conductive resistance within the droplet (°°C/W)
A_s	Droplet surface area (m ²)	$R_{liq/vap}$	Thermal resistance at liquid-vapor interface (°°C/W)
T_s	Surface temperature (°°C)	δ	Thickness of the droplet (m)
T_d	Droplet temperature (°°C)	t_{cond}	Time scale for heat conduction into the droplet (s)
ΔT	Temperature difference (°°C)		
$We = \frac{\rho_w D u^2}{\sigma}$	Weber number		

Droplet impact on a heated surface and subsequent evaporation comprises several physical phenomena that requires researchers to investigate from both heat transfer and hydrodynamic perspectives. Preceding studies have identified five distinct characteristic

behaviors: completely wet, wet film boiling, transition, dry rebound, and satellite dry rebound [4], [94]. When the surface temperature is lower than the saturation temperature of the liquid or insufficient to nucleate bubbles, the droplet spreads on the surface after impact and adheres to the surface throughout the evaporation process; this behavior is referred to as the completely wet/deposition impact behavior [4], [94]. When a droplet impacts a solid surface, it expands and spreads out, known as a spreading regime. Droplet impact velocity and surface wettability play the most crucial role in this regime [77], [95]. Once the droplet reaches its maximum spreading diameter, the liquid's surface tension initiates retraction, known as the receding regime. Liquid surface tension, surface properties, and wall temperature greatly influence the receding regime of an impacting droplet [96].

Surface temperature plays the most crucial role in influencing the phase interface and heat transfer phenomena involved with the droplet impingement on a heated surface and subsequent evaporation [89], [93]. Four distinct behaviors have been identified depending on the surface temperature and duration of evaporation of a single droplet on a heated surface: film evaporation, nucleate boiling, transition boiling, and film boiling [4], [97]. Film evaporation occurs when a droplet impacts a solid wall having a surface temperature below the saturation temperature of the liquid or even if the surface temperature exceeds the saturation point but is still inadequate to nucleate vapor bubbles [3], [4], [96]. A comprehensive review [4] of heat transfer mechanisms and hydrodynamics during droplet impingement on heated walls denoted that the overall heat transfer during the process strongly depends on the magnitude of surface temperature relative to the saturation temperature of the liquid. Other key factors that influence the droplet/surface

interactions are impact velocity, impact diameter, and the physical properties of the liquid [4]. A seminal experimental work on droplet impingement heat transfer revealed that the surface temperature and spreading characteristics of the droplet are the two most significant parameters that influence the overall heat transfer mechanisms [98], again highlighting the need to study impacting droplet phenomena from a multi-physics approach. Experimental and numerical studies by Gholijani et al. have demonstrated that the impact velocity of a droplet also significantly influences the heat transfer that occurs during the impingement. These studies have demonstrated that the higher impact velocities lead to higher heat transfer due to the higher maximum spreading diameter, resulting in higher temperature differences at the solid-liquid interface [89], [92].

In recent studies, researchers have used advanced techniques such as high-speed imaging, interferometry, and total internal reflection schemes to investigate the interfacial behavior of the impacted droplet. This includes the impact, spreading characteristics, and correlation with the local heat transfer mechanisms [94], [99]–[101]. Experimental investigations and numerical simulations on spreading behavior have demonstrated that the overall heat transfer process due to droplet impingement comprised three subsequent segments: droplet spreading, droplet receding, and sessile droplet evaporation [91], [102]. It is worth mentioning that experimental investigations have deduced the three-phase contact line or moving contact line (MCL) as the region with the highest heat transfer during droplet impact and evaporation on a heated surface [103], [104]. The recent work on sessile droplet evaporation conclusively proved this via independent microscale measurements of surface temperature and contact line movement [105]. In one of their experimental studies, Lee et al. combined a MEMS device and high-speed imaging, which

denoted that the maximum heat transfer occurs at the droplet spreading phase right after the impact resulting from the maximum temperature difference between the cold liquid and the solid heated substrate [106].

While numerous experimental and numerical studies have been conducted in the literature to explore hydrodynamics and heat transfer mechanisms during droplet impingement, the number of studies focused on measuring the microscopic thermo-fluid phenomena near the MCL region is limited, explicitly correlating the phase interface behavior with associated temperature change. Due to its complex nature, when it comes to investigating phase-change heat transfer at the microscale, it is essential to correlate the interdependence of heat transfer mechanisms with dynamic phase interface behavior, requiring more sophisticated and multifaceted sensing schemes. Moreover, there are only a few comprehensive studies in the literature that focus on studying the influence of significant parameters such as surface temperature and impact velocity as well as denoting the specific contribution of the heat transfer regimes like conduction, convection, and surface evaporation during droplet impingement and subsequent evaporation. Quantifying and differentiating the distinct heat transfer regimes, their transition, overall magnitude, and dependence on the surface temperature and impact velocity is another pressing need for improving heat transfer models, optimizing droplet surface interactions, and enhancing overall effectiveness. Previous studies have mainly focused on measuring heat transfer dynamics and often used external equipment such as high-speed cameras and optical image processing to evaluate interfacial behavior. These techniques' macroscopic spatial resolution and visibility, i.e., line of sight and viewing angle, often hamper precise detection of the location and temperature gradient in the MCL region. This study utilized

a custom-designed MEMS device for independent, real-time temperature measurements and simultaneous microscale tracking of the MCL during droplet impingement on the heated surface of the device and subsequent evaporation.

To the best of the authors' knowledge, there has been no investigation so far that combines the exploration of various heat transfer regimes occurring during droplet impingement and subsequent evaporation, along with examining the impact of influential parameters such as impact velocity and surface temperature for subcooled impinging droplets. In this study, the impinging droplets have been experimentally investigated via a custom-designed MEMS device to explore the interdependence of underlying heat transfer mechanisms at the three-phase contact line region with the simultaneous tracking of the phase interface behavior. Apart from investigating the effect of impact velocity and surface temperature for subcooled impinging droplets, this work mainly focused on discerning the specific contribution of conduction, convection, and surface evaporation throughout the process. The findings of this study regarding the transition from initial heat conduction to quasi-steady surface evaporation and effective heat transfer rates associated with these can lead to more accurate models for phase-change heat transfer processes and maximize overall effectiveness. Furthermore, the device used in this work can track the MCL behavior and temperature measurements simultaneously at the microscale in real-time. A minimally invasive device like this can pave the way for new possibilities in thermal management and process control in high-precision manufacturing and electronics cooling.

5.2 Methodology

Most studies in this field have predominantly employed infrared thermography (IR) or macroscopic temperature sensing probes to measure the temperature distribution due to

the impact and the subsequent evaporation of impinged droplets from heated walls. Although IR is a widely used technique in literature, it is only applicable for measuring temperature distribution in places where optical access to the surface is available. The limitation of resolution of other macroscopic temperature sensing probes and wavelength diffraction limit of infrared thermography often restricts their applicability in microscale temperature measurement. However, all these methods' knowledge of temperature distribution alone does not provide critical insights into the interdependence of phase-interface dynamics and heat transfer mechanism on a microscale. Thus, it requires a sensing scheme for microscale tracking of the MCL to unlock a meaningful correlation between the phase interface and the heat transfer mechanisms involved in dynamic phase-change heat transfer processes. When it comes to tracking the location of the MCL, most of the previous works employed high-speed optical imaging and post-processing of infrared images. These techniques usually infer the MCL as the region coinciding with local temperature minimum and high heat flux values. However, these methods have limited accuracy due to their macroscopic spatial resolution and visibility, which is restricted by the line of sight and viewing angle, making it difficult to detect the exact location and temperature gradient in the MCL region. To overcome these barriers and reveal new insights, a composite MEMS device was utilized in this work to measure the temperature changes and monitor the location of the MCL of the droplet throughout the heat transfer process simultaneously on the microscale. This microdevice also includes a thin-film resistance heater that maintains a desired surface temperature, making it an independent experimental setup for investigating phase-change heat transfer processes.

5.2.1 Microdevice Overview

Figure 5-1 displays the laser microscopic images of the fabricated composite microdevice utilized in this study to investigate the heat transfer process due to droplet impingement. This microdevice consists of three metal layers where a thin layer of polyimide provides electrical insulation between each two consecutive metal layers. This microdevice adopted a commercially available silicon wafer with a PECVD grown 2 μm thick silicon nitride on top as the starting substrate. The initial metal layer deposited on the starting substrate acts as a thin film resistance heater to achieve the desired surface temperature. A series of resistance temperature detectors (RTD) was deposited as the second metal layer on top of the first insulation layer of polyimide. The RTDs provided temperature distributions underneath the impacted droplet, where the minimum spatial separation between two consecutive RTDs is 20 μm . A 1.2 μm deposited thin polyimide film served as the second insulation layer that separated the RTDs from the capacitance sensors and provided electrical insulation between the top two metal layers of the microdevice. An array of capacitance microsensors based on interdigitated electrodes (IDEs) was the microdevice's third and final metal layer. These IDE-based microsensors detected droplets and kept track of the moving contact line throughout the experiment, as described in more detail within the previous works [107], [108]. A 500 nm thin polyimide layer was deposited as the topmost protective coating, acting as the solid heated wall during droplet impingement. The sensing zone of the microdevice spans over a region of 1500 μm .

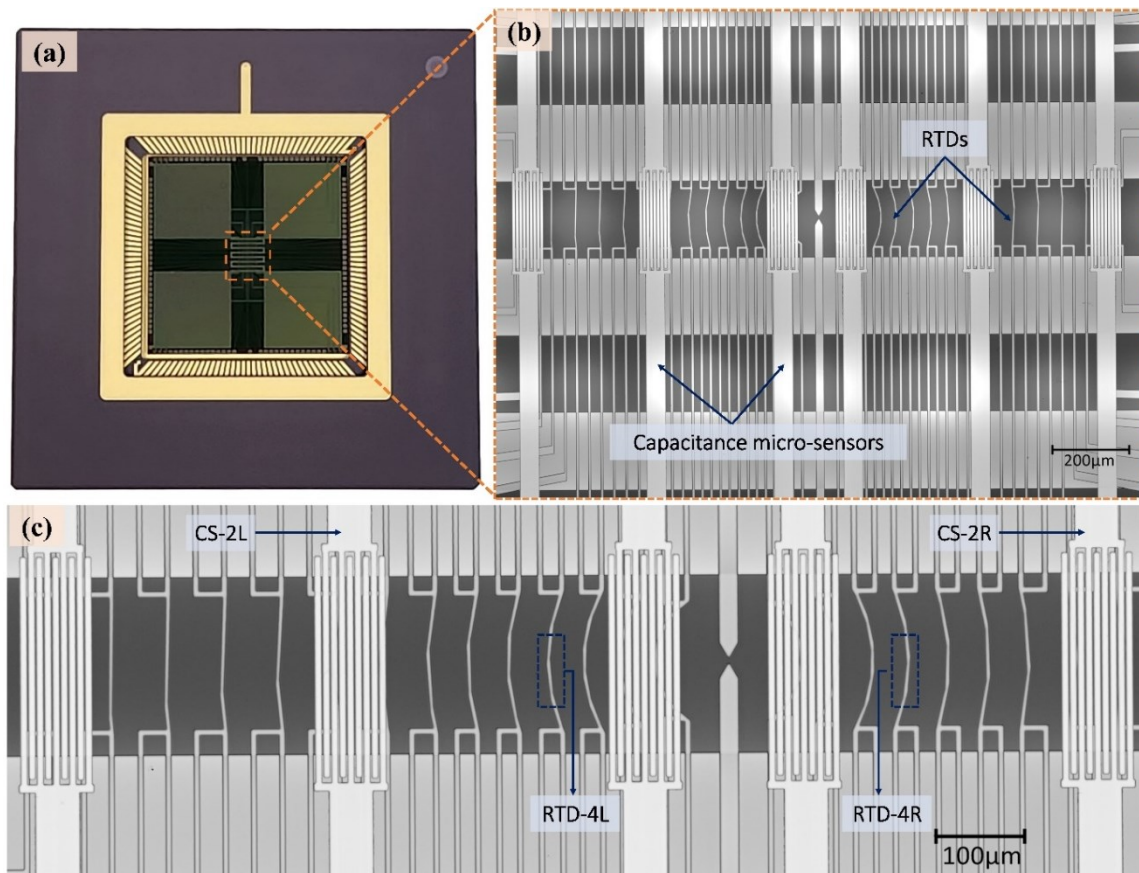


Figure 5-1: Optical images of the composite microdevice employed for investigating droplet impingement: (a) the microdevice attached to a ceramic chip carrier; (b) microscope image of the microdevice's sensing zone comprising RTDs, IDE-based capacitance microsensors, and a resistance heater; (c) a detailed view of the sensing zone, showcasing IDEs and RTDs.

A naming convention was followed for the microdevice's RTDs and IDE-based capacitance sensors. According to Figure 5-1, the RTDs and IDEs located on the right and left side of the microdevice's center are labeled with "R" and "L," respectively, after their corresponding number, where "1" refers to the one nearest to the center and "14" indicates the farthest from the center. To illustrate, RTD-1L is the closest temperature detector to the center of the device on the left side, whereas RTD-14R is the most distant from the device's center on the right side. The IDE-based capacitance sensors are named with the short form

of "CS" and follow the same naming convention as the RTDs. To learn more about this composite microdevice, refer to the previous work reported in Chapter 4, where this microdevice was employed to investigate heat transfer mechanisms and phase-interface behavior during the evaporation of sessile droplets from a heated polyimide surface.

5.2.2 Experimental Setup

This study adopted an experimental setup that consists of a sample stage underneath a syringe controlled by a drop shape analyzer equipment (DSA 25E, KRÜSS Scientific). The DSA provided controlled dosing of water droplets during each experiment. An optical camera attached to the DSA recorded the droplet changes throughout the evaporation process after the impact. The volume of water droplets was 6.0 μL for all the experimental results shown in this article. The droplet's volume was chosen in a way so that it entirely covered the sensing zone of the microdevice upon impact. To dose such small-scale droplets, we utilized a working fluid comprised of 90% deionized water and 10% isopropanol. Isopropanol decreased the surface tension and made it possible to dispense small-scale droplets capable of gravity-induced detachment while minimally changing the fluid properties of deionized water.

Due to the relatively small capacitance change caused by the droplet, a supporting circuit was employed to ensure a detectable capacitance change. The supporting circuit consists of an operational amplifier, an RC oscillator circuit, and a reference capacitor connected in parallel with the capacitance sensor employed for tracking the moving contact line of the impacted droplet. Please refer to the previous work in Chapter 4 for more details on this capacitance sensing and calibration of the RTDs.

During the experiments, a high-speed B/W camera (VEO 410L, Phantom) was utilized to observe droplet impact and subsequent changes in hydrodynamics. The recorded video/images were post-processed via Phantom post-processing software to evaluate the impact velocity, diameter, and duration of spreading and receding phases of the impacted droplets. The resolution and framerate of the captured images were 1280 x 800 pixels and 1000 frames per second, respectively.

This study investigated heat transfer due to droplet impingement on the heated top polyimide surface of the microdevice at various impact velocities ranging from 0.58 to 1.35 m/s. Analyzing the time-elapsd images captured by the high-speed camera while the droplet was in flight just before impact made it possible to calculate the accurate impact velocities. The impact velocities were varied by simply adjusting the height of the syringe controlled by the DSA from the top surface of the microdevice.

The temperature sensing uncertainty was analyzed by measuring the standard deviation of initial temperature readings from each RTD. Please refer to the previous work in Chapter 4 for more details on this measurement uncertainty analysis. A sampling at 100 Hz provided adequate data for precise measurement, and repeating experiments three times on each surface temperature enabled accurate precision estimation.

Although the RTDs of this microdevice allowed for higher sampling rates when working independently, for optimal accuracy and in cases of combined data acquisition with IDE-based capacitance sensors, a sampling rate of 100 Hz was used for all experiments reported in this work. This sampling rate was optimal given that all experiments involved subcooled impinging droplets and the overall length of the evaporation process was in tens of seconds.

The impact of air currents or large-scale convective flows on the sensitivity of the RTDs or IDEs of the microdevice was investigated since all the experiments were conducted in an open environment. The measured capacitance and temperature data from the RTDs and IDEs did not exhibit any fluctuations above the signal noise levels before the impingement of the droplets that abrupt air currents or larger-scale convective flows can cause. The changes in signals occurred exclusively due to the droplet impact and subsequent evaporation, and the change in magnitude was sufficiently greater than signal noise levels, indicating the effect of air currents or large-scale convective flow was negligible in comparison.

5.3 Results and Discussion

5.3.1 Hydrodynamic Perspectives

Time-elapsed images of 6.0 μL impacting droplets on the top polyimide surface of the microdevice at varying impact velocities are shown in Figure 5-2. A high-speed B/W camera (VEO 410L, Phantom) captured the moment of impact and subsequent changes in the spreading diameter and shape of the impacted droplets. Figures 5-2 and 5-3 show that a period up to 6 ms refers to the droplet spreading regime as the impacted droplet reached its maximum spreading diameter regardless of the impact velocity or associated Weber (We) number. As the droplet visualization depicts, the droplet spreading regime involves the radially outward movement of the impacted droplet.

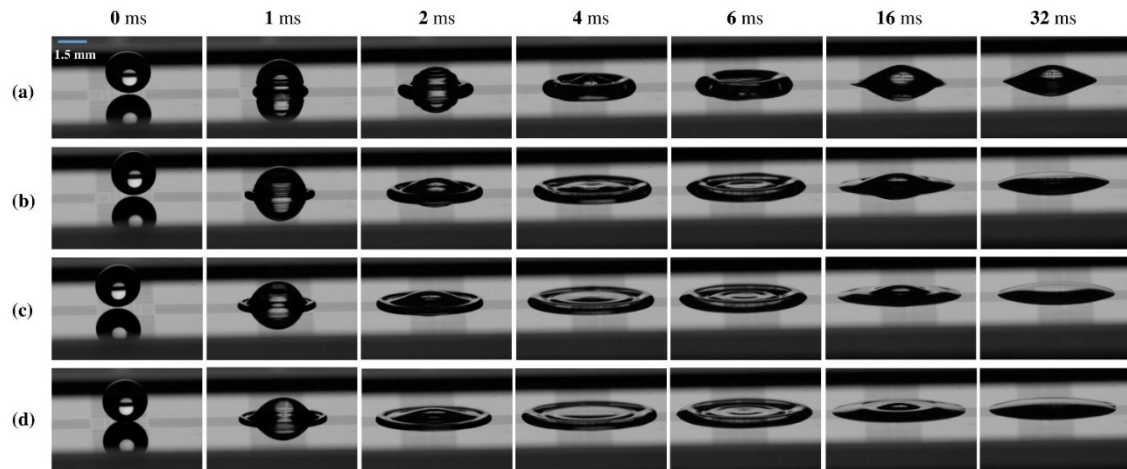


Figure 5-2: Time elapsed images of impacting droplets on a polyimide surface at four different impact velocities: (a) 0.58 m/s ($We = 11.2$), (b) 1.05 m/s ($We = 36.7$), (c) 1.22 m/s ($We = 49.2$), (d) 1.35 m/s ($We = 60.7$).

Impact velocity and We number (a dimensionless parameter that denotes a ratio of inertial to surface tension forces) are the two significant parameters that influence the impact characteristic patterns [77], [95]. According to the experiments reported in this work, the higher Weber number or impact velocity led to the maximum spreading diameter of the impacted droplets. To illustrate, at 6 ms an impact velocity of 0.58 m/s ($We = 11.2$) exhibited the lowest value of 5.16 mm as the maximum spreading, whereas an impact velocity of 1.35 m/s ($We = 60.7$) facilitated the highest spreading diameter of 7.15 mm.

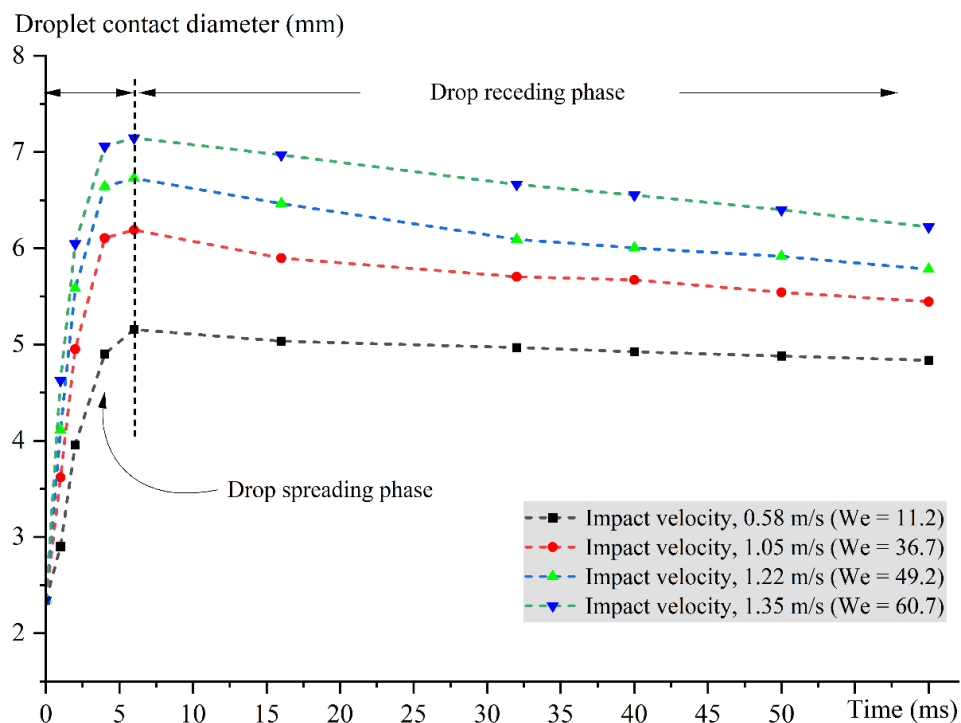


Figure 5-3: Evolution of droplet contact diameter with time at varying impact velocities (discrete points are connected through dashed lines to show the trend).

As time-elapsd images depict, once the droplet spread to its maximum extent, the surface area of the droplet started to shrink because of the dominant surface tension forces of the liquid. As shown in Figure 5-3, the spreading diameter of the impacting droplets gradually decreased until they reached their equilibrium state. This phase is known as the droplet-receding regime, leading to the subsequent sessile droplet evaporation phase.

As the experimental setup section described, DSA dosed a consistent volume of impacting droplets during each experiment and recorded the evaporation process. DSA also kept track of the contact diameter and changes in contact angle throughout the evaporation process via its image analysis software. Experiments involving droplet impingement and subsequent evaporation at varied surface temperatures demonstrated a consistent trend regarding changes in contact angle and diameter. Figure 5-4 illustrates a representative plot

depicting the evolution of diameter and contact angle over time of the impinging droplet at a surface temperature of 80.9 °C. As shown in Figure 5-4, at the beginning of the evaporation process, there is a brief period where the contact angle increased to its maximum value of 49.5° from its initial value of 39.6°. Approximately 57% of the total duration of the evaporation maintained a constant contact angle (CCA) phase, followed by a phase with a sharp reduction in contact angle. During this phase, the evaporating droplet held a nearly constant contact diameter, known as the constant contact diameter (CCD) phase. This CCD phase constituted about 27% of the total duration of the evaporation process.

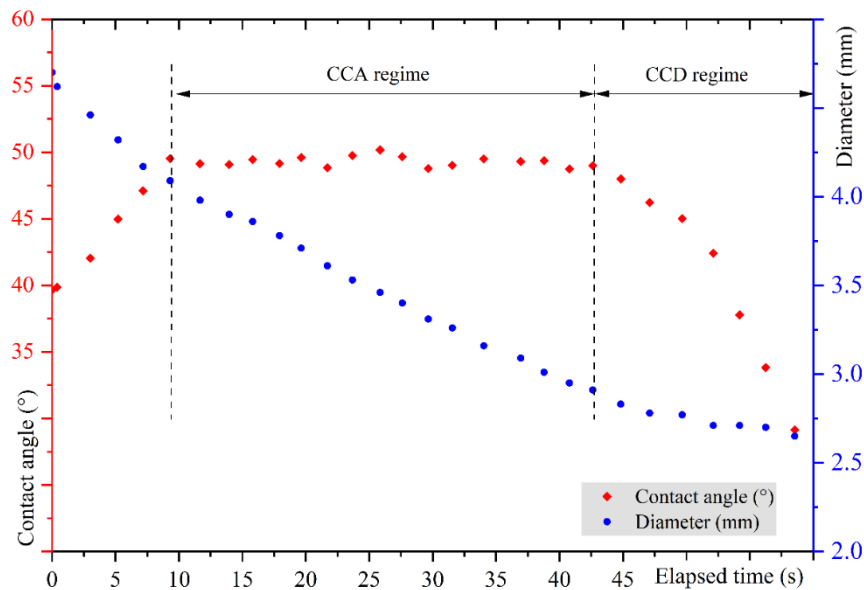


Figure 5-4: Evolution of diameter and contact angle over time of a 6.0 μL impacting water droplet on the polyimide surface at the surface temperature of 80.9 °C.

5.3.2 Heat Transfer Perspectives

Figure 5-5 shows the temperature change and vertical heat fluxes when a droplet impacts the heated top polyimide surface of the microdevice at various impact velocities ranging from 0.58 to 1.35 m/s. Analyzing the time-elapsed images captured by the high-

speed camera while the droplet was in flight just before impact made it possible to calculate the accurate impact velocities. As shown in Figure 5-2, for all experiments reported in this work, water droplets completely covered the sensing zone of the microdevice upon impact. As a result of droplets impinging onto the heated surface of the microdevice, the measured temperature change by the RTDs demonstrated a sudden and simultaneous decline. Since all the RTDs of the microdevice employed during experiments showed the same temperature change within the experimental uncertainty of ± 0.5 °C during and initially after impact, for the clarity of presentation, we chose RTD-2L located in the center of the device to demonstrate the temperature changes due to the impingement of a 6.0 μ L water droplet at varying impact velocities while maintaining the surface temperature at 72.9 °C. As Figure 5-2 demonstrates, the higher impact velocities resulted in a greater spreading diameter of the droplet, facilitating a larger contact area between the heated polyimide surface and the impacted droplets. The larger contact area allowed higher heat transfer from the heated surface to the liquid droplet. Consequently, the highest impact velocity resulted in the highest temperature drop and contained the maximum magnitude of vertical heat flux, as shown in Figure 5-5. Please refer to the “Methodology” section of Chapter 4 for more details on the vertical heat flux calculations.

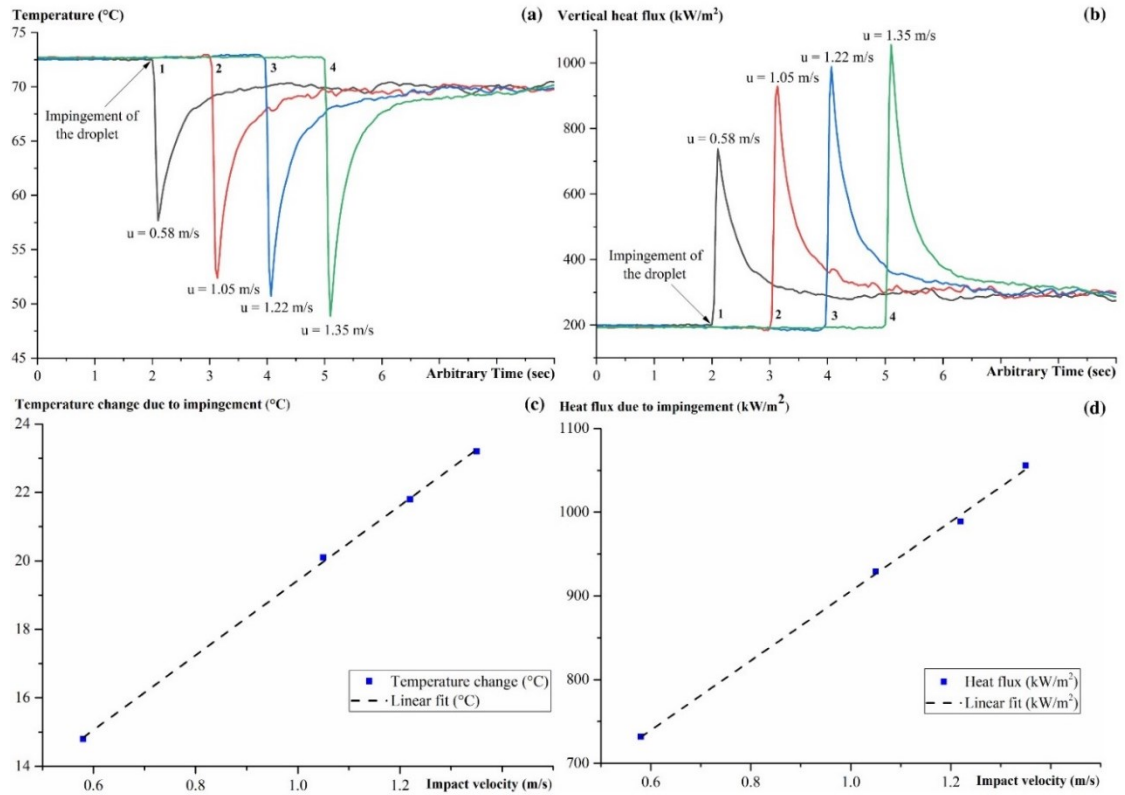


Figure 5-5: Influence of varying impact velocities u during impingement of a $6.0 \mu\text{L}$ water droplet on the heated polyimide surface of the microdevice at 72.9°C , (a) change in temperature over time, (b) heat flux values over time for varying impact velocities, (c) temperature change due to impingement vs. impact velocities, (d) heat flux due to impingement vs. impact velocities.

The surface temperature of the solid wall also significantly impacts the amount of heat transferred upon droplet impingement. The experiments were conducted in the film evaporation regime, where the effects of varying surface temperature for $6.0 \mu\text{L}$ water droplets were investigated by keeping the impact velocity constant. Figure 5-6 shows the temperature changes and heat flux values due to droplet impact on the heated polyimide surface of the microdevice at four different surface temperatures ranging from 53.3°C to 74.5°C . The impact velocity of the droplet impingement was 1.05 m/s for all four experiments, and these results were merged in a single plot by arbitrarily shifting along the

time axis to aid in visibility. Figure 5-6 exhibits experimental results in ascending order of the surface temperature, where “1” and “4” dictate the lowest and highest surface temperatures, respectively, out of the four. A higher surface temperature facilitated a more significant temperature difference between the impacting droplet and the heated surface; as a result, temperature drop and vertical heat flux values due to droplet impingement were more significant in magnitude for experiments with higher surface temperatures.

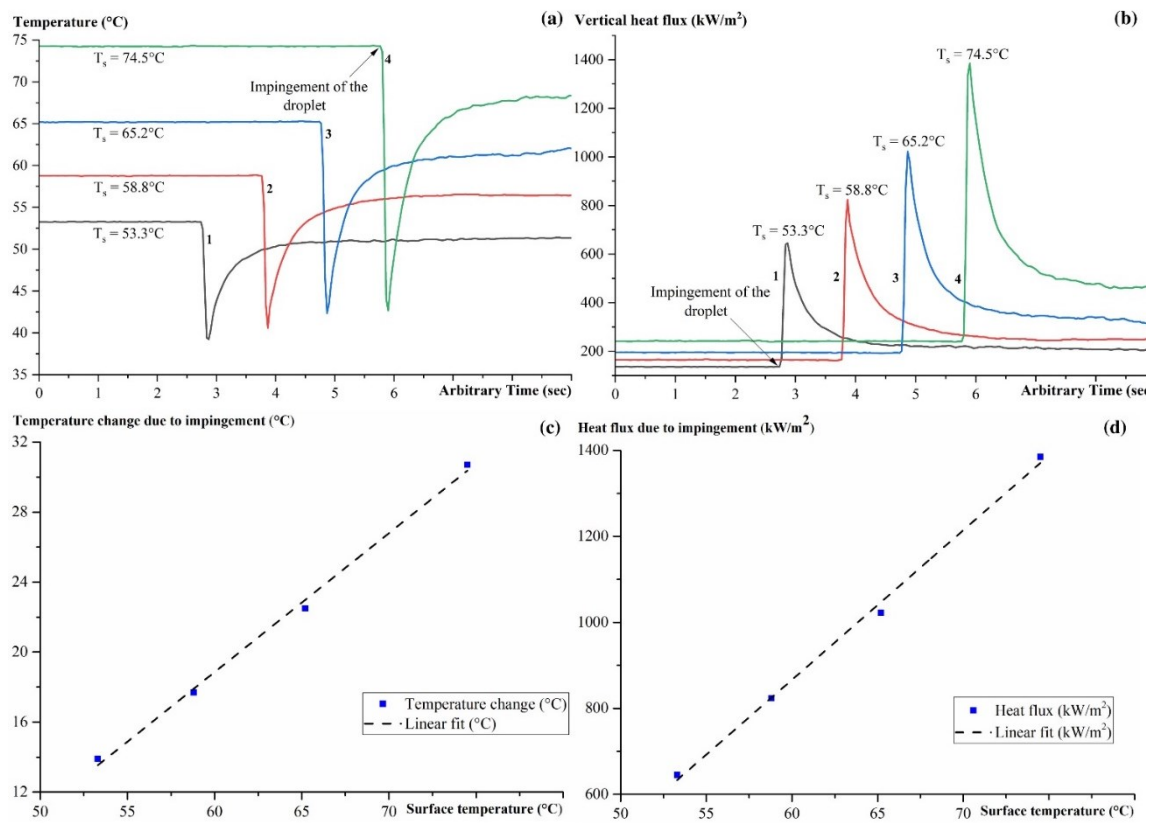


Figure 5-6: Influence of varying surface temperatures during impingement of a 6.0 μL water droplet on the heated polyimide surface of the microdevice at $u = 1.05 \text{ m/s}$: (a) change in temperature over time, (b) heat flux values over time for varying surface temperatures, (c) temperature change due to impingement vs. surface temperatures, (d) heat flux due to impingement vs. surface temperatures.

5.3.3 Interdependence of Phase Interface and Heat Transfer Dynamics

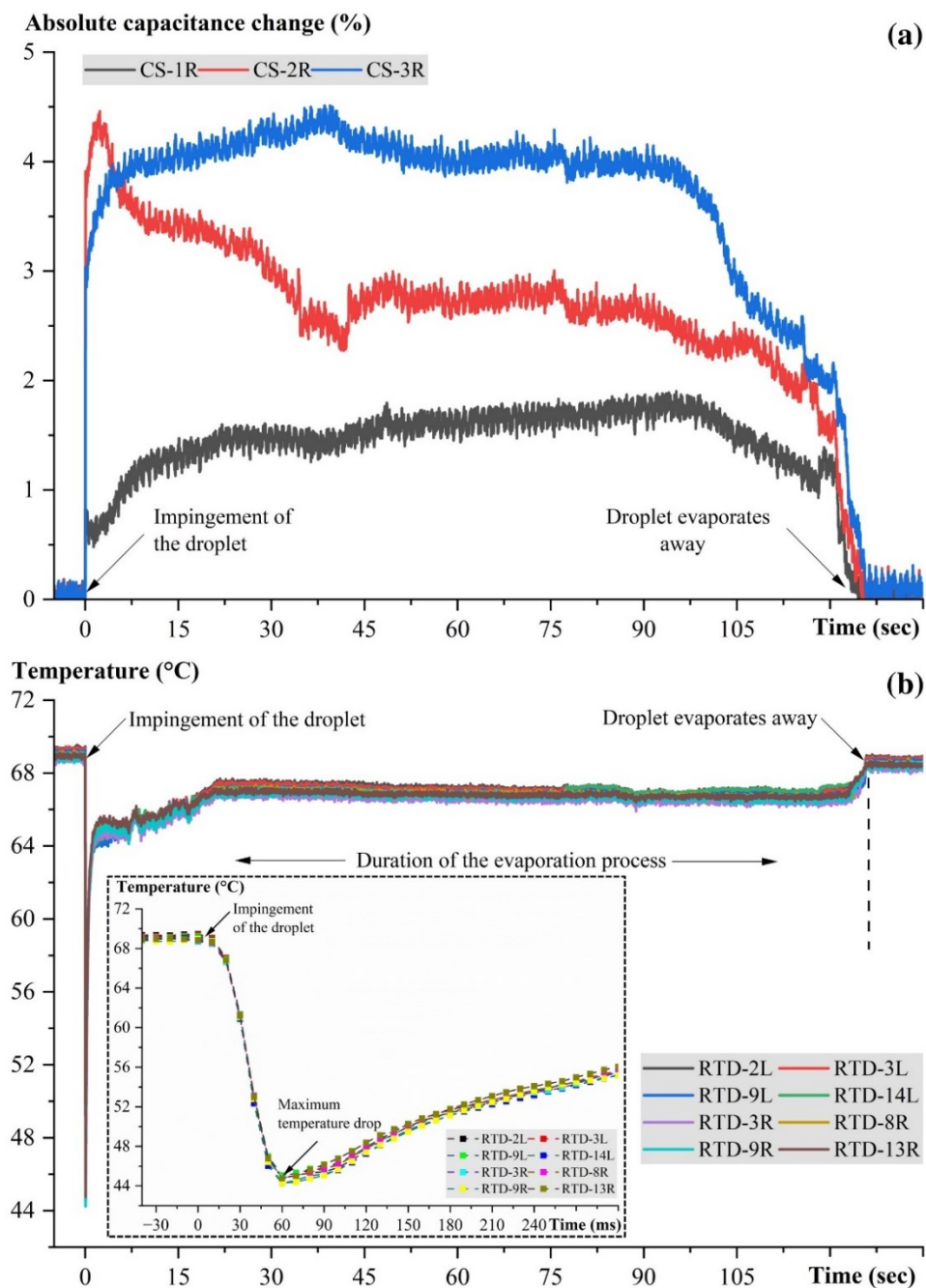


Figure 5-7: Droplet impact and subsequent evaporation of a 6.0 μL water droplet on a heated polyimide surface at 68.8 $^{\circ}\text{C}$ (a) absolute capacitance change (%) with time depicting the passage of MCL, (b) temperature distribution with time (dashed box shows the temperature changes on a millisecond timescale directly preceding and following the moment of droplet impingement).

Additional experiments were conducted to investigate the interdependence of phase interface and heat transfer dynamics for impacting droplets having a volume of $6.0\ \mu\text{L}$ and impact velocity of $1.05\ \text{m/s}$ at varying surface temperatures. This study employed IDE-based capacitance microsensors and RTDs to simultaneously track the MCL and temperature changes caused by droplet impact and subsequent evaporation. Figure 5-7(a) depicts how the capacitance signals change to track the MCL of impacting droplets. Figure 5-7(b) shows the temperature drop upon droplet impact and temperature change during the evaporation process of droplet impacting the heated polyimide surface of the microdevice. The capacitance and temperature data presented were recorded simultaneously and time-aligned with one another for each experiment reported in this work. Figures 5-8 and 5-9 show additional experimental results for droplet impact and subsequent droplet evaporation processes at $80.9\ ^\circ\text{C}$ and $89.5\ ^\circ\text{C}$. In these plots, time “0” second denotes the impingement of the droplet, demonstrated by the capacitance sensors with a sharp and sudden rise in their signals as the droplet covered these sensors upon impact. Near the end of the evaporation process, when the droplet evaporated away, the change in capacitance signals was more gradual and lower in magnitude, differing from the moment of impact. These capacitance sensors can thus precisely detect the key events, such as droplet impact and the moment at which droplets evaporated away via the pattern and magnitude of the signals.

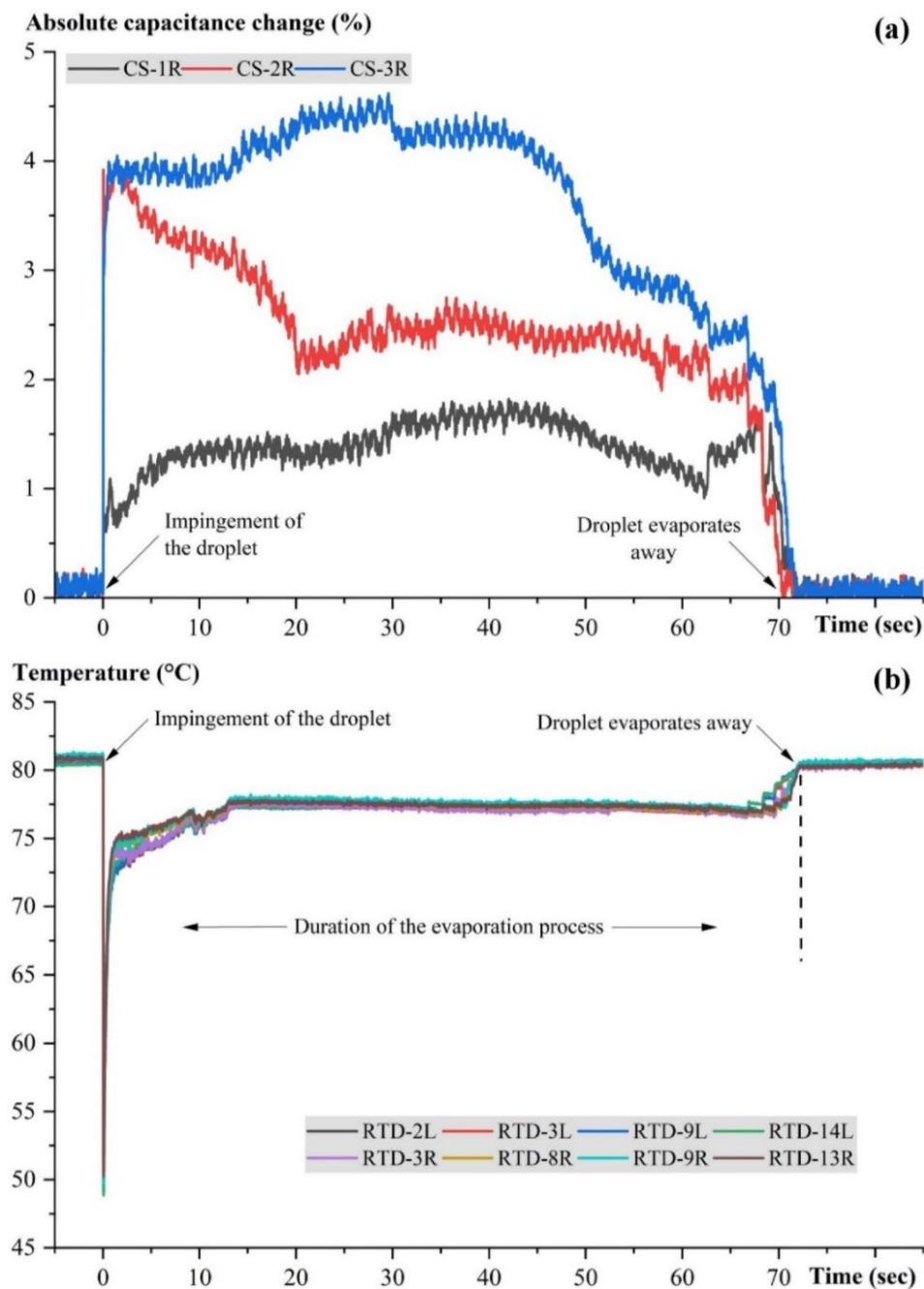


Figure 5-8: Droplet impact and subsequent evaporation of a 6.0 μL water droplet on a heated polyimide surface at 80.9 °C (a) absolute capacitance change (%) with time depicting the passage of MCL, (b) temperature distribution with time.

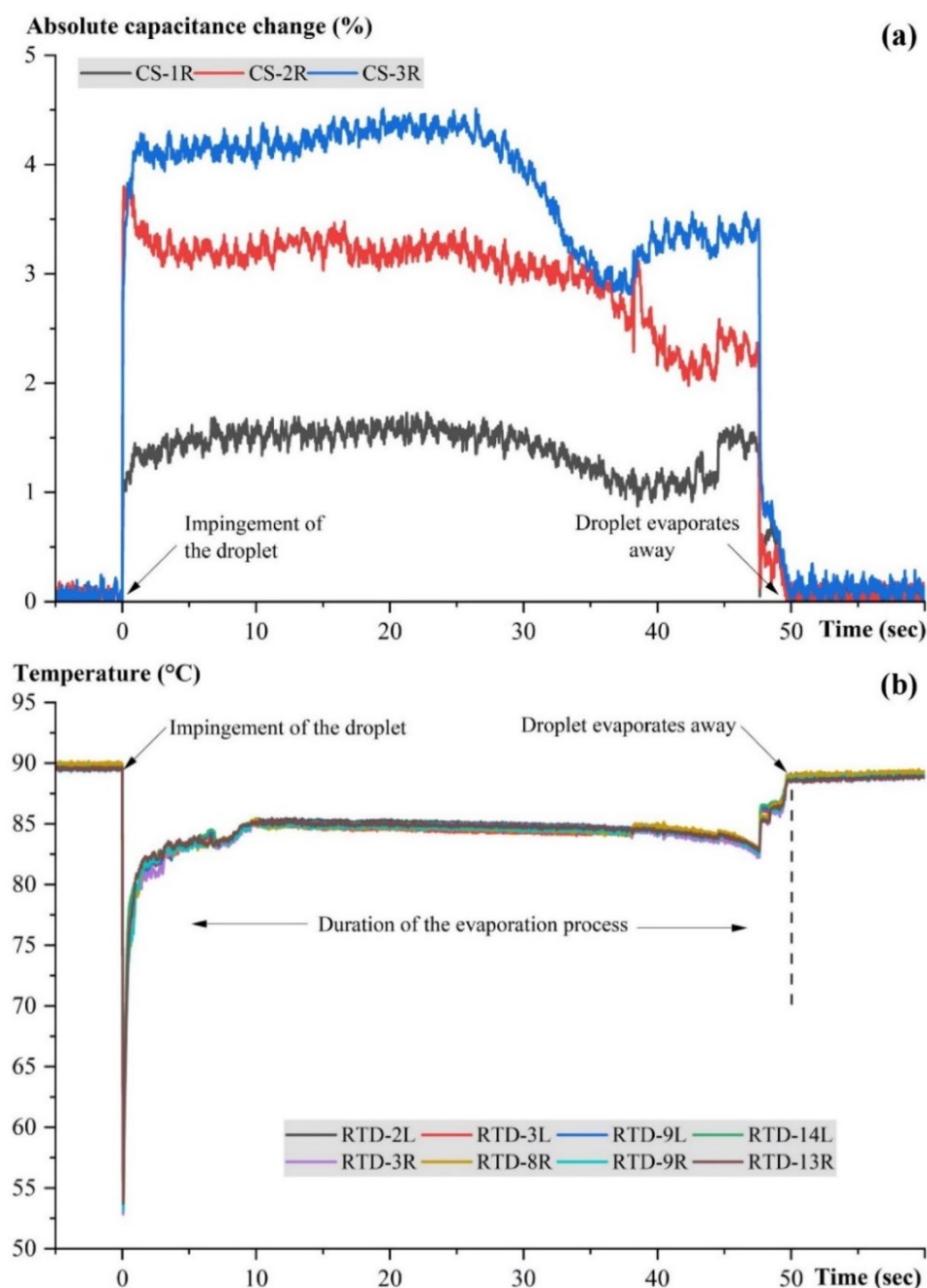


Figure 5-9: Droplet impact and subsequent evaporation of a 6.0 μL water droplet on a heated polyimide surface at 89.5 $^{\circ}\text{C}$ (a) absolute capacitance change (%) with time depicting the passage of MCL, (b) temperature distribution with time.

As depicted by the temperature distribution plots, the RTDs also demonstrated a sharp decrease in temperature at “0” second with the impingement of the droplet, followed

by a gradual increase in temperature and another sharp change at the near end of the experiment, indicating the completion of droplet evaporation. The temperature distribution underneath the evaporating droplet measured by the RTDs is in excellent agreement with the capacitance signals denoting the location of the MCL of the impacting droplets. The duration of the evaporation process measured by the RTDs, and IDE-based capacitance sensors is the same. The absolute capacitance changes and temperature distribution data reported in Figure 5-7 combine to validate the dual functionality of this composite microdevice, where the capacitance sensing scheme enabled precise tracking of the MCL rather than inferring. As the surface temperature increased, the duration of the evaporation process decreased because of the high evaporation rates. The duration of the evaporation process at 68.8 °C was 125.8 s, which was reduced by 42.7% and 60.5% when the surface temperature increased to 80.9 °C and 89.5 °C, respectively. These temperature change plots also revealed that the whole process can be divided into two distinct parts: the first part consists of a sharp temperature drop due to droplet impact followed by a gradual increase in temperature as heat is conducted into the droplet from the heated surface. On the other hand, the second part corresponds to a nearly constant temperature until a sharp change in temperature occurs at the end of the evaporation process. The length of each segment significantly depends on the surface temperature. The duration of the first part increases with increasing surface temperature, while the second segment's length decreases. The latter part of this chapter provides a detailed explanation of the underlying heat transfer mechanisms behind this.

Figure 5-2 shows that the time-elapsd images captured by the high-speed camera exhibited the initial droplet impact, spreading and receding on the millisecond timescale.

However, the temperature drop observed over the first few milliseconds after the droplet impingement did not reveal any additional insights beyond what could be obtained from the longer timescale data. Specifically, the temperature distribution during these initial milliseconds showed a decrease followed by the droplet impingement (see Figure 5-7(b)), consistent with the longer timescale data. As the millisecond data did not provide any further elucidation of the physics governing the evaporation process, this study only emphasized analysis of the temperature distribution over the whole evaporation process, which is on the timescale of seconds.

This study utilized the measured temperature data from the evaporation processes reported above to quantify the heat flux values. Figure 5-10 illustrates the change in vertical heat flux from the resistance heater of the microdevice to the evaporating droplet for evaporation studies performed at 68.8 °C. Figures 5-11 and 5-12 demonstrate the additional heat flux distribution data for evaporation studies conducted at 80.9 °C and 89.5 °C.

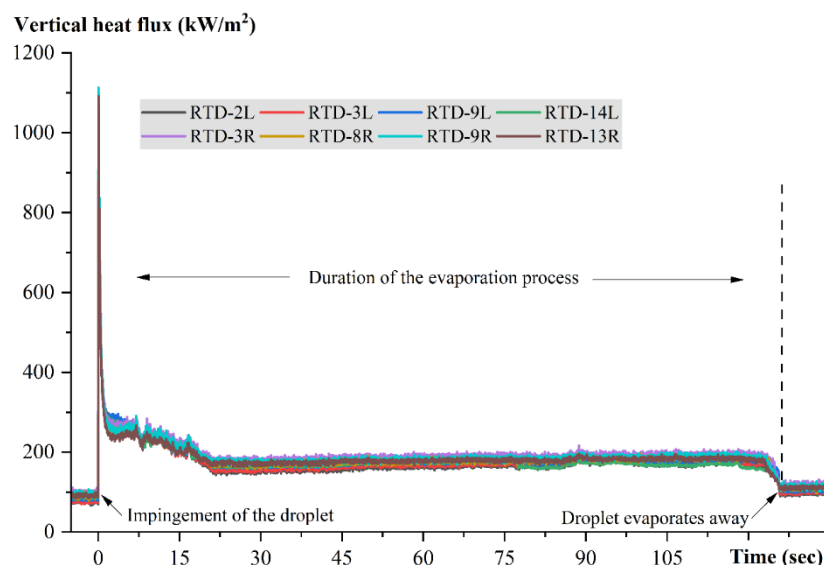


Figure 5-10: Heat flux distribution with time due to droplet impact and subsequent evaporation of a 6.0 μL water droplet on a heated polyimide surface at 68.8 °C.

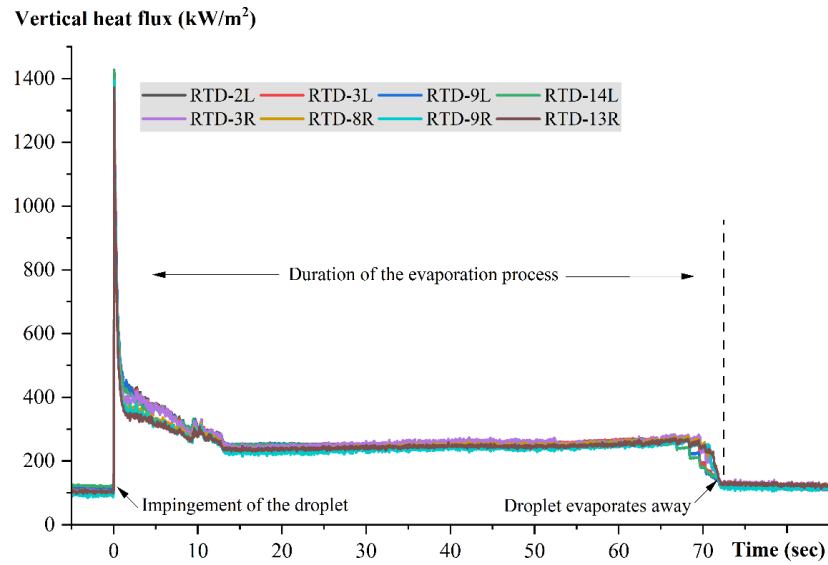


Figure 5-11: Heat flux distribution with time due to droplet impact and subsequent evaporation of a 6.0 μL water droplet on a heated polyimide surface at 80.9 °C.

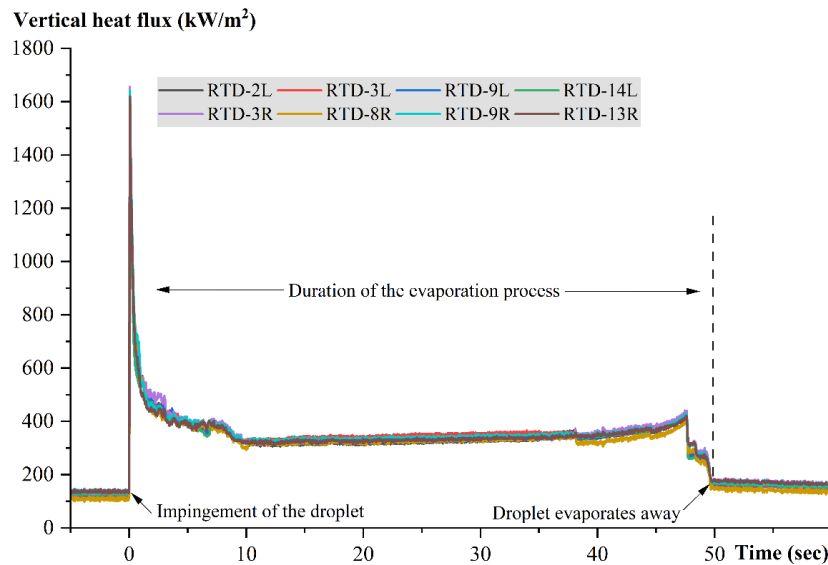


Figure 5-12: Heat flux distribution with time due to droplet impact and subsequent evaporation of a 6.0 μL water droplet on a heated polyimide surface at 89.5 °C.

In these experiments, it was observed that the local heat flux has the maximum values immediately upon the droplet impact resulting from the significant temperature change because of the deformation of the thermal boundary layer between the heated

polyimide surface and the impacting droplets. Another sharp change was observed at the near end of the evaporation process when the droplets evaporated away. These changes denoted the passage of the MCL and the advancing and receding movement due to impingement and evaporation, respectively. As summarized in Table 5-2, the local heat flux values due to droplet impact are, on average, more than 12 times higher than the initial dry state when no water droplet was present on the sensing zone of the microdevice. When the droplets impinged on the heated surface, it facilitated a higher heat flux than the heat flux caused by the receding MCL due to evaporation. The heat fluxes caused by droplet impact are, on average, more than 4.5 times higher than those associated with the receding MCL movement. These data also suggest that higher surface temperatures increase the evaporation rate and the MCL speed, resulting in higher local heat flux values during the receding MCL passage. The previous research found that the average heat flux value for advancing MCL of gently deposited droplets on a heated surface (without droplet impingement) was 5.50-7.45 times the initial dry state for surface temperature ranging from 53.0-69.7 °C [105]. These results indicate that, in the film evaporation regime, droplets impacting a heated surface have approximately 1.6 times higher vertical heat flux values than gently deposited droplets.

Table 5-2 shows that the average heat flux caused by droplet impact (times initial dry state) increased only by 1.74% when the surface temperature rose from 68.8 °C to 89.5 °C. In contrast, the average heat flux caused by receding MCL (times the initial dry state) exhibited a significant increase of 30.77% with the same increase in surface temperature. Based on the results, heat flux caused by droplet impact has a weak dependence on surface temperature; conversely, the receding MCL heat transfer is significantly surface

temperature dependent due to its influence on MCL speed, as shown in the previous chapter.

Table 5-2: Summary of the heat flux values resulting from drop impingement and receding MCL due to evaporation.

Surface temperature	Impact velocity	Average heat flux (initial dry state)	Average heat flux caused by droplet impact (x initial dry state)	Average heat flux caused by receding MCL (x initial dry state)
68.8 °C	1.05 m/s	87.46 kW/m ²	12.09	2.08
80.9 °C		109.72 kW/m ²	12.19	2.27
89.5 °C		127.14 kW/m ²	12.30	2.72

5.3.4 Energy Balance and Thermal Resistance

An energy balance equation can be used to fully understand the contribution of different heat transfer mechanisms on the evaporation of a droplet from a heated surface. After droplet impact/deposition, heat is transferred from the heated surface to the droplet via conduction. The overall heat transfer rate from the heated surface to the droplet can be estimated by:

$$Q_s = h_s A_c (T_s - T_d) \quad \text{Eq. 5-1}$$

Heat transfer also includes the sensible heat required for the temperature increase within the droplet bulk Q_{sen} , the external convective heat transfer from the evaporating droplet to the ambient $Q_{conv/ext}$, radiation heat transfer Q_{rad} , and heat transfer associated with vapor transport during evaporation $Q_{liq/vap}$. The energy balance of an evaporating droplet from a heated surface can be estimated as:

$$Q_s = Q_{sen} + Q_{conv/ext} + Q_{rad} + Q_{liq/vap} \quad \text{Eq. 5-2}$$

In the initial period when the droplet impacts on the heated surface, sensible heat is significant, and the time scale for heat conduction into the droplet can be estimated by [109]:

$$t_{cond} = \frac{r_d^2 \rho_w C_w}{k_w} \quad \text{Eq. 5-3}$$

The estimated time scale for heat conduction is 16.86 s, similar to the period that exhibits the gradual decrease in heat transfer rate values, as shown in Figure 5-13, showed as the sensible heat regime. During the initial evaporation phase, the sharp increase in heat transfer rate upon droplet impact denotes the highest temperature difference between the droplet and the heated surface. After that, the gradual decrease in heat transfer rate indicates an increase in the temperature of the droplet as heat is being conducted to the droplet from the heated surface until surface evaporation dominates the process and causes relatively constant heat transfer rate. The assumptions for the analytical model presented in Eq. 5-3 for the time scale of heat conduction are based on:

- The thermal properties of the liquid, such as density, specific heat capacity, and thermal conductivity, are assumed to be constant.
- The effects of convection and phase change are neglected in the initial sensible heat transfer regime, focusing on the conduction heat transfer within the droplet from the heated surface of the microdevice.
- The droplet maintains a spherical shape with a radius r_d throughout the initial heat conduction period.

After this initial heating, the conductive heat transfer process achieves a quasi-steady state, and the heat transfer associated with mass transfer due to vapor removal becomes dominant. Due to the high efficiency of phase-change heat transfer, the heat

transfer associated with vapor removal or evaporation accounts for more than 95% of the overall heat transfer, making other modes of heat transfer negligible [109], [110].

Therefore, the energy balance of an evaporating droplet can be approximated as:

$$Q_s \approx Q_{liq/vap} \quad \text{Eq. 5-4}$$

The variation in heat transfer rate at the liquid-vapor interface can be calculated by employing the equation below that expresses $Q_{liq/vap}$ in terms of the change in volume with time. Figure 5-14 shows the change in volume with time recorded by the DSA for the experiment conducted at 80.9 °C. These recorded values facilitated the calculation of the heat transfer rate values at the liquid-vapor interface throughout the evaporation process, also displayed in Figure 5-14.

$$Q_{liq/vap} = \rho_w h_{fg} \frac{dV}{dt} \quad \text{Eq. 5-5}$$

The assumptions for the analytical model presented in Eq. 5-5 for the heat transfer rate at the liquid-vapor interface are based on:

- The liquid is a pure substance with constant thermophysical properties, such as density and latent heat of vaporization.
- The effects of the external convective heat transfer from the evaporating droplet to the ambient and radiative heat transfer are negligible.
- Heat conduction into the droplet becomes quasi-steady, and heat transfer at the liquid-vapor interface is dominated by the latent heat of vaporization.

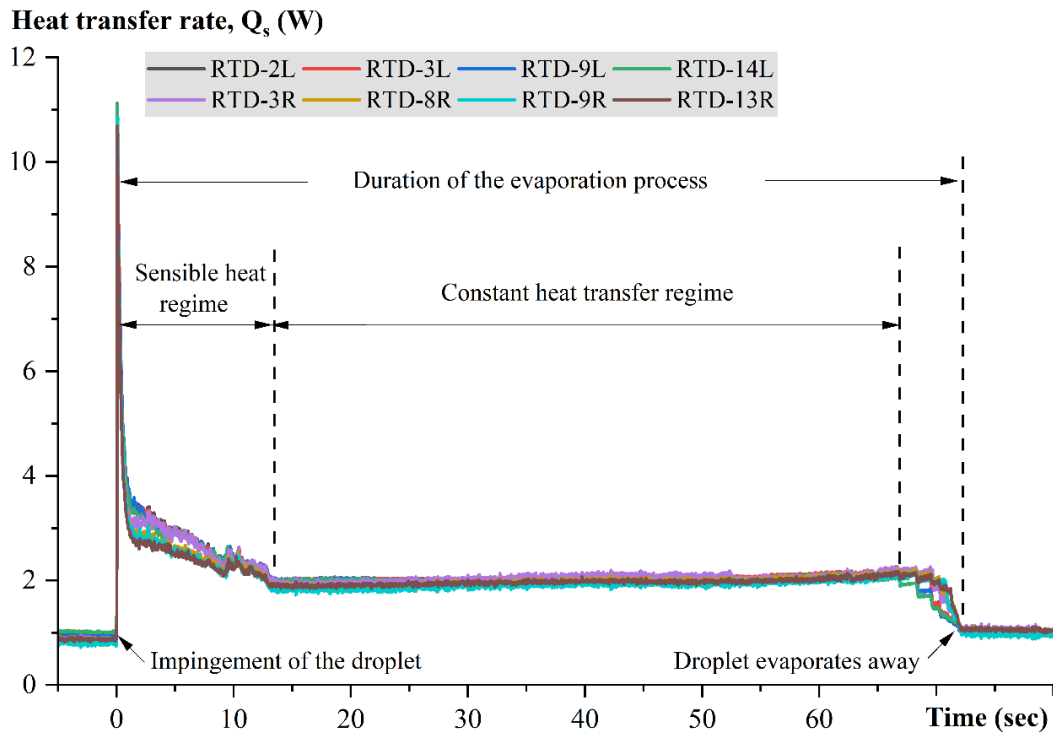


Figure 5-13: Heat transfer rate distribution with time at the solid-liquid interface due to droplet impact and subsequent evaporation of a 6.0 μL water droplet on a heated polyimide surface at 80.9 $^{\circ}\text{C}$ as measured by the microscale RTDs.

Based on the RTD-measured temperature distributions, the calculated average heat transfer rate Q_s was 1.99 W during the sessile droplet evaporation phase for the experiment conducted at 80.9 $^{\circ}\text{C}$ (see Figure 5-13). The average heat transfer rate for vapor removal $Q_{liq/vap}$ was calculated as 1.84 W (see Figure 5-14) using the DSA-recorded change in volume of the evaporating droplet from the same experiment. The percentage difference between these values is 7.54%, within the range of estimated propagated error of 11% resulting from the temperature difference measurement uncertainty of ± 0.5 $^{\circ}\text{C}$ [105].

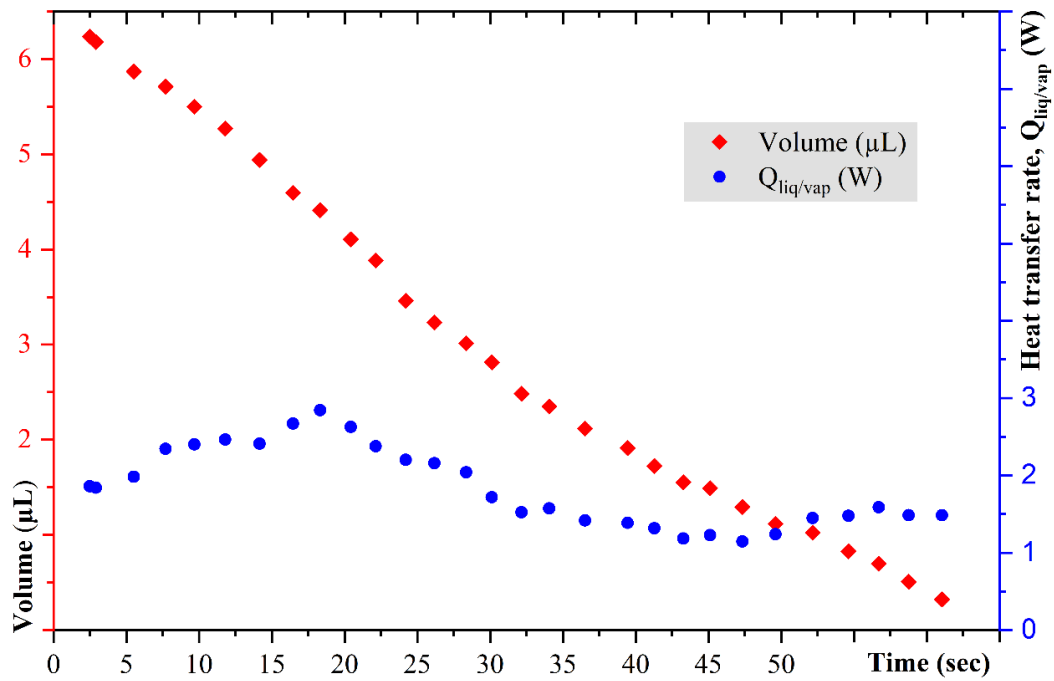


Figure 5-14: Change in volume and heat transfer rate at the liquid-vapor interface over time due to evaporation of a 6.0 μL water droplet on a heated polyimide surface at 80.9 $^{\circ}\text{C}$.

A thermal resistance model can also be employed to determine an evaporating droplet's overall heat transfer mechanism. The total thermal resistance can be estimated by:

$$R_{tot} = R_{drop,cond} + R_{liq/vap} + R_{conv/ext} + R_{rad} \approx \frac{\delta}{k_w A_c} + \frac{1}{h_{liq/vap} A_s} \quad \text{Eq. 5-6}$$

Where $R_{drop,cond}$ denotes the thermal conductive resistance within the droplet, and $R_{liq/vap}$ is the interfacial resistance associated with the mass transfer at the liquid-vapor interface. Since small-scale evaporating droplets experience minor heat loss via radiation and external natural convection to the surroundings, the radiative R_{rad} and external convective resistances $R_{conv/ext}$ contribute negligibly [109], [110]. As the droplet evaporates, the thickness of the droplet δ decreases, as does the resistance within the liquid. So, after the initial heat-up period, the resistance associated with vapor removal dominates

over the resistance within the liquid [106]; hence the total thermal resistance can be approximated as:

$$R_{tot} \approx R_{liq/vap} \approx \frac{1}{h_{liq/vap} A_s} \quad \text{Eq. 5-7}$$

During the experiment conducted at 80.9 °C, the calculated total thermal resistance was 28.6 °C/W. This calculation was based on the average heat transfer rate at the solid-liquid interface obtained from the RTD-measured temperature distributions during the evaporation study. The calculated thermal resistance associated with vapor removal was 30.9 °C/W. The percentage difference between these was 7.54%, which falls within the range of estimated propagated error.

5.3.5 Contribution of Convection within Droplet

This study evaluated the contribution of convection within the droplet to the overall heat transfer by considering the effects of buoyancy and thermocapillary flows inside the impacted droplets. Grahshoff (Gr) and Marangoni (Ma) numbers are the two dimensionless numbers widely used to characterize the buoyancy and thermocapillary-driven convections within droplets. A higher Gr number indicates that buoyancy-driven convection is the more dominant mode of heat transfer, whereas a lower Gr suggests weaker buoyancy and conduction-dominated heat transfer [32]. The range of Gr number values for this experiment is 3.63-5.31, much lower than the reference value (Gr is <2400) [111], indicating the contribution of buoyancy-driven convection is negligible. Ma number characterizes thermocapillary-driven convection in evaporating droplets by comparing the surface tension gradient caused by temperature gradient to viscous force. The contribution of thermocapillary flows, known as the Marangoni convection, increases with increasing Ma number. The effect of Marangoni convection is negligible for horizontal liquid films

if the Ma number is less than 80-100 [111]. With a characteristic length of 0.318 mm, experiments from this work yield Ma values in the range of 16500-24250, higher than the reference value (80-100), denoting the contribution of thermo-capillary convection within the droplet. Another dimensionless number, the Bond (Bo) number, characterizes the relative contribution between buoyancy convection and Ma convection in an evaporating droplet. The calculated value of Bo is 0.00138 for the experiments reported in this work, and when $Bo \ll 1$ [111], internal flow is dominated by Ma convection. During the process, when evaporation is in constant contact diameter (CCD) mode, the evaporative mass loss near the contact line must be balanced by new liquid flowing from the droplet's bulk [48]. Therefore, a capillary flow can exist within an evaporating sessile droplet, although it is not significant due to the high efficiency of the phase-change heat transfer. Heat transfer associated with the surface evaporation of an evaporating droplet accounts for more than 95% of the overall heat transfer [109], [110], making other modes of heat transfer negligible. Moreover, in experiments of this work, the CCD mode constituted only about 27% of the total duration of the evaporation process, as demonstrated in Figure 5-4. Therefore, the contribution of internal convection in small-scale evaporating droplets is often neglected in the literature. Gholijani et al. [89] and Lee et al. [106] found that the total heat is mainly transferred through diffusion or surface evaporation during the sessile droplet evaporation phase of impacting droplets onto a heated solid wall. Chandramohan et al. [112] also reported that the convection within evaporating droplets has a negligible contribution to wetting droplets due to their low height-to-contact diameter ratio.

5.3.6 Calculation of the Dimensionless Parameters

This study employed the Weber (We) number to characterize the droplet spreading behavior upon impact on the heated polyimide surface of the microdevice. We number is a dimensionless parameter that refers to the ratio of inertial to surface tension forces acting on a fluid flow [89]. It plays an essential role in determining the outcome of the droplet impact; higher impact velocity results in a higher We number. At higher We numbers, the inertial forces dominate over surface tension forces, leading to greater droplets spreading upon impact. Based on the impact velocity range of 0.58 to 1.35 m/s, the following equation denotes the range of We numbers for this study.

$$We = \frac{\rho_w Du^2}{\sigma} = [11.2, 60.7] \quad \text{Eq. 5-1}$$

This study utilized Grahshoff (Gr) and Marangoni (Ma) numbers to characterize the buoyancy and thermocapillary-driven convections within droplets. Gr number refers to the ratio of buoyancy force to viscous resistance. A higher Gr value indicates that buoyancy-driven convection is the more dominant mode of heat transfer, whereas a lower Gr suggests weaker buoyancy and conduction-dominated heat transfer [48]. The range of Gr number values for our experiment is 3.63-5.31, much lower than the reference value (Gr is <2400) [111], indicating the contribution of buoyancy-driven convection is negligible.

$$L = \frac{V}{\pi R^2} \approx 3.18 \times 10^{-4} \text{ m} \quad \text{Eq. 5-2}$$

$$Gr = \frac{g \beta \Delta T L^3}{\nu^2} = [3.63, 5.31] \quad \text{Eq. 5-3}$$

The contribution of Marangoni convection (thermocapillary flow) during droplet evaporation heat transfer can be quantified by employing the Ma number, which is a ratio

of surface tension gradient caused by the temperature gradient to the viscous force. The contribution of Marangoni convection increases with increasing Ma number [111]. The contribution of Marangoni convection is negligible for liquid droplets if the Ma number is less than 80–100 [113]. With a characteristic length of 0.318 mm, our experiments yield Ma values in the range of 16500–24250, higher than the reference value, denoting the contribution of thermo-capillary convection within the droplet is more significant than the buoyancy-driven convection.

$$Ma = \frac{\frac{d\sigma}{dT} \Delta T L}{\mu a} = [16585.77, 24249.28] \quad \text{Eq. 5-4}$$

$$Bo = \frac{g \beta \rho L^2}{\frac{d\sigma}{dT}} = 0.00138 \quad \text{Eq. 5-5}$$

The Bond (Bo) number, the ratio of buoyancy force to surface tension force, characterizes the relative contribution between buoyancy convection and Ma convection in an evaporating droplet. The calculated value of Bo is 0.00138 for the experiments reported in this work, and when $Bo \ll 1$ [111], internal flow is dominated by Ma convection. Please refer to the table of *Nomenclature* provided in Table 5-1 for the details and units of the symbols used in the equations of these dimensionless parameters.

5.3.7 Key Findings

Droplet impingement on a heated surface and subsequent evaporation can be divided into two segments based on the effective heat transfer rate, as shown in Figure 5-13. The first segment, “sensible heat regime,” corresponds to the sharp increase in heat transfer rate upon droplet impact resulting from the highest temperature difference between the droplet and the heated surface. After that, the gradual decrease in heat transfer rate

indicates an increase in the temperature of the droplet as heat is being conducted to the droplet from the heated surface. After this initial heating, in the second segment, the conductive heat transfer process achieves a quasi-steady state, and the heat transfer associated with mass transfer due to vapor removal becomes dominant and causes a nearly constant heat transfer rate. Microscopically, the previous research closest to ours is the microscale heaters array-based investigation of heat transfer characteristics of a single isolated impacting droplet on a heated surface by Lee et al. [106]. They likewise reported two distinct segments throughout the droplet vaporization process regarding effective heat transfer rate at the solid-liquid interface. According to them, for superheated impacting droplets, the first segment is mainly caused by the oscillatory motion of the droplet after impact and initial heat conduction into the droplet. This study observed that for subcooled impacting droplets, the initial oscillations into the droplets lasted only a few tens of milliseconds, whereas the duration of the first segment was a few seconds, denoting the effect of oscillatory motion is negligible; hence, heat conduction into the droplet from the heated surface entirely dominated this segment.

This study indicates that the surface temperature significantly influences the length of these two segments. In the case of subcooled impinging droplets, In the case of subcooled impinging droplets, the sensible heat regime's duration increases as the surface temperature increases. However, the duration of the constant heat transfer segment decreases with the rise in surface temperature. The duration of the conduction-dominated first segment increased from 16% to 20% of the total time of the process when the surface temperature increased from 68.8 °C to 89.5 °C. Meanwhile, the duration of the evaporation-dominated second segment decreased from 81% to 75%. This study also

facilitates a comparison of the magnitude of the heat transfer rate of both segments, where the sensible heat segment has higher heat transfer rates than the segment dominated by vapor removal/surface evaporation.

The distinct heat transfer regimes during droplet impingement and subsequent evaporation reported in this study can reveal essential insights into the underlying physics. Understanding the transition from initial heat conduction to quasi-steady surface evaporation and associated effective heat transfer rate can facilitate more accurate models for phase-change heat transfer processes.

The simultaneous microscale temperature measurements and phase interface sensing of the custom-made MEMS device utilized in this study make it possible to identify the dominant heat transfer mechanisms during droplet impact and evaporation. In terms of detecting the MCL's location, most previous works relied on a combination of high-speed optical imaging and post-processing of the IR images; these works often inferred MCL as the coinciding region with the local temperature minimum and high heat flux values. These techniques' macroscopic spatial resolution and visibility, i.e., line of sight and viewing angle, often hinder precise detection of the location and temperature gradient in the MCL region. In this work, the IDE sensors facilitated independent and microscale tracking of the MCL validated by the temperature measurement of the RTDs, facilitating an important distinction and utility. The resistance and capacitance-based operating principles of this microdevice offer a significant utility in detecting temperature changes and tracking MCL at the microscale in real-time, even for applications with limited or no visibility. This MEMS device eliminates the need for an external heater or optical image processing scheme, making it an independent experimental setup for investigating phase-change heat

transfer processes and usable within thermal management hardware or processing equipment.

5.4 Summary of Findings

This study investigated droplet impact and subsequent evaporation of subcooled impinging droplets on a heated polyimide surface at varying impact velocities and surface temperatures utilizing a custom MEMS device to determine the underlying physics behind the phase-change heat transfer process. This microdevice ensured simultaneous tracking of the MCL validated by the microscale temperature measurement of the RTDs, facilitating an independent experimental setup. Experimental results have shown that when a droplet impacts a heated surface and evaporates, the process can be divided into two segments based on the effective heat transfer rate: an initial conduction-dominated segment followed by another segment dominated by surface evaporation. The experimental investigations have also led to the following conclusions:

- The first segment, “sensible heat regime,” corresponds to a sharp increase in heat transfer rate upon droplet impact, followed by the gradual decrease in heat transfer rate resulting from an increase in the temperature of the droplet as heat is being conducted to the droplet from the heated surface.
- The effect of oscillatory motion is negligible for subcooled impacting droplets, unlike in a superheated regime; hence, heat conduction into the droplet from the heated surface entirely dominates the first segment.
- In the second segment, the conductive heat transfer process achieves a quasi-steady state, and the heat transfer associated with mass transfer due to vapor removal becomes dominant and causes a nearly constant heat transfer rate.

- Increasing surface temperature lengthens the duration of the sensible heat regime but shortens the length of the constant heat transfer segment.
- The sensible heat regime has higher heat transfer rates than the segment dominated by vapor removal/surface evaporation.
- Heat flux caused by droplet impact has a weaker dependence on surface temperature; conversely, the receding MCL heat transfer is significantly surface temperature dependent.
- The heat flux at the solid-liquid interface of an impacting droplet increases with the rise of either impact velocity or surface temperature.
- The local heat flux values due to droplet impact are, on average, more than 12 times higher than the initial dry state and more than 4.5 times higher than those associated with the receding MCL movement.
- In the film evaporation regime, droplets impacting a heated surface have approximately 1.6 times higher vertical heat flux values than gently deposited droplets.
- Buoyancy and thermocapillary convection within evaporating droplets contribute negligibly to overall heat transfer, which is dominated by heat conduction into the droplet and surface evaporation.

In summary, the experimental results of this work from studying the heat transfer regimes and comprehending the transition from conductive heat transfer to surface evaporation during droplet impingement and following evaporation can provide essential insights into underlying physics to improve heat transfer models, surface engineering, and overall effectiveness. Additionally, real-time, minimally invasive temperature

measurements and simultaneous tracking of MCL at the microscale by a composite microdevice utilized in this work can aid in thermal management and process control for electronics cooling.

In terms of future application, this multifaceted sensing scheme can be employed to investigate droplet impingement and subsequent evaporation across nucleate boiling, transition boiling, and film boiling regimes. Heat transfer resulting from various droplet-surface interactions can also be investigated with this MEMS device by enabling surface modification of the top polymer layer. Furthermore, this device can be utilized to investigate successive droplet and drop-on-drop impingement events, which closely emulate real-world spray cooling techniques.

CHAPTER 6

INVESTIGATION OF HEAT TRANSFER MECHANISMS AND THREE-PHASE CONTACT LINE BEHAVIOR OF NUCLEATED BUBBLES IN POOL BOILING WITH COMPOSITE MEMS DEVICE

6.1 Introduction and Motivation

Pool boiling is considered one of the most effective methods of heat transfer, which makes it applicable in a wide range of applications ranging from nuclear reactors to small-scale heat sinks. Boiling processes have been the focus of significant scientific research over the past few decades because of its importance in a wide variety of scientific and technological applications [114]–[118]. Boiling heat transfer is also considered as one of the most effective means of achieving high rates of heat dissipation due to its superiority as compared with the single-phase heat transfer processes [57], [118]–[121]. Efficient cooling technologies are essential for high heat flux surfaces of nuclear reactors, high-power LEDs, aircraft combustion chambers, and super-critical boilers, which motivated the experimental investigation of micro-structured surfaces in pool boiling processes [119]. Surfaces with micro-structures have demonstrated superior performance in reducing the maximum superheat and enhancing the boiling heat transfer and critical heat flux. The implementation of micro-pin-fin configurations, deposited nanoparticles, and electrodeposited nanostructured porous media on the heat flux surfaces has led towards enhanced heat dissipation techniques for high heat flux surfaces [119], [122], [123].

Despite its ubiquity and long history of study, nucleate boiling is a complex phenomenon with many aspects still not fully understood. Even simplistic boiling processes are comprised of multiple fundamental heat transfer phenomena such as transient heat conduction, micro-convection, and micro-layer evaporation which are also closely interrelated [124]. Although the bubble nucleation at the surface enhances the heat dissipation in pool boiling processes, the microscale heat transfer phenomena involved at the nucleation site are still indistinct because of the complex correlation among the hydrodynamics, mass, momentum, and energy transport during bubble nucleation [125]. Conventional macroscopic measurement techniques cannot precisely measure these fundamental heat transfer phenomena because of the required small temporal and spatial resolutions [126]. Development of high-resolution microscopic measurement techniques such as MEMS sensors that contain an artificial nucleation site, temperature, and heat flux sensors has led towards new observations of heat transfer mechanisms involved at the nucleation site of pool boiling processes [114], [126]. A MEMS device containing a micro-heater array with a spatial resolution of 100 μm has facilitated the observation that transient conduction and micro-convection have been the principal heat transfer phenomena during pool boiling of FC-72 [124]. A few other MEMS devices comprising thin film thermocouples and resistance temperature detectors with a spatial resolution of 22–40 μm has determined micro-layer evaporation as one of other dominant heat transfer mechanisms involved at the nucleation site for pool boiling processes [125], [126].

Although the MEMS sensor approaches previously described have facilitated the observation of fundamental microscopic heat transfer phenomena involved at the nucleation site of pool boiling processes, there remain significant limitations and scope for

improvement to overcome the shortcomings associated with the spatial and temporal resolutions as well as the reliance on thermal data alone to infer phase behavior rather than observe it directly. The acquisition of thermal data alone does not facilitate the comprehensive understanding of the mechanisms involved at the MCL region, and thus needs to be combined with some other form of independent sensing of the dynamic phase interface behavior. A capacitance-based phase interface sensing device mounted on top of the temperature sensing MEMS sensor can enable a new understanding regarding the mechanistic interrelationship among the phase interface dynamics and the heat transfer mechanisms involved in the bubble ebullition cycle. Another demanding research need is to unlock the interdependence of underlying heat transfer mechanisms and MCL behavior for various working fluids and thermo-physical properties as they significantly influence each other.

This project addressed the research needs by implementing the custom-made MEMS device with an artificial nucleation site that made it applicable for nucleating bubbles and investigating the heat transfer and interfacial phenomena. This device measured individual nucleated bubbles' temperature and heat flux at sufficiently high spatial and temporal resolutions to determine the correlation with the phase interface behavior.

6.2 Methodology

6.2.1 Microdevice Overview

The proposed research requires a multi-functional MEMS device comprising a thin-film resistance heater, a series of RTDs, and an array of phase interface sensing capacitance micro-sensors. Thin-film thermocouple (TFTC) based MEMS devices can also provide

thermal data, but RTDs outperform TFTCs in terms of stability, precision, and repeatability.

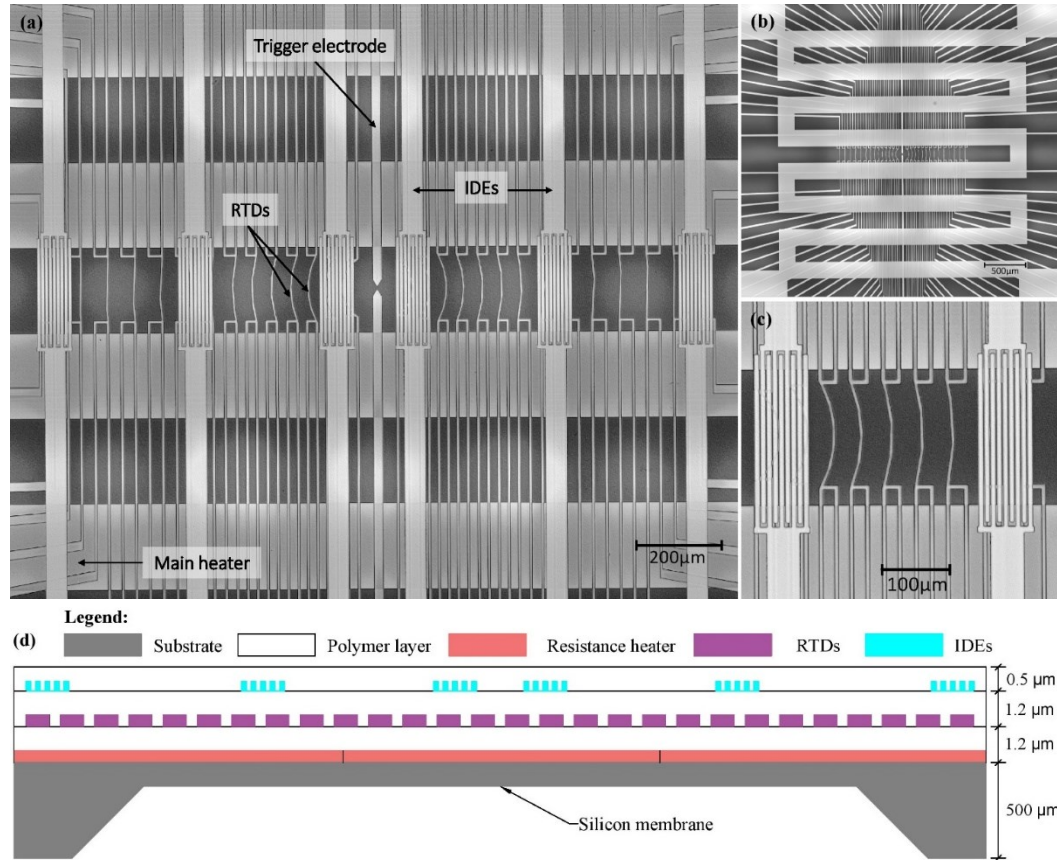


Figure 6-1: Laser microscope images of the microdevice. (a) A detail of the sensing zone containing six IDE capacitance micro-sensors, a series of four-probe type RTDs, two hydrolysis trigger electrodes, and a resistance heater. (b) Thin-film resistance heater (serpentine feature) located beneath RTD and IDE layers. (c) A close-up of the sensing region showing detailed view of the IDEs and RTDs. (d) Schematic diagram of the cross-section of the microdevice. Conceptual image, not to scale.

Figure 6-1(a)-(c) shows the laser microscope images of the microdevice based on silicon substrate for studying nucleate boiling processes. Figure 6-1(d) shows a schematic diagram of the cross-sectional view of the microdevice, where the resistance heater resides on the primary insulation layer (silicon nitride) on top of a silicon membrane. The secondary insulation layer (polyimide) resides between the resistance heater and the RTDs

to provide electrical insulation between them. A series of RTDs is spatially oriented from the center of the device on the second insulation layer to record temperatures for individual nucleated bubbles at various radial locations. A capacitance-based phase interface sensor array is mounted on top of the third insulation layer (polyimide) to measure the moving contact line behavior during the bubble ebullition cycle. Another 500 nm polymer layer was deposited on top of the capacitance sensor layer as the topmost protective coating of the microdevice. Finally, a rectangular etch pit was fabricated at the center of the microdevice by selectively etching the top polymer layer. As shown in Figure 6-2, this $20\ \mu\text{m} \times 20\ \mu\text{m}$ etch pit acted as the artificial nucleation cavity during each experiment reported in this work. Please refer to Chapter 4 for more details on the working mechanism of the RTDs and IDEs employed in this microdevice.

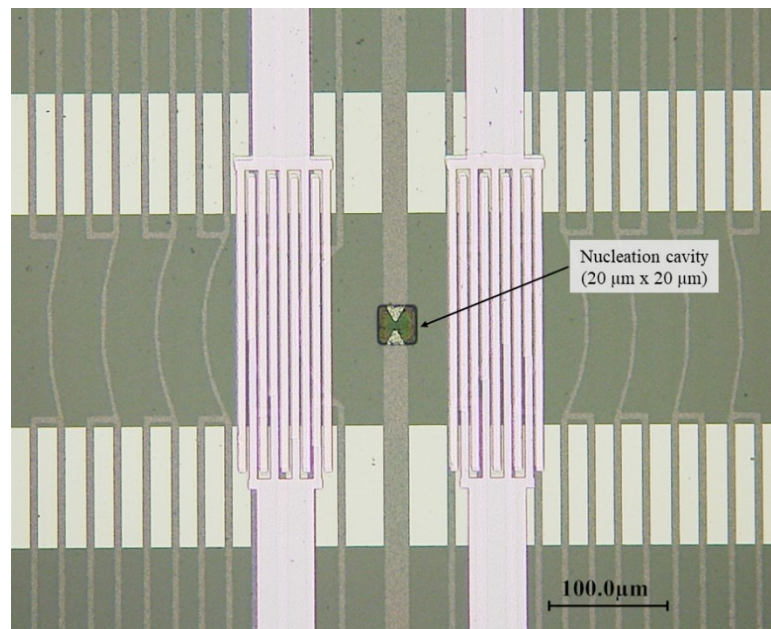


Figure 6-2: Laser microscopic image of the nucleation cavity at the center of the device, fabricated by RIE etching of the polyimide layer.

6.2.2 Experimental Setup

The experimental setup for pool boiling and the microdevice to be tested is shown in Figure 6-3. The test device and ceramic chip carrier combo are connected to a ZIF socket, which is then placed inside a cylindrical enclosure. The cylindrical enclosure, machined out of MDS-filled cast nylon, was designed to expose only the sensing zone of the microdevice with the DI water inside the borosilicate glass chamber while keeping the circuits and other setups away from the water, as shown in Figure 6-3. Figure 6-4 shows a detailed 3D model of the cylindrical enclosure that holds the microdevice and connecting wires inside. A nichrome heater wire mounted outside the glass chamber provided necessary heating on the DI water inside for the experiment. A programmable temperature controller (PTC 10, Stanford Research Systems) controlled the heater wire's power input and maintained the temperature to a set point by monitoring the temperature inside with a commercially available thermocouple (Type-K, Omega Engineering) placed inside the glass chamber. A DC power supply provided the necessary power to the resistance heater of the test device to facilitate bubble nucleation from the sensing zone of the microdevice. Another DC power supply provided a small amount of input current (< 1 mA) to the power leads of the four probe RTDs of the microdevice. The voltage leads of the RTDs and capacitance microsensor array were connected to a computer-controlled data acquisition (DAQ) system. During the investigation, the DAQ system controlled the data acquisition of the thermal and capacitance sensors.

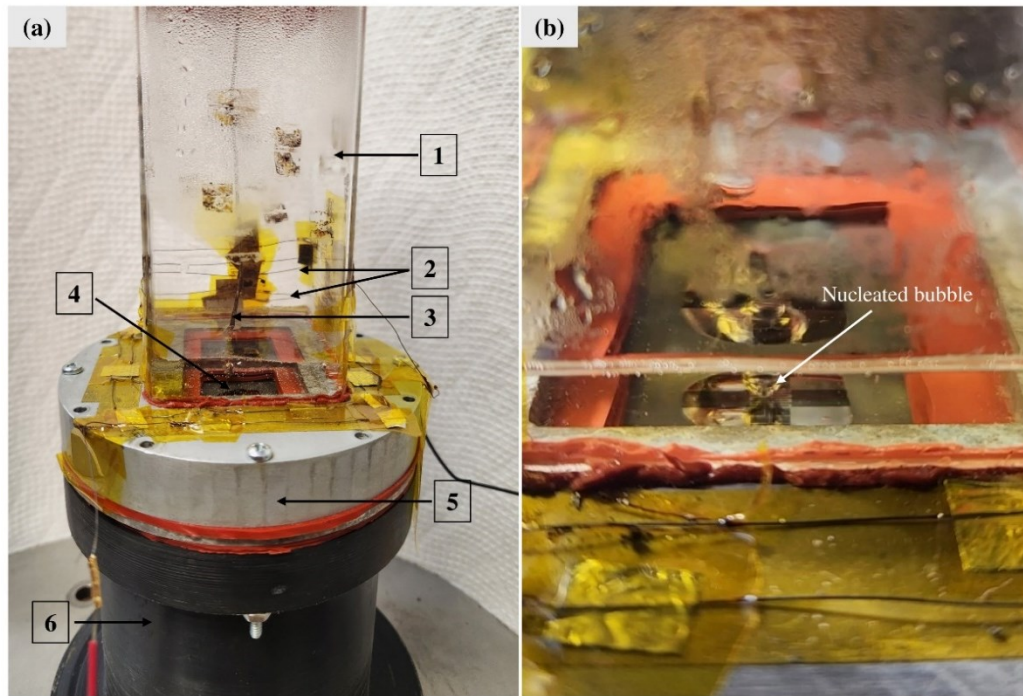


Figure 6-3: (a) Pool boiling experimental setup consisting of 1: Borosilicate glass chamber, 2: Nichrome wire heater, 3: Thermocouple, 4: MEMS device, 5: Aluminum top plate, 6: Cylindrical enclosure machined out of MDS-filled cast nylon to hold the microdevice in inside the boiling test rig. (b) A nucleated bubble at the onset of departure from the center of the device.

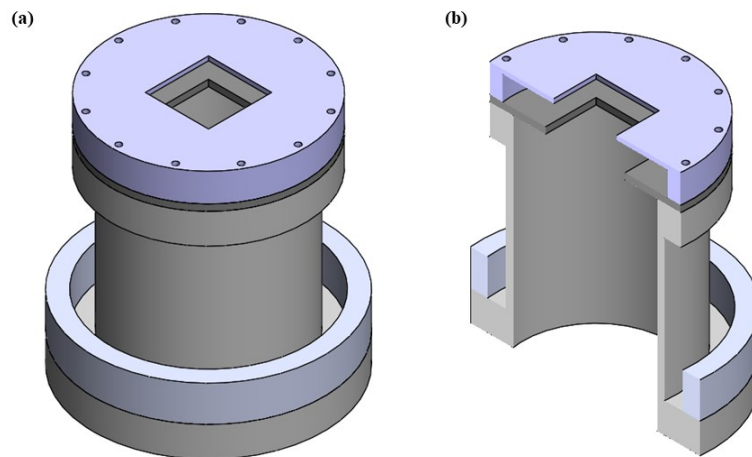


Figure 6-4: A 3D model of the cylindrical enclosure machined out of MDS-filled cast nylon to hold the microdevice and connecting wires inside: (a) isometric view, (b) sectional view.

6.3 Results and Discussion

Figure 6-5 shows the results of a typical experiment conducted to investigate nucleated bubbles in the pool boiling rig described in the previous section. During this experiment, the water temperature inside the rig was maintained at 98 °C using the nichrome heater wire controlled by the PTC 10 temperature controller. A heater power of 2659.3 to 3551.1 mW was applied to the resistance heater of the microdevice to nucleate bubbles from the artificial nucleation cavity of the microdevice.

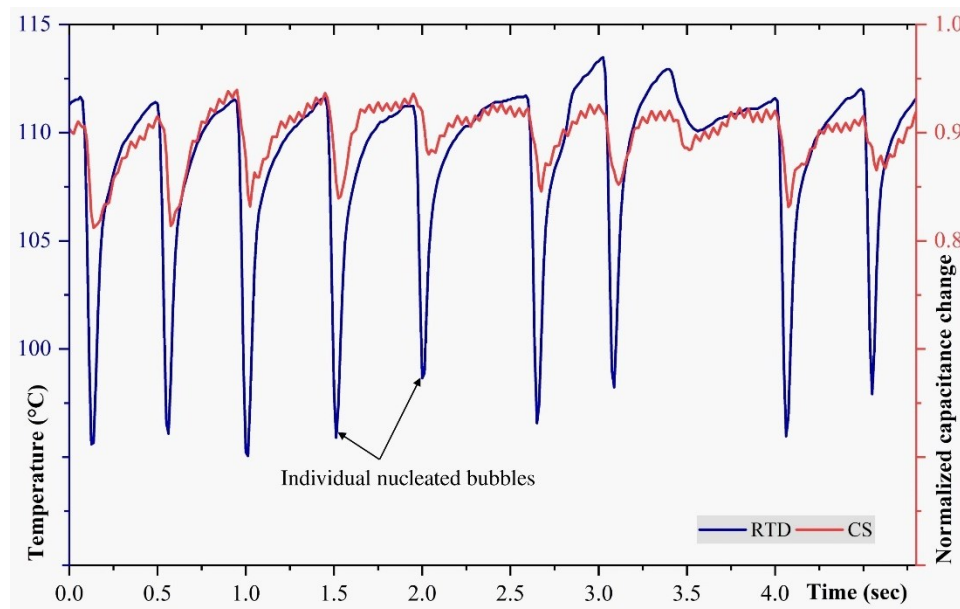


Figure 6-5: Test results at a surface temperature of 111.5 °C show the MCL passage and surface temperature variation for a few bubbling events.

Figure 6-5 demonstrates the change in temperature throughout the bubble ebullition cycle, starting from the nucleation to departure for individual nucleated bubbles. This figure also shows the change in capacitance signal resulting from the movement of the MCL during the bubble cycle. The measured temperature & capacitance changes

throughout this experiment confirmed each other's accuracy, thereby validating the dual functionality of the MEMS device utilized in this study.

Figures 6-6 and 6-7 show the events that occur throughout the bubble ebullition cycle in terms of heat transfer and hydrodynamic perspective. Based on the experimental results depicted in these figures, the nucleation of the bubble was preceded by the rewetting of the sensing zone, which caused a sharp decrease in surface temperature till the onset of bubble nucleation. An experiment at a surface temperature of 111.5 °C, shown in Figure 6-6, took, on average, 75 ms from rewetting to bubble nucleation. For another experiment at a higher surface temperature of 115.4 °C, the duration of rewetting to the onset of bubble growth was 62.5 ms, as shown in Figure 6-7. During these experiments, the rewetting of the superheated surface of the microdevice behaved as a fast-quenching event that caused the sharp and sudden temperature drop. The length of this event decreased as the surface temperature became more superheated. At the end of the quenching event, the surface temperature started to increase, which indicated the end of the rewetting process and the onset of the bubble nucleation. The subsequent gradual increase in surface temperature indicated the advancing movement of the MCL on the sensing region due to the growing bubble. The increasing trend in surface temperature continued the rest of the bubble ebullition cycle until the nucleated bubble departed at the end of the cycle. After the growing bubble reached its maximum diameter at the onset of the departure, the MCL started to recede. The receding MCL rewetted the dried-out areas and led toward the next bubbling cycle with its sudden and sharp decrease in surface temperature.

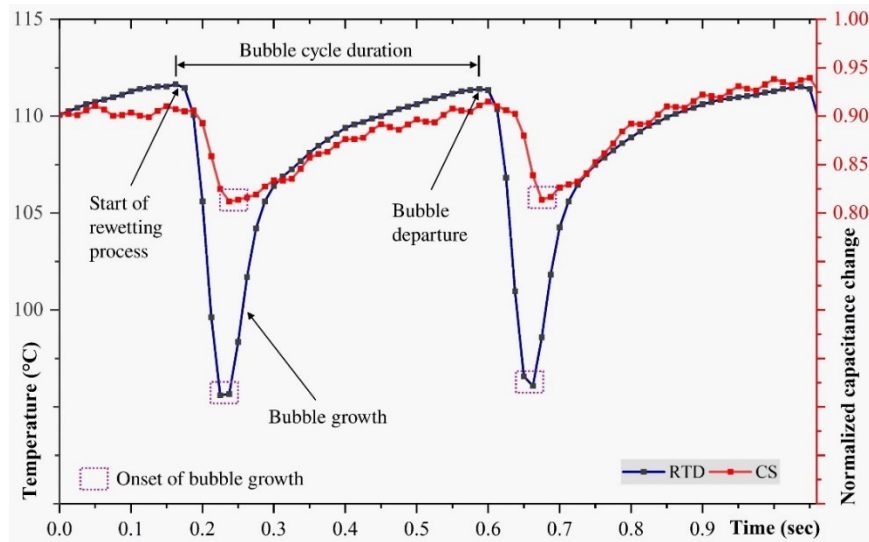


Figure 6-6: A detailed view of the MCL passage and surface temperature variation of two consecutive bubbling events for an experiment conducted at a surface temperature of 111.5 °C.

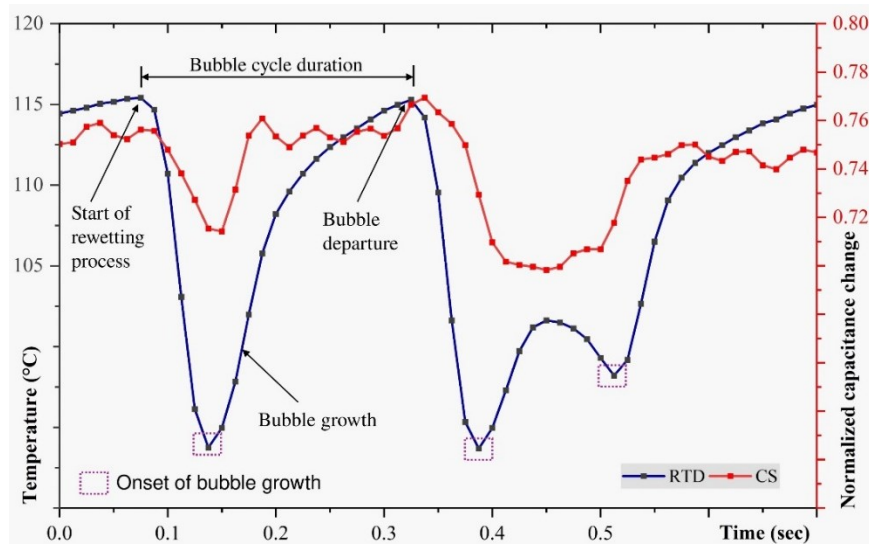


Figure 6-7: A detailed view of the MCL passage and surface temperature variation of two consecutive bubbling events for an experiment conducted at a surface temperature of 115.4 °C.

As shown in Figures 6-6 and 6-7, rewetting, bubble growth, and departure are all coordinated with the movement of MCL tracked by the capacitance sensor. With the

receding movement of the MCL due to the rewetting process, the capacitance sensor exhibited a sharp decrease in the capacitance signal. At the onset of the bubble growth, the capacitance sensor also showed a gradual increase in the signal, indicating the advancing movement of MCL due to bubble growth. Following the rise in surface temperature, the capacitance signal continued to increase until the growing bubble diameter reached its maximum, and the MCL started to recede. The capacitance signal change also agrees with the receding MCL movement due to the following rewetting process and marked the beginning of the next bubbling cycle. The capability of correlating the independence of MCL movement and corresponding temperature variation due to the bubble ebullition cycle facilitated a significant utility of the sensing scheme employed in this work. This capacitance sensor precisely tracked the advancing and receding movement of the MCL instead of inferring or relying on external equipment, which added a significant advantage over other microscale sensing approaches reported in the literature [114], [118], [125], [126].

Various heater power was applied to the device's heater while keeping the pool temperature at 98 °C to investigate the influence of surface temperature on the bubbling event. Figure 6-6 shows the surface temperature variation and the MCL passage of two consecutive bubbling events for an experiment conducted at a surface temperature of 111.5 °C. A higher heater power of 3551.1 mW facilitated a surface temperature of 115.4 °C. This increased heater power nucleated bubbles faster than the previous experiment shown in Figure 6-6. Figure 6-7 demonstrates the variation in surface temperature & capacitance change associated with this experiment. Table 6-1 summarizes the comparison between these experiments. According to this Table, the total duration of the bubble ebullition cycle

was reduced by 43.2% when the device heater power increased from 2659.3 to 3551.1 mW. The time period between nucleating two consecutive bubbles also reduced as the heater power increased. The maximum temperature drop for the experiment with higher heater power was 21.7 °C, 34.8% higher than for the experiment with lower heater power. Also, higher heater power nucleated bubbles at a faster rate and occasionally led to bubble streams instead of single bubbles, as shown in Figures 6-7.

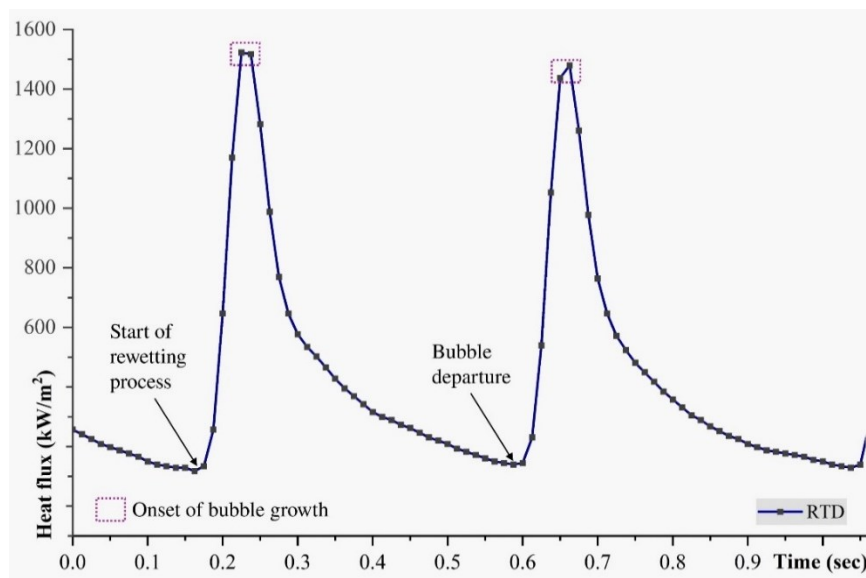


Figure 6-8: Vertical heat fluxes corresponding to the surface temperature variation of three consecutive bubbling events for an experiment conducted at a surface temperature of 113.2 °C.

Table 6-1: Summary of the effect of surface temperature on the bubbling event.

Surface temperature	Duration of bubble cycle	Maximum temperature change	Time period between two consecutive bubble cycles
111.5 °C	0.44 s	16.1 °C	0.43 s
115.4 °C	0.25 s	21.7 °C	0.25 s

The local heat flux values were evaluated by employing the RTD-measured variation in surface temperature during the bubbling events and calculated as in the

previous evaporation experiments. Figures 6-8 and 6-9 depict the variation in vertical heat fluxes corresponding to the surface temperature variation of two consecutive bubbling events for the experiment shown in Figures 6-5 and 6-6, respectively. According to these figures, the maximum heat flux occurred during the receding movement of the MCL, where the fast-quenching event due to rewetting of the superheated surface caused the maximum temperature difference in the sensing region.

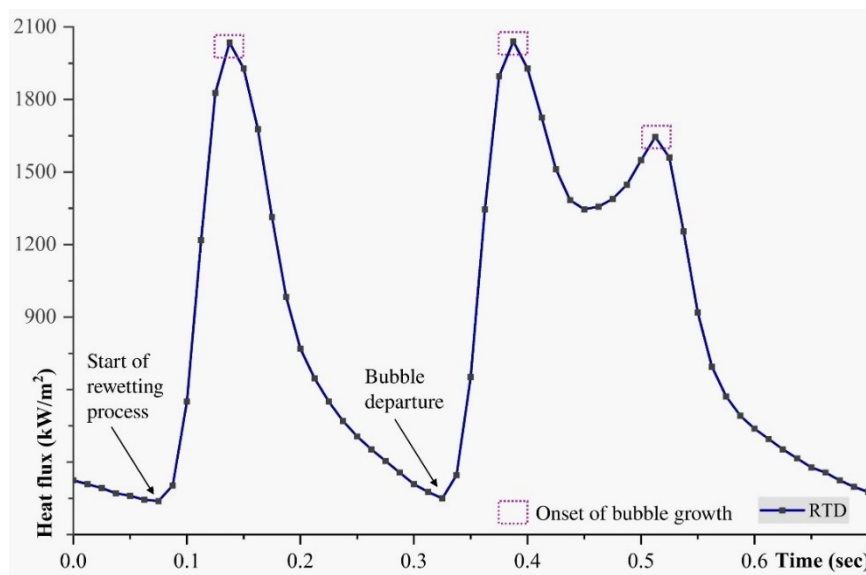


Figure 6-9: Vertical heat fluxes corresponding to the surface temperature variation of three consecutive bubbling events for an experiment conducted at a surface temperature of 113.2 °C.

At the end of the rewetting event, starting from the onset of bubble nucleation, the surface temperature increased, demonstrating a gradual decrease in vertical heat flux until the bubble departed from the sensing region. Right after the bubble departure, the rewetting process began, leading toward the next bubbling cycle, and these figures likewise demonstrated a similar sharp rise in heat flux values. Please refer to Chapter 4 for more details on the vertical heat flux calculations and measurement uncertainty.

6.4 Summary of Findings

This work employed a custom-made MEMS device to simultaneously measure surface temperature variation and track the movement of the MCL for isolated bubbling events during nucleate boiling of water. The experimental results exhibited the heat transfer phenomena and interfacial movement during rewetting, bubble growth, and departure events that usually occur throughout the bubble ebullition cycle. The local temperature measurement and tracking of the movement of the MCL throughout these events validated the dual functionality of this MEMS device and demonstrated the following findings.

- The rewetting process of the superheated sensing region acted as a fast-quenching event that caused a sharp and sudden temperature drop, and the duration of this event shortened with increasing surface temperature.
- The bubble nucleation followed the rewetting process and caused a gradual increase in surface temperature as the bubble started to grow with the advancing movement of the MCL.
- When the growing bubble diameter reached its maximum, the MCL started to recede, indicating the beginning of the rewetting process, which led to the next bubbling cycle.
- Surface superheat played a significant role; the maximum temperature drop for the experiment with a higher surface temperature was 21.7 °C, 34.8% higher than for the experiment with a lower surface temperature.

CHAPTER 7

CONCLUSIONS AND FUTURE WORKS

7.1 Conclusions

This dissertation presented several custom-made MEMS devices and their applications in investigating technologically important phase-change cooling processes. Phase-change cooling has been one of the major emphases in recent years because of its superior performance and efficiency in modern thermal management systems, specifically in microelectronic industries, which are currently dealing with large power densities associated with the downscaling of integrated circuits. Investigating the underlying physics behind these phase-change cooling processes is essential for refining heat transfer models, optimizing surface engineering, and enhancing overall effectiveness. Most importantly, these processes involve various complex physical phenomena and thus require a multifaceted sensing scheme to correlate both the heat transfer mechanism and the phase interface behavior.

In its earlier part, this dissertation presented a MEMS device based on capacitance microsensors capable of tracking the MCL movement during dosing and retraction of unconstrained water droplets. Using a semiconductor base caused signal inversion and coupling effects for multiple sensors in adjacent proximity, which was resolved when a dielectric base was adopted. Moreover, incorporating a thin-film resistance heater with this

capacitance-sensing microdevice made it applicable for elevated temperature applications and dynamic phase change cooling processes such as droplet evaporation.

This efficient technique of tracking MCL was then combined with temperature-sensing RTDs to fabricate a composite MEMS device to investigate phase-change cooling processes. This MEMS device also included a thin film resistance heater, making it an independent experimental setup. It was employed first to explore the heat transfer phenomena and MCL behavior during droplet evaporation of small-scale water droplets from the heated polyimide top surface of the device. This composite sensing scheme presented a few important findings specifically correlating the MCL movement and its influence on surface temperature variation throughout the process. Based on this investigation, MCL precedes the actual change in local surface temperature, contributing more than 70% of the overall temperature change during evaporation. Also, the advancing MCL of an evaporating droplet due to dosing exhibited a more significant temperature change than that associated with a receding MCL due to evaporation. Furthermore, the maximum local heat flux values occurred at this region due to the significant differences in wall temperature underneath the liquid bulk and MCL regions.

After successfully investigating droplet evaporation, this dissertation presented another study investigating a more transient heat transfer process due to droplet impingement on a heated surface. The composite MEMS device used in the previous study underwent a few modifications to make it responsive to fast temperature changes. Then, it was employed to investigate droplet impingement heat transfer on the heated top surface at varying impact velocities across various surface temperatures. Both these studies precisely evaluated that MCL is the region with the highest heat transfer characteristics

rather than inferring or relying on external equipment as the previous works in the literature did. This study revealed the heat transfer modes, their transition, and their contribution to the overall heat transfer during droplet impingement and subsequent sessile droplet evaporation. Based on the experimental results, when a droplet impacts a heated surface and evaporates, the process can be divided into two segments based on the effective heat transfer rate: an initial conduction-dominated segment followed by another segment dominated by surface evaporation. Moreover, convection within evaporating droplets contributes negligibly to overall heat transfer, which is dominated by heat conduction into the droplet and surface evaporation.

Finally, this dissertation presented another study investigating isolated nucleated water bubbles in a pool boiling environment. The composite MEMS device underwent further modification, including an artificial nucleation cavity at the center of the sensing zone to facilitate bubble nucleation. This study presented results on interfacial behavior and corresponding surface temperature variation during isolated bubble nucleation at different surface temperatures. Based on the experiments conducted, the rewetting process of the superheated sensing region acted as a fast-quenching event that caused a sharp and sudden temperature drop and contained the highest local heat flux value. From the onset of bubble formation till the departure, the surface temperature gradually decreases because of the dried-out areas underneath the growing bubble. Once the bubble departed, the MCL started to recede and cover the dried-out region, leading to rewetting for the next bubbling cycle. Results also showed that the surface superheat played a significant role; the maximum temperature drop for the experiment with a higher surface temperature was 21.7 °C, 34.8% higher than for the experiment with a lower surface temperature.

To summarize, this dissertation primarily aimed to develop functional composite MEMS devices and implement them to investigate the underlying physics behind various technologically important phase-change cooling processes, thereby collectively contributing to enhancements in thermal management solutions. Chapters 2 to 4 demonstrated the device design, fabrication, and optimization, which facilitated a capacitance sensing scheme for real-time tracking of the MCL and microscale temperature sensors for measuring temperature variations during phase-change cooling processes. The subsequent chapters demonstrated the implementation of these optimized composite MEMS devices to investigate the heat transfer mechanisms and phase-interface behavior in real-life phase-change cooling processes, such as droplet evaporation and impingement on a heated surface and nucleate boiling. The experimental results of this dissertation from studying these phase-change cooling processes provided essential insights into underlying physics to improve heat transfer models, optimize surface engineering, and enhance overall effectiveness. Moreover, real-time, minimally invasive temperature measurements and simultaneous tracking of MCL at the microscale by the composite MEMS devices utilized in these studies can aid in thermal management and process control across various industries.

7.2 Future Works

While the functional MEMS devices and their implementation in exploring phase-change cooling processes presented in this dissertation have provided valuable insights, there is still room for improvement in the existing device designs. Additionally, further investigations can be conducted across different working conditions and surface conditions to enhance these devices' functionality and explore new insights. These devices and the

experimental techniques utilized in these studies can pave the way for future research opportunities described below.

- The future improvement of the capacitance-sensing MEMS device should primarily focus on further reducing the proximity effect by enhanced filtering and minimizing parasitic capacitance in leads, traces, interconnects, and other system elements.
- The future direction of this capacitance sensing research should emphasize analyzing how the capacitance signal and electric fields vary when dealing with different surface/droplet interactions, such as more hydrophilic and hydrophobic droplets.
- Future research should also investigate how the capacitance signals behave when dealing with the partial wetting or de-wetting of the interdigitated electrodes of the capacitance sensors to find out how the measured signals differ from conventional experiments involving complete wetting of the sensing region. Additionally, if the IDEs of the capacitance sensor can be effectively scaled down, this sensing scheme could provide efficient detection of microscale droplets and potentially achieve detection capabilities smaller than conventional cameras.
- An emphasis on improving the composite MEMS device should focus on increasing the spatial resolution via a more compact geometry for the IDEs and the RTDs. Another emphasis should be on improving the temporal resolution of these sensors, especially in the case of combined data acquisition employing both IDEs and RTDs.
- Many industrial applications, especially spray cooling, involve very complex drop-on-drop interactions, so future work should focus on the investigation of heat transfer for subcooled and superheated drop-on-drop interactions on heated surfaces with the composite MEMS device.

- The composite MEMS device presented in this dissertation can be further modified to investigate phase change heat transfer associated with nanofluid droplets on surfaces with different thermal conductivities or wettability to achieve enhanced heat dissipation capability.
- Future research should also focus on improving the MEMS device employed for investigating pool boiling by incorporating a more efficient nucleation cavity that promotes more controlled bubble nucleation. Further research should also focus on improving this device's temporal and spatial resolution for more efficient investigation of nucleate boiling processes with different technologically important working fluids.

REFERENCES

- [1] M. M. Nahar *et al.*, “Review article: Microscale evaporative cooling technologies for high heat flux microelectronics devices: Background and recent advances,” *Appl. Therm. Eng.*, vol. 194, no. May, 2021.
- [2] P. K. Tyagi, R. Kumar, and P. K. Mondal, “A review of the state-of-the-art nanofluid spray and jet impingement cooling,” *Phys. Fluids*, vol. 32, no. 12, 2020.
- [3] J. L. Plawsky *et al.*, “Nano-and microstructures for thin-film evaporation-A review,” *Nanoscale Microscale Thermophys. Eng.*, vol. 18, no. 3, pp. 251–269, 2014.
- [4] G. Liang and I. Mudawar, “Review of drop impact on heated walls,” *Int. J. Heat Mass Transf.*, vol. 106, pp. 103–126, 2017.
- [5] J. D. Benthier, J. D. Pelaez-Restrepo, C. Stanley, and G. Rosengarten, “Heat transfer during multiple droplet impingement and spray cooling: Review and prospects for enhanced surfaces,” *Int. J. Heat Mass Transf.*, vol. 178, p. 121587, 2021.
- [6] R. K. Mandel, D. G. Bae, and M. M. Ohadi, “Embedded Two-Phase Cooling of High Flux Electronics Via Press-Fit and Bonded FEEDS Coolers,” *J. Electron. Packag.*, vol. 140, no. 3, 2018.
- [7] M. Buchholz, H. Auracher, T. Lüttich, and W. Marquardt, “A study of local heat transfer mechanisms along the entire boiling curve by means of microsensors,” *Int. J. Therm. Sci.*, vol. 45, no. 3, pp. 269–283, 2006.
- [8] R. Raj, J. Kim, and J. McQuillen, “On the scaling of pool boiling heat flux with gravity and heater size,” *J. Heat Transfer*, vol. 134, no. 1, pp. 1–13, 2012.
- [9] G. Guggilla, R. Narayanaswamy, and A. Pattamatta, “An experimental investigation into the spread and heat transfer dynamics of a train of two concentric impinging droplets over a heated surface,” *Exp. Therm. Fluid Sci.*, vol. 110, no. September 2019, p. 109916, 2020.
- [10] O. E. Ruiz and W. Z. Black, “Evaporation of water droplets placed on a heated horizontal surface,” *J. Heat Transfer*, vol. 124, no. 5, pp. 854–863, 2002.
- [11] M. J. Gibbons, P. Di Marco, and A. J. Robinson, “Local heat transfer to an evaporating superhydrophobic droplet,” *Int. J. Heat Mass Transf.*, vol. 121, pp. 641–652, 2018.

- [12] J. Eggers and H. A. Stone, "Characteristic lengths at moving contact lines for a perfectly wetting fluid: The influence of speed on the dynamic contact angle," *J. Fluid Mech.*, vol. 505, no. 505, pp. 309–321, 2004.
- [13] E. F. Crafton and W. Z. Black, "Heat transfer and evaporation rates of small liquid droplets on heated horizontal surfaces," *Int. J. Heat Mass Transf.*, vol. 47, no. 6–7, pp. 1187–1200, 2004.
- [14] C. P. Migliaccio, H. K. Dhavaleswarapu, and S. V. Garimella, "Temperature measurements near the contact line of an evaporating meniscus V-groove," *Int. J. Heat Mass Transf.*, vol. 54, no. 7–8, pp. 1520–1526, 2011.
- [15] H. K. Dhavaleswarapu, S. V. Garimella, and J. Y. Murthy, "Microscale temperature measurements near the triple line of an evaporating thin liquid film," *J. Heat Transfer*, vol. 131, no. 6, pp. 1–7, 2009.
- [16] C. Elbuken, T. Glawdel, D. Chan, and C. L. Ren, "Detection of microdroplet size and speed using capacitive sensors," *Sensors Actuators, A Phys.*, vol. 171, no. 2, pp. 55–62, 2011.
- [17] J. Z. Chen, A. A. Darhuber, S. M. Troian, and S. Wagner, "Capacitive sensing of droplets for microfluidic devices based on thermocapillary actuation," *Lab Chip*, vol. 4, no. 5, pp. 473–480, 2004.
- [18] M. T. H. Mondal, T. Desai, R.-E.-N. Hossain, and A. L. Moore, "Microscale tracking of unconstrained moving multiphase contact lines via a capacitance sensor array," *Sensors Actuators A Phys.*, vol. 331, p. 113046, 2021.
- [19] P. Kubra Isgor, M. Marcali, M. Keser, and C. Elbuken, "Microfluidic droplet content detection using integrated capacitive sensors," *Sensors Actuators, B Chem.*, vol. 210, pp. 669–675, 2015.
- [20] Y. D. Shikhmurzaev, "The moving contact line on a smooth solid surface," *Int. J. Multiph. Flow*, vol. 19, no. 4, pp. 589–610, 1993.
- [21] Y. Zhao, "Moving contact line problem: Advances and perspectives," *Theor. Appl. Mech. Lett.*, vol. 4, no. 3, p. 34002, 2014.
- [22] N. Srivastava and M. A. Burns, "Electronic drop sensing in microfluidic devices: Automated operation of a nanoliter viscometer," *Lab Chip*, vol. 6, no. 6, pp. 744–751, 2006.
- [23] M. C. Cole and P. J. A. Kenis, "Multiplexed electrical sensor arrays in microfluidic networks," *Sensors Actuators, B Chem.*, vol. 136, no. 2, pp. 350–358, 2009.
- [24] T. Vu Quoc, T. Pham Quoc, T. Chu Duc, T. T. Bui, K. Kikuchi, and M. Aoyagi, "Capacitive sensor based on PCB technology for air bubble inside fluidic flow detection," *Proc. IEEE Sensors*, vol. 2014-Decem, no. December, pp. 237–240,

2014.

- [25] G. Maier, “Low dielectric constant polymers for microelectronics,” *Prog. Polym. Sci.*, vol. 26, no. 1, pp. 3–65, 2001.
- [26] X. Zhao and H. Liu, “Review of polymer materials with low dielectric constant,” no. October 2009, pp. 597–606, 2010.
- [27] C. Barbosa, C. A. Silva, and T. Dong, “Integratable capacitive bubble counter for lab-on-chip devices,” in *2014 IEEE International Symposium on Medical Measurements and Applications (MeMeA)*, 2014, pp. 1–5.
- [28] N. Yazdi, H. Kulah, and K. Najafi, “Precision readout circuits for capacitive microaccelerometers,” *Proc. IEEE Sensors*, vol. 1, no. 2, pp. 28–31, 2004.
- [29] J. Wei, C. Yue, Z. L. Chen, Z. W. Liu, and P. M. Sarro, “A silicon MEMS structure for characterization of femto-farad-level capacitive sensors with lock-in architecture,” *J. Micromechanics Microengineering*, vol. 20, no. 6, 2010.
- [30] J. EGGERS and H. A. STONE, “Characteristic lengths at moving contact lines for a perfectly wetting fluid: the influence of speed on the dynamic contact angle,” *J. Fluid Mech.*, vol. 505, pp. 309–321, 2004.
- [31] A. Mohammad Karim, “A review of physics of moving contact line dynamics models and its applications in interfacial science,” *J. Appl. Phys.*, vol. 132, no. 8, p. 080701, 2022.
- [32] Y. Sui, H. Ding, and P. D. M. Spelt, “Numerical simulations of flows with moving contact lines,” *Annu. Rev. Fluid Mech.*, vol. 46, pp. 97–119, 2014.
- [33] J. H. Snoeijer and B. Andreotti, “Moving contact lines: Scales, regimes, and dynamical transitions,” *Annu. Rev. Fluid Mech.*, vol. 45, pp. 269–292, 2013.
- [34] S. Semenov, V. M. Starov, M. G. Velarde, and R. G. Rubio, “Droplets evaporation: Problems and solutions,” *Eur. Phys. J. Spec. Top.*, vol. 197, no. 1, pp. 265–278, 2011.
- [35] R. Raj, C. Kunkelmann, P. Stephan, J. Plawsky, and J. Kim, “Contact line behavior for a highly wetting fluid under superheated conditions,” *Int. J. Heat Mass Transf.*, vol. 55, no. 9–10, pp. 2664–2675, 2012.
- [36] K. Ibrahim, M. F. Abd Rabbo, T. Gambaryan-Roisman, and P. Stephan, “Experimental investigation of evaporative heat transfer characteristics at the 3-phase contact line,” *Exp. Therm. Fluid Sci.*, vol. 34, no. 8, pp. 1036–1041, 2010.
- [37] C. Kunkelmann, K. Ibrahim, N. Schweizer, S. Herbert, P. Stephan, and T. Gambaryan-Roisman, “The effect of three-phase contact line speed on local evaporative heat transfer: Experimental and numerical investigations,” *Int. J. Heat*

Mass Transf., vol. 55, no. 7–8, pp. 1896–1904, 2012.

- [38] E. V. Moiseeva, A. A. Fletcher, and C. K. Harnett, “Thin-film electrode based droplet detection for microfluidic systems,” *Sensors Actuators, B Chem.*, vol. 155, no. 1, pp. 408–414, 2011.
- [39] W. wen Liu and Y. Zhu, “Development and application of analytical detection techniques for droplet-based microfluidics’-A review,” *Anal. Chim. Acta*, vol. 1113, pp. 66–84, 2020.
- [40] A. Ernst, W. Streule, N. Schmitt, R. Zengerle, and P. Koltay, “A capacitive sensor for non-contact nanoliter droplet detection,” *Sensors Actuators, A Phys.*, vol. 153, no. 1, pp. 57–63, 2009.
- [41] S. A. Putnam *et al.*, “Microdroplet evaporation on superheated surfaces,” *Int. J. Heat Mass Transf.*, vol. 55, no. 21–22, pp. 5793–5807, 2012.
- [42] D. Nieto, T. Delgado, and M. T. Flores-Arias, “Fabrication of microchannels on soda-lime glass substrates with a Nd:YVO4 laser,” *Opt. Lasers Eng.*, vol. 63, pp. 11–18, 2014.
- [43] H. Ci *et al.*, “6-Inch Uniform Vertically-Oriented Graphene on Soda-Lime Glass for Photothermal Applications,” *Nano Res.*, vol. 11, no. 6, pp. 3106–3115, 2018.
- [44] C. H. Lin, G. Bin Lee, Y. H. Lin, and G. L. Chang, “A fast prototyping process for fabrication of microfluidic systems on soda-lime glass,” *J. Micromechanics Microengineering*, vol. 11, no. 6, pp. 726–732, 2001.
- [45] M. J. Gibbons, A. I. Garivalis, S. O’Shaughnessy, P. Di Marco, and A. J. Robinson, “Evaporating hydrophilic and superhydrophobic droplets in electric fields,” *International Journal of Heat and Mass Transfer*, vol. 164. 2021.
- [46] P. Di Marco, R. Kurimoto, G. Saccone, K. Hayashi, and A. Tomiyama, “Bubble shape under the action of electric forces,” *Exp. Therm. Fluid Sci.*, vol. 49, pp. 160–168, 2013.
- [47] H. Almohammadi and A. Amirfazli, “Sessile drop evaporation under an electric field,” *Colloids Surfaces A Physicochem. Eng. Asp.*, vol. 555, pp. 580–585, 2018.
- [48] D. Zang, S. Tarafdar, Y. Y. Tarasevich, M. Dutta Choudhury, and T. Dutta, “Evaporation of a Droplet: From physics to applications,” *Phys. Rep.*, vol. 804, pp. 1–56, 2019.
- [49] S. Y. Misyura, “Evaporation of a sessile water drop and a drop of aqueous salt solution,” *Sci. Rep.*, vol. 7, no. 1, pp. 1–11, 2017.
- [50] S. K. Wilson and H. M. D’Ambrosio, “Evaporation of Sessile Droplets,” *Annu. Rev. Fluid Mech.*, vol. 55, pp. 481–509, 2023.

- [51] Z. Zheng, L. Zhou, X. Du, and Y. Yang, “Numerical investigation on conjugate heat transfer of evaporating thin film in a sessile droplet,” *Int. J. Heat Mass Transf.*, vol. 101, pp. 10–19, 2016.
- [52] E. Lakew, A. Sarchami, G. Giustini, H. Kim, and K. Bellur, “Thin Film Evaporation Modeling of the Liquid Microlayer Region in a Dewetting Water Bubble,” *Fluids*, vol. 8, no. 4, 2023.
- [53] K. Chen, R. N. Xu, and P. X. Jiang, “Evaporation Enhancement of Microscale Droplet Impact on Micro/Nanostructured Surfaces,” *Langmuir*, vol. 36, no. 41, pp. 12230–12236, 2020.
- [54] M. J. Gibbons, P. Di Marco, and A. J. Robinson, “Local heat transfer to an evaporating superhydrophobic droplet,” *Int. J. Heat Mass Transf.*, vol. 121, pp. 641–652, 2018.
- [55] A.-M. Cazabat and G. Guéna, “Evaporation of macroscopic sessile droplets,” *Soft Matter*, vol. 6, no. 12, pp. 2591–2612, 2010.
- [56] A. L. Karchevsky, I. V Marchuk, and O. A. Kabov, “Calculation of the heat flux near the liquid–gas–solid contact line,” *Appl. Math. Model.*, vol. 40, no. 2, pp. 1029–1037, 2016.
- [57] P. A. Raghupathi and S. G. Kandlikar, “Contact line region heat transfer mechanisms for an evaporating interface,” *Int. J. Heat Mass Transf.*, vol. 95, pp. 296–306, 2016.
- [58] S. S. Panchamgam, A. Chatterjee, J. L. Plawsky, and P. C. Wayner, “Comprehensive experimental and theoretical study of fluid flow and heat transfer in a microscopic evaporating meniscus in a miniature heat exchanger,” *Int. J. Heat Mass Transf.*, vol. 51, no. 21–22, pp. 5368–5379, 2008.
- [59] P. Stephan and C. A. Busse, “Analysis of the heat transfer coefficient of grooved heat pipe evaporator walls,” *Int. J. Heat Mass Transf.*, vol. 35, pp. 383–391, 1992.
- [60] X. Xu and V. P. Carey, “Film evaporation from a micro-grooved surface—an approximate heat transfer model and its comparison with experimental data,” *J. Thermophys. Heat Transf.*, vol. 4, no. 4, pp. 512–520, 1990.
- [61] B. Sobac and D. Brutin, “Triple-line behavior and wettability controlled by nanocoated substrates: Influence on sessile drop evaporation,” *Langmuir*, vol. 27, no. 24, pp. 14999–15007, 2011.
- [62] J. G. Myers, V. K. Yerramilli, S. W. Hussey, G. F. Yee, and J. Kim, “Time and space resolved wall temperature and heat flux measurements during nucleate boiling with constant heat flux boundary conditions,” *Int. J. Heat Mass Transf.*, vol. 48, no. 12, pp. 2429–2442, 2005.

- [63] C. Sodtke, V. S. Ajaev, and P. Stephan, "Dynamics of volatile liquid droplets on heated surfaces: Theory versus experiment," *J. Fluid Mech.*, vol. 610, pp. 343–362, 2008.
- [64] T. H. Kim, E. Kommer, S. Dessiatoun, and J. Kim, "Measurement of two-phase flow and heat transfer parameters using infrared thermometry," *Int. J. Multiph. Flow*, vol. 40, pp. 56–67, 2012.
- [65] S. W. Paik, K. D. Kihm, S. P. Lee, and D. M. Pratt, "Spatially and temporally resolved temperature measurements for slow evaporating sessile drops heated by a microfabricated heater array," *J. Heat Transfer*, vol. 129, no. 8, pp. 966–976, 2007.
- [66] M. Buchholz, T. Lüttich, H. Auracher, and W. Marquardt, "Experimental investigation of local processes in pool boiling along the entire boiling curve," *Int. J. Heat Fluid Flow*, vol. 25, no. 2, pp. 243–261, 2004.
- [67] H. Auracher and W. Marquardt, "Heat transfer characteristics and mechanisms along entire boiling curves under steady-state and transient conditions," *Int. J. Heat Fluid Flow*, vol. 25, no. 2, pp. 223–242, 2004.
- [68] R. Raj, J. Kim, and J. McQuillen, "Pool boiling heat transfer on the international space station: Experimental results and model verification," *J. Heat Transfer*, vol. 134, no. 10, pp. 1–14, 2012.
- [69] J. Jung, S. J. Kim, and J. Kim, "Observations of the critical heat flux process during pool boiling of FC-72," *J. Heat Transfer*, vol. 136, no. 4, 2014.
- [70] S. Bae, M. Kim, and J. Kim, "Improved technique to measure time and space-resolved heat transfer under single bubbles during saturated pool boiling of fc-72," *Exp. Heat Transf.*, vol. 12, no. 3, pp. 265–278, 1999.
- [71] Y. Fukatani, D. Orejon, Y. Kita, Y. Takata, J. Kim, and K. Sefiane, "Effect of ambient temperature and relative humidity on interfacial temperature during early stages of drop evaporation," *Phys. Rev. E*, vol. 93, no. 4, pp. 1–16, 2016.
- [72] L. Bogdanic, H. Auracher, and F. Ziegler, "Two-phase structure above hot surfaces in jet impingement boiling," *Heat Mass Transf. und Stoffuebertragung*, vol. 45, no. 7, pp. 1019–1028, 2009.
- [73] H. Robidou, H. Auracher, P. Gardin, and M. Lebouché, "Controlled cooling of a hot plate with a water jet," *Exp. Therm. Fluid Sci.*, vol. 26, no. 2–4, pp. 123–129, 2002.
- [74] H. Auracher and W. Marquardt, "Experimental studies of boiling mechanisms in all boiling regimes under steady-state and transient conditions," *Int. J. Therm. Sci.*, vol. 41, no. 7, pp. 586–598, 2002.
- [75] Y. M. Qiao and S. Chandra, "Experiments on adding a surfactant to water drops boiling on a hot surface," *Proc. R. Soc. A Math. Phys. Eng. Sci.*, vol. 453, no. 1959,

pp. 673–689, 1997.

- [76] S. Chandra and C. T. Avedisian, “Evaporation and Combustion of Levitated Arrays of Two, Three and Five Droplets At a Hot Surface.,” *Proc. R. Soc. London, Ser. A Math. Phys. Sci.*, vol. 418, no. 1855, pp. 365–382, 1988.
- [77] S. Chandra and C. T. Avedisian, “On the collision of a droplet with a solid surface,” *Proc. R. Soc. A Math. Phys. Eng. Sci.*, vol. 432, no. 1884, pp. 13–41, 1991.
- [78] J. D. Bernardin, I. Mudawar, C. B. Walsh, and E. I. Franses, “Contact angle temperature dependence for water droplets on practical aluminum surfaces,” *Int. J. Heat Mass Transf.*, vol. 40, no. 5, pp. 1017–1033, 1997.
- [79] J. D. Bernardin, C. J. Stebbins, and I. Mudawar, “Effects of surface roughness on water droplet impact history and heat transfer regimes,” *International Journal of Heat and Mass Transfer*, vol. 40, no. 1, pp. 73–88, 1996.
- [80] J. Kim, J. Kim, Y. Shin, and Y. Yoon, “A Study on the Fabrication of an RTD (Resistance Temperature Detector) by Using Pt Thin Film,” *Korean J. Chem. Eng.*, vol. 18, no. 1, pp. 61–66, 2001.
- [81] Y. Wang, C. Zhang, J. Li, G. Ding, and L. Duan, “Fabrication and characterization of ITO thin film resistance temperature detector,” *Vacuum*, vol. 140, pp. 121–125, 2017.
- [82] M. T. H. Mondal, R.-E.-N. Hossain, R. Martin, and A. L. Moore, “Speed and location tracking of moving multiphase interfaces via a capacitance microsensor array during droplet evaporation,” *Micro Nano Eng.*, vol. 17, no. September, p. 100168, 2022.
- [83] X. Y. Zhao and H. J. Liu, “Review of polymer materials with low dielectric constant,” *Polym. Int.*, vol. 59, no. 5, pp. 597–606, 2010.
- [84] X. Wang, S. A. Ghaffarizadeh, X. He, A. J. H. McGaughey, and J. A. Malen, “Ultrahigh evaporative heat transfer measured locally in submicron water films,” *Sci. Rep.*, vol. 12, no. 1, p. 22353, 2022.
- [85] T. Chen, “Heat transfer to wetting and non-wetting liquid droplets deposited onto a heated microgroove surface,” *Proc. 15th Intersoc. Conf. Therm. Thermomechanical Phenom. Electron. Syst. ITherm 2016*, pp. 987–993, 2016.
- [86] S. David, K. Sefiane, and L. Tadrist, “Experimental investigation of the effect of thermal properties of the substrate in the wetting and evaporation of sessile drops,” *Colloids Surfaces A Physicochem. Eng. Asp.*, vol. 298, no. 1–2, pp. 108–114, 2007.
- [87] S. L. Manzello and J. C. Yang, “An experimental investigation of water droplet impingement on a heated wax surface,” *Int. J. Heat Mass Transf.*, vol. 47, no. 8–9, pp. 1701–1709, 2004.

- [88] S. L. Manzello and J. C. Yang, "An experimental study of a water droplet impinging on a liquid surface," *Exp. Fluids*, vol. 32, no. 5, pp. 580–589, 2002.
- [89] A. Gholijani, C. Schlawitschek, T. Gambaryan-Roisman, and P. Stephan, "Heat transfer during drop impingement onto a hot wall: The influence of wall superheat, impact velocity, and drop diameter," *Int. J. Heat Mass Transf.*, vol. 153, p. 119661, 2020.
- [90] M. Pasandideh-Fard, S. D. Aziz, S. Chandra, and J. Mostaghimi, "Cooling effectiveness of a water drop impinging on a hot surface," *Int. J. Heat Fluid Flow*, vol. 22, no. 2, pp. 201–210, 2001.
- [91] S. Herbert, S. Fischer, T. Gambaryan-Roisman, and P. Stephan, "Local heat transfer and phase change phenomena during single drop impingement on a hot surface," *Int. J. Heat Mass Transf.*, vol. 61, pp. 605–614, 2013.
- [92] A. Gholijani, T. Gambaryan-Roisman, and P. Stephan, "Experimental investigation of hydrodynamics and heat transport during vertical coalescence of multiple successive drops impacting a hot wall under saturated vapor atmosphere," *Exp. Therm. Fluid Sci.*, vol. 118, p. 110145, 2020.
- [93] S. Herbert, S. Fischer, T. Gambaryan-Roisman, and P. Stephan, "Local heat transfer and phase change phenomena during single drop impingement on a hot surface," *Int. J. Heat Mass Transf.*, vol. 61, no. 1, pp. 605–614, 2013.
- [94] A. B. Wang, C. H. Lin, and C. C. Cheng, "Pattern analysis of a single droplet impinging onto a heated plate," *Heat Transf. - Asian Res.*, vol. 34, no. 8, pp. 579–594, 2005.
- [95] H. Jones, M. H. Burden, G. Thursfield, H. Liu, E. J. Lavernia, and R. H. Rangel, "A rotary atomization technique for bulk splat cooling Splat cooling and metastable phases H Jones A gas atomization spray quenching technique for bulk splat cooling Numerical simulation of substrate impact and freezing of droplets in plasma spray processe," *J. Phys. D Appl. Phys.*, vol. 4, p. 1657, 1971.
- [96] S. Moghtadernejad, C. Lee, and M. Jadidi, "An introduction of droplet impact dynamics to engineering students," *Fluids*, vol. 5, no. 3, pp. 1–18, 2020.
- [97] A. R. Pati, B. Swain, and S. S. Mohapatra, "The Boiling Phenomena and their Proper Identification and Discrimination Methodology," *Sci. Rep.*, vol. 10, no. 1, pp. 1–8, 2020.
- [98] J. D. Bernardin, C. J. Stebbins, and I. Mudawar, "Mapping of impact and heat transfer regimes of water drops impinging on a polished surface," *Int. J. Heat Mass Transf.*, vol. 40, no. 2, pp. 247–267, 1997.
- [99] T. Tran, H. J. J. Staat, A. Prosperetti, C. Sun, and D. Lohse, "Drop impact on superheated surfaces," *Phys. Rev. Lett.*, vol. 108, no. 3, pp. 1–5, 2012.

- [100] A.-B. Wang, C. Lin, and C.-C. Chen, “The critical temperature of dry impact for tiny droplet impinging on a heated surface,” *Phys. Fluids*, vol. 12, pp. 1622–1625, 2000.
- [101] H. J. J. Staat *et al.*, “Phase diagram for droplet impact on superheated surfaces,” *J. Fluid Mech.*, vol. 779, p. R3, 2015.
- [102] S. Herbert, T. Gambaryan-Roisman, and P. Stephan, “Influence of the governing dimensionless parameters on heat transfer during single drop impingement onto a hot wall,” *Colloids Surfaces A Physicochem. Eng. Asp.*, vol. 432, pp. 57–63, 2013.
- [103] V. E. Nakoryakov, S. Y. Misyura, and S. L. Elistratov, “The behavior of water droplets on the heated surface,” *Int. J. Heat Mass Transf.*, vol. 55, no. 23–24, pp. 6609–6617, 2012.
- [104] C. Qiang, S. Chandra, and S. McCahan, “The Effect of Dissolving Gases or Solids in Water Droplets Boiling on a Hot Surface,” *J. Heat Transfer*, vol. 123, no. 4, pp. 719–728, 2001.
- [105] M. T. H. Mondal, R.-E.-N. Hossain, R. Martin, and A. L. Moore, “Independent microscale sensing of phase interface and surface temperature during droplet evaporation,” *Appl. Therm. Eng.*, vol. 236, p. 121477, 2024.
- [106] J. Lee, J. Kim, and K. T. Kiger, “Time- and space-resolved heat transfer characteristics of single droplet cooling using microscale heater arrays,” *Int. J. Heat Fluid Flow*, vol. 22, no. 2, pp. 188–200, 2001.
- [107] M. T. H. Mondal, T. Desai, R.-E.-N. Hossain, and A. L. Moore, “Microscale tracking of unconstrained moving multiphase contact lines via a capacitance sensor array,” *Sensors Actuators A Phys.*, vol. 331, p. 113046, 2021.
- [108] M. T. H. Mondal, R.-E.-N. Hossain, R. Martin, and A. L. Moore, “Speed and location tracking of moving multiphase interfaces via a capacitance microsensor array during droplet evaporation,” *Micro Nano Eng.*, p. 100168, 2022.
- [109] W. Huang *et al.*, “Droplet Evaporation on Hot Micro-Structured Superhydrophobic Surfaces: Analysis of Evaporation from Droplet Cap and Base Surfaces,” *Int. J. Heat Mass Transf.*, vol. 185, 2022.
- [110] R. Hays, D. Maynes, and J. Crockett, “Thermal transport to droplets on heated superhydrophobic substrates,” *Int. J. Heat Mass Transf.*, vol. 98, pp. 70–80, 2016.
- [111] G. Lu, Y. Y. Duan, X. D. Wang, and D. J. Lee, “Internal flow in evaporating droplet on heated solid surface,” *Int. J. Heat Mass Transf.*, vol. 54, no. 19–20, pp. 4437–4447, 2011.
- [112] A. Chandramohan, S. Dash, J. A. Weibel, X. Chen, and S. V. Garimella, “Marangoni Convection in Evaporating Organic Liquid Droplets on a Nonwetting Substrate,”

Langmuir, vol. 32, no. 19, pp. 4729–4735, 2016.

- [113] D. B. R. Kenning, *Liquid—vapor phase-change phenomena*, vol. 48, no. 3. 1993.
- [114] S. Moghaddam, K. T. Kiger, A. Modafe, and R. Ghodssi, “A novel benzocyclobutene-based device for studying the dynamics of heat transfer during the nucleation process,” *J. Microelectromechanical Syst.*, vol. 16, no. 6, pp. 1355–1366, 2007.
- [115] M. G. Cooper and A. J. P. Lloyd, “The microlayer in nucleate pool boiling,” *Int. J. Heat Mass Transf.*, vol. 12, no. 8, pp. 895–913, 1969.
- [116] J. Kim, “Review of nucleate pool boiling bubble heat transfer mechanisms,” *Int. J. Multiph. Flow*, vol. 35, no. 12, pp. 1067–1076, 2009.
- [117] J. N. Chung, T. Chen, and S. C. Maroo, “A review of recent progress on nano/micro scale nucleate boiling fundamentals,” *Front. Heat Mass Transf.*, vol. 2, no. 2, 2011.
- [118] J. Buongiorno, D. G. Cahill, C. H. Hidrovo, S. Moghaddam, A. J. Schmidt, and L. Shi, “Micro-and nanoscale measurement methods for phase change heat transfer on planar and structured surfaces,” *Nanoscale Microscale Thermophys. Eng.*, vol. 18, no. 3, pp. 270–287, 2014.
- [119] Z. Cao *et al.*, “Pool boiling heat transfer of FC-72 on pin-fin silicon surfaces with nanoparticle deposition,” *Int. J. Heat Mass Transf.*, vol. 126, pp. 1019–1033, 2018.
- [120] K. C. Leong, J. Y. Ho, and K. K. Wong, “A critical review of pool and flow boiling heat transfer of dielectric fluids on enhanced surfaces,” *Appl. Therm. Eng.*, vol. 112, pp. 999–1019, 2017.
- [121] S. G. Kandlikar, “A New Perspective on Heat Transfer Mechanisms and Sonic Limit in Pool Boiling,” *J. Heat Transfer*, vol. 141, no. 5, 2019.
- [122] S. H. Kim, G. C. Lee, J. Y. Kang, K. Moriyama, M. H. Kim, and H. S. Park, “Boiling heat transfer and critical heat flux evaluation of the pool boiling on micro structured surface,” *Int. J. Heat Mass Transf.*, vol. 91, pp. 1140–1147, 2015.
- [123] A. Mehdikhani, H. Moghadasi, and H. Saffari, “An experimental investigation of pool boiling augmentation using four-step electrodeposited micro/nanostructured porous surface in distilled water,” *Int. J. Mech. Sci.*, vol. 187, no. C, p. 105924, 2020.
- [124] F. Demiray and J. Kim, “Microscale heat transfer measurements during pool boiling of FC-72: Effect of subcooling,” *Int. J. Heat Mass Transf.*, vol. 47, no. 14–16, pp. 3257–3268, 2004.
- [125] S. Moghaddam and K. Kiger, “Physical mechanisms of heat transfer during single bubble nucleate boiling of FC-72 under saturation conditions-I. Experimental

investigation,” *Int. J. Heat Mass Transf.*, vol. 52, no. 5–6, pp. 1284–1294, 2009.

- [126] T. Yabuki and O. Nakabeppu, “Heat transfer mechanisms in isolated bubble boiling of water observed with MEMS sensor,” *Int. J. Heat Mass Transf.*, vol. 76, pp. 286–297, 2014.